Cold and dense clouds of atoms in a Holographic Atom Trap

by

Raymond T R Newell

A dissertation submitted in partial fulfillment

of the requirements for the degree of

Doctor of Philosophy

(Physics)

at the

UNIVERSITY OF WISCONSIN-MADISON

2003

0.1 Abstract

This dissertation describes the development and characterization of a Holographic Atom Trap. This trap, or HAT, employs a novel configuration of far-off resonant laser beams to create a periodic array of small potential wells. These wells, or microtraps, typically measure $10\mu m \times 10\mu m \times 100\mu m$ in the HAT implementation described here, and confine up to 18,000 atoms each at temperatures near 50 microkelvin. The very high oscillation frequencies within the microtraps ($\overline{\nu}$= 18.4 kHz) lead to high atomic densities ($> 10^{14} cm^{-3}$) and a phase space density greater than 1/260. This periodic array of small, high density samples is attractive for a number of experiments, in particular for studies of ultracold Rydberg atoms.

We also present a new type of imaging system useful for traps such as the HAT, known as Spatial Heterodyne Imaging, which we have developed and characterized. This technique measures the index of refraction of a cloud of atoms over a wide range of spatial sizes and without the need for specially-fabricated optics. Spatial Heterodyne imaging is a non-destructive technique, and we demonstrate images with a signal-to-noise ratio greater than ten made with fewer than 0.0004 photons scattered per atom.

Our studies of laser cooling in the HAT are discussed at length. We show that the 50 μK temperature is determined by free evaporation within the trap, and that laser cooling has little or no effect on the temperature of atoms in our trap. Instead we find that the temperature is determined by the depth of the potential trap. An excited-state mixing process is proposed to explain the inability of laser cooling to break the 50 μK barrier.

We have performed a number of forced evaporation experiments with our HAT. By decreasing the potential trap depth we eject hotter atoms from the trap and effectively cool those that remain. We present data with a variety of shapes for the decreasing

potential ramp, including an optimized ramp which cooled 1,100 atoms to $\simeq$ 100nK which corresponds to a phase space density of $0.91^{+1.1}_{-0.5}$. Finally, we discuss the factors that limit the ultimate phase space density and our efforts to overcome them.

0.2 Acknowledgements

I would like to begin by thanking my advisor Dr. Thad Walker for the encouragement and support he has provided throughout my graduate career. Since my arrival in Madison I have enjoyed a fruitful and rewarding relationship with Thad, and for this I am very grateful.

I am especially grateful for the assistance and friendship of my parter in the laboratory, Jennifer Sebby. It has been a privilege to work with someone so intelligent, talented, and dedicated. It has also been fun. I wish Jenni great success in the laboratory as well as the triatholon course.

Other members of the Atom Trainers have been very helpful, as well as being good friends. Steve Kadlecek, Paul Voytas and Renée Nesnidal all invested their time in teaching me the nuts and bolts of atom trapping. Ian Nelson and Bien Chann provided a wealth of good advice on navigating the rapids and doldrums of graduate school. The current members of the group, Earl Babcock, Erich Urban, and Jason Day have all provided support and companionship throughout the dissertation process, and to all I am grateful.

In the wider community of graduate students I am particularly fortunate to have found such a lively and supportive group of friends. From our first qual party together to the wedding ceremonies yet to come, John Peck, Brian Lepore, Brad Frazer, Jason Meaux and Bryan Fry have been great friends in fair weather and in foul. From Johnson street to the boundary waters, from San Jose to the 'bou, my happiness in Madison owes much to these gentlemen.

I am filled with gratitude for my parents and my brother, who have nurtured my curiosity and love for tinkering throughout my life. I could never have achieved this goal, or any other, without their unflagging support and belief in me. Thank you.

Sobre todo, yo quiero ofrecer mi gratitud a la persona quien hecho lo máximo para nutrirme y apoyarme durante este trabajao; mi esposa Adriana Reyes-Newell. Adriana, gracias por tu paciencia inagotable y fomento continuo. Tu estas como el sol para mi: surtir calor y luz y alimento con una generosidad inacabable. Muchissimas gracias por repartir tu brillo conmigo; gracias por causar mi a crecer y medrar.

Contents

List of Figures

Chapter 1

Introduction

1.1 Background and Motivation

Since the first demonstrations of Bose-Einstein Condensation [Bose, 1924], [Einstein, 1924] in dilute gasses were made [Anderson *et al.*, 1995] [Bradley *et al.*, 1995] [Davis *et al.*, 1995a], a great deal of effort has been invested in simplifying the experimental requirements for achieving this goal. Bose-Einstein Condensation (BEC) is an unusual state of matter which occurs when atoms are so cold and so densely packed that their quantum wavefunctions overlap and interact with one another. A group of atoms will form a BEC when their density, n, times the cube of their deBroglie wavelength reaches a critical value, approximately 2.6. This product, $n\lambda_{dB}^3$ is known as the phase space density, and is a convenient figure of merit for determining how close an atom cloud is to quantum degeneracy.

Conventional magneto-optical atom traps (MOTs), which rely on spontaneous-force cooling, can reach temperatures of a few microkelvin and maximum atomic densities on the order of 10^{11} cm^3. As remarkable as these low temperatures are, however, MOTs remain limited to maximum phase space densities between 10^{-4} and 10^{-6}. It is not

possible to increase the density further, as photon rescattering creates an effective repulsion between the atoms [Walker *et al.*, 1990, Ketterle *et al.*, 1993]. Nor is it possible to attain lower temperatures in MOT, as the recoil momentum attained from photon scattering cannot be avoided.

To increase phase space density further, it is necessary to employ a different type of atom trap which does not suffer these limitations. The original demonstrations of BEC began with a MOT but proceeded to transfer the atoms to a magnetic trap. Since pure magnetic trapping does not require any light, the effects of photon scattering are avoided. Cooling in the magnetic trap was performed through evaporation- a chirped radio-frequency electric field (the "RF knife") selectively ejected hotter atoms from the trap, leaving those which remained with a lower average temperature.

With this forced evaporative cooling, it is possible to increase phase space density to quantum degeneracy. The method is inherently inefficient, however, since it requires that the vast majority of the atoms initially in a trap be thrown away. Since effective evaporative cooling requires that the atoms make several elastic collisions with one another to rethermalize, the speed and efficiency of evaporation depend strongly on the initial density in the trap. In the magnetic traps described in the literature, starting densities tend to be low, so evaporation to BEC typically takes tens of seconds and requires the ejection of 99.9% or more of the initial sample.

It would therefore be advantageous to perform evaporative cooling in a trap which begins with higher-density samples. An excellent candidate is the Far-Off Resonance Trap (FORT) in which atoms are held at the focus of intense laser beam. Evaporation is performed simply by decreasing the intensity of the FORT laser.

A particular advantage of the FORT is that novel geometries are possible when multiple laser beams are made to interfere with each other, and the resulting periodic array of interference fringes creates a lattice of traps. Each trap within the lattice is

tightly confining, with large oscillation frequencies and very high densities.

This dissertation describes the development and characterization of a novel Holographic Atom Trap (HAT), which collects ^{87}Rb atoms in the interference pattern created by five intersecting beams from an Nd:YAG laser operating at λ= 1064 nm. The individual lattice sites, known as microtraps, gather as many as 18,000 atoms each from a MOT. After a brief period of free evaporation, atoms in the HAT reach a stable temperature of 50 μK, a density of $> 10^{14} cm^{-3}$, and a phase space density as high as 1/260.

We have performed a number of experiments with forced evaporative cooling in the HAT. Decreasing the Nd:YAG laser intensity leads to dramatic cooling as the hottest atoms preferentially leave the trap. Technical difficulties have to date limited the phase space density to one-third the value required for BEC, but the process is now well understood and progress is well underway to overcome these obstacles.

Evaporative cooling to degeneracy in the HAT would represent a significant advance in the field. The experimental apparatus required is substantially less costly than that needed for magnetic trapping, and much more convenient than previously reported optical traps [Barrett *et al.*, 2001]. Our trap is loaded from a standard vapor-cell MOT, as opposed to more complicated double-chamber MOT preparation and loading systems frequently employed to achieve BEC. Further, our optical geometry requires access in only one vacuum chamber window, and no optics or instruments inside the vacuum system. For these reasons and others, the Holographic Atom Trap constitutes an intriguing platform for further study of high-density samples and evaporative cooling to BEC.

1.2 Summary of the dissertation

This dissertation begins by presenting a new non-destructive method for imaging trapped atoms, known as Spatial Heterodyne Imaging. A weak, nearly-resonant probe beam passes through the atom cloud, and a stronger reference beam derived from the same laser passes around it. The two beams are made to intersect on a CCD camera, and computer software demodulates the resulting interference pattern to reconstruct the effect of the atom cloud on the probe beam. The result is a measurement of the index of refraction of the trapped atom cloud.

Spatial Heterodyne imaging has a number of advantages over previously reported imaging systems. Foremost, it is a non-destructive method; the probe beam can be made very weak (we have used ~ 500 nW/cm^2) and detuned far from resonance (11 Γ) with the atoms. Unlike other non-destructive methods, Spatial Heterodyne imaging does not require custom fabrication of micron-sized $\lambda/4$ retardation plates. Furthermore, it is easily adapted to a wide range of spatial scales, and makes better use of the detector's full dynamic range.

Chapter 2 describes the theory of Spatial Heterodyne imaging, the experimental apparatus used, and presents sample results. In particular, we present images of a MOT taken with fewer than 0.0004 photons scattered per atom. These results were published in [Kadlecek *et al.*, 2001].

Chapter 2 also describes the absorption imaging technique we use to measure the number of atoms in our trap. Though destructive to the trap, this imaging method enjoys a self-calibrating feature which makes absolute number measurements straightforward. We also describe the use of an optical pumping "image booster" beam which increases the signal by more than a factor of ten when used with absorption imaging.

Chapter 3 describes our Magneto-Optical trap (MOT). While not a central focus of

this dissertation, the MOT apparatus is central to the following chapters and is thus presented in detail.

The central development of this work, the Holographic Atom Trap, is presented in Chapter 4. We begin with a derivation of the dipole force acting on an atom in an off-resonant laser field and show how a confining, conservative potential well can be generated. We show that the density of atoms in the trap increases as the spatial extent of the potential well is decreased. This motivates our development of an optical lattice in which the interference pattern of five beams confines atoms in an array of microtraps. This array constitutes the Holographic Atom Trap.

Chapter 4 continues with a description of the experimental apparatus used to create and manipulate the HAT. The optimized loading procedure whereby atoms are transferred from the MOT into the HAT is presented. The chapter concludes with a description of the measurements which indicate a 5.2 $\times 10^5$ atoms at a temperature of 50 μK, a trap lifetime of 850 milliseconds, and a peak phase space density of 1/260 in the HAT. The peak density in the HAT is very high: 2×10^{14} cm^{-3}. These results were published in [Newell *et al.*, 2003].

The periodic array of small, high density clouds of atoms is particularly attractive for experiments involving ultracold Rydberg atoms; excitation of Rydberg states with principal quantum number near 50 would create long-range dipole-dipole interactions with a spatial extent comparable to the size of a microtrap. We have estimated that the interaction energy between two atoms on opposite sides of a microtrap is greater than 1 MHz [Saffman and Walker, 2002]. As a result, a narrow-band laser tuned to the Rydberg transition should excite no more than one atom. This "dipole blockade" raises a number of interesting possibilities for quantum information processing [Lukin *et al.*, 2001], single-atom sources, and single-photon sources.

We have found that the temperature of atoms in the HAT is determined by the

maximum trap depth, and is not affected by laser cooling. Free evaporation occurs rapidly in the trap, and the temperature quickly falls to one-tenth the trap depth. Chapter 5 summarizes these results. Several possible heating mechanisms are proposed and their effects estimated; none is found to be large enough to explain the inhibition of laser cooling in the HAT. We believe that laser cooling is spoiled by a two-photon Raman process driven by multiple longitudinal modes in our flashlamp-pumped YAG laser. The two-photon Raman rate is estimated to be comparable to the excited state lifetime, leading to considerable mixing of the excited states. A test experiment to examine this effect is proposed, and possible remedies are discussed.

Having seen that the temperature in the HAT is determined by evaporation , we turn our attention to forced evaporative cooling in Chapter 6. In forced evaporative cooling, we decrease the intensity of the YAG laser in a controlled manner so that atoms with higher thermal energies are ejected and the remaining sample has a lower temperature. A theoretical model and a computer simulation for this process are presented.

We have studied a variety of decreasing intensity ramps in search of the highest possible final phase space density. Our best data so far, a phase space density of $0.91^{+1.1}_{-0.5}$, was achieved through a piecewise-optimized linear decrease in intensity. Collisions with untrapped background atoms are identified as the limitation preventing further increase in phase space density.

Analysis of our experimental data and the predictions of our computer model suggest that we define a figure-of-merit which assesses the possibility of evaporation to BEC. This figure of merit is the ratio of the rate of elastic collisions between trapped atoms to the rate of collisions with untrapped atoms in the background gas. Efficient evaporation requires that the elastic collision rate be large relative to the background collision rate. For our current initial conditions in the HAT we find this ratio to be 1.0×10^4. Our computer model suggests that forced evaporation can result in quantum

degeneracy only if this ratio is 3.3×10^4 or higher. We believe that it is not possible for us to increase the elastic scattering rate within our HAT further. This last small increase is most likely to be achieved by improvements made to the vacuum chamber.

Chapter 2

Spatial Heterodyne Imaging System

2.1 Introduction

This chapter presents the development and characterization of the Spatial Heterodyne Imaging system. This system measures the index of refraction of a cloud of atoms over a wide range of spatial sizes and without the need for specially-fabricated optics. Spatial Heterodyne imaging is a non-destructive technique, and we demonstrate images with a signal-to-noise ratio greater than ten made with fewer than 0.0004 photons scattered per atom.

We begin with a review of previously developed non-destructive imaging systems, including Phase Contrast imaging (Section 2.2.3). Spatial Heterodyne imaging is introduced in Section 2.3 and the theory behind it in Section 2.4. The experimental apparatus is described in Section 2.5 and sample images are seen in Section 2.7.

2.2 Background

2.2.1 Absorption imaging

A number of techniques have been employed to image small, dense clouds of atoms. The simplest of these, absorption imaging, suffers a number of significant drawbacks. This method consists of a collimated beam of light tuned near resonance passing through the atom cloud. As the atoms absorb photons from the beam they create a shadow which is projected onto a detector by an imaging lens.

A disadvantage of absorption imaging is that it can easily be too sensitive, scattering too many photons out of the probe beam. The scattering cross section is given by

$$\sigma = \sigma_0 f_e \tag{2.1}$$

The on-resonant optical density of an atom cloud of width l and density n is

$$D_0 = nl\sigma \tag{2.2}$$

which, for a modest MOT with $n = 10^{10}$ cm^{-3} and l= 5 mm, is 4. Thus an on-resonant probe beam would be attenuated by e^{-4}, or down to 1.8%. Since atomic densities in our HAT are $\sim 10^{14}$ cm^{-3}, even the outermost parts of the trap would be completely opaque, and all spatial information would be lost. Furthermore, taking the picture would substantially affect the atoms, as they would be optically pumped and heated by the probe beam.

We could work around these problems by detuning the imaging light from resonance; the optical density for detuned light is decreased by increasing Δ.

$$\sigma' = \frac{\sigma}{1 + 4\Delta^2/\Gamma^2} \tag{2.3}$$

$$D' = \frac{OD_0}{1 + 4\Delta^2/\Gamma^2} \tag{2.4}$$

This creates a second problem, however. As the detuned imaging light travels through the cloud of atoms, it accumulates a phase shift according to

$$\phi = \sigma' nl \times \frac{\Delta}{\Gamma} \tag{2.5}$$

Since we would like an optical density D' on the order of unity, equation 2.4 compels us to choose Δ such that $\Delta/\Gamma \sim \sqrt{D_0}/2$ which implies $\phi \sim \sqrt{D_0}/2$. Given $D_0 > 4$ for even a modest MOT and is well over 100 for our HAT, this is a large phase shift indeed.

If the cloud of atoms is spatially uniform over the width of the probe beam, this phase shift corresponds to a bulk retardance of the light and is of little consequence. We seek to image the atom cloud, however, and not merely detect it, so it is necessary to use a probe beam which is much wider than the atom cloud. In this case, the portion of the beam which passed through the atoms is phase shifted, but the rest is not. In effect, the atom cloud is region with higher index of refraction, and it distorts the probe beam just as a lens would . As a rule, because the absorption falls as $1/\Delta^2$ but the phase shift only falls as $1/\Delta$, it is difficult to chose a detuning that provides a satisfactory absorption signal without an unacceptably large phase shift.

One solution is to image the atoms by measuring the phase shift rather than the absorption. Several schemes have been demonstrated that do this. The simplest of these methods, called Dark-ground imaging, is common in microscopy and was first used to image atom clouds by Andrews *et al.* [Andrews *et al.*, 1996].

2.2.2 Dark-ground imaging

For dark-ground imaging [Hecht, 1987] a lens is placed in the probe beam after it passes through the atoms. A small opaque object is centered in the fourier plane of the lens. Light which is unperturbed by the atoms is focused onto the opaque object and blocked

by it. Light which is deflected by the higher-index atom cloud passes around the opaque object and is projected onto a screen or camera. The dark-ground imaging technique can be thought of as the opposite of a standard spatial filter: the dc component of a collimated beam is blocked, while high frequency spatial information is allowed to pass. Andrews *et al.* used laser detuned 342 Γ to the red of resonance with with the $F = 1$ to $F' = 2$ transition in sodium. They employed a thin wire stretched across the focal place of the imaging lens to block the dc component of the imaging beam. Using this method Andrews *et al.* were able to take as many as 100 consecutive images of a BEC without generating measurable heating.

Formally, this process can be described as follows. Consider the probe beam as a simple set of plane waves propagating in the $\hat{x}$-direction.

$$E_i(t) = E_0 \sin(\omega t) \tag{2.6}$$

Immediately after passing through the cloud of atoms, the beam has picked up a spatially varying phase shift $\phi(y, z)$

$$\begin{aligned} E_{PM}(y, z, t) &= E_0 \sin[\omega t + \phi(y, z)] && (2.7) \\ &= E_0 \sin \omega t \cos \phi + E_0 \cos \omega t \sin \phi && (2.8) \end{aligned}$$

In the limit of small ϕ this can be approximated as

$$E_{PM}(y, z, t) = E_0 \sin \omega t + E_0 \phi(y, z) \cos \omega t \tag{2.9}$$

The first term does not depend on ϕ and is the contribution from the source plane wave, the second term contains the phase shift information. At the focal plane of the imaging lens, the E-field distribution is the y-z Fourier transform of E_{PM}: the first term has no y or z dependence and so generates a single spot on axis; the y and z dependence of ϕ spreads that information across the fourier plane. The opaque object

at the center of the fourier plane thus blocks the first term (and the zero-frequency component of the second) but permits higher spatial frequency information to pass. The image that results is essentially dark, as we have blocked the majority of the light. An unfortunate drawback to this system is that the measured intensity

$$I(y,z) = |E_{PM}|^2 = [\phi(y,z) \times E_0 \cos \omega t]^2 \tag{2.10}$$

is not linear with respect to ϕ; in particular, if ϕ changes sign over the object there will be a contrast reversal. A further limitation is that some distortion of the image is unavoidable: since the opaque object must have some physical extent, it is bound to remove a range of spatial frequencies from the fourier transform of ϕ, not just the zero-frequency part. Given knowledge of the size of the phase object being measured, it is possible to optimize the size of the opaque beam block, but some distortion remains.

2.2.3 Phase contrast imaging

A more useful implementation of this method is the Phase Contrast technique [Hecht, 1987]. This arrangement is similar to the Dark-Ground system, but with the small opaque object replaced by a small $\pi/2$ phase plate. In this case the unperturbed probe beam and the phase shifted light interfere on the imaging plane so that the phase modulation is transformed to an intensity modulation. To see this, we write equation 2.9 with a $\pi/2$ phase shift:

$$\begin{aligned} E_{PM}(y,z,t) &= E_0 \sin\left(\omega t + \frac{\pi}{2}\right) + E_0 \phi(y,z) \cos \omega t & (2.11) \\ &= E_0[1 + \phi(y,z)] \cos \omega t & (2.12) \end{aligned}$$

The resulting intensity distribution on the image plane is a bright field with a spatially varying intensity which directly corresponds to $\phi(y,z)$. As with dark-ground imaging, the spatial resolution of the system is affected by the size of the phase plate placed at the

focus of the imaging beam. The first demonstration of the phase-contrast technique to image atoms, by Andrews *et al.* [Andrews *et al.*, 1997], used a glass slide with a raised dot 500 μm in diameter. The thickness d of the raised dot was chosen so that $(n_{glass} - 1)d = \lambda/4$ and it imparts a $\pi/2$ phase shift relative to light which does not pass through the dot. Just as with dark-ground imaging, the probe laser was detuned very far off resonance (1.7 GHz, or 170Γ) to minimize the probability of scattering and reduce the phase shift to manageable levels.

Since its first demonstration in 1997 the phase contrast method has been widely used to image small and dense atom clouds. A primary drawback to this method is need for precision fabrication and alignment of the $\sim 500 - \mu$m $\pi/2$ phase plate. Furthermore, since the spatial resolution of the imaging system is determined by the size of the phase element, it is necessary to fabricate multiple phase plates if one wishes to image clouds of different sizes.

To overcome some of the shortcomings of these methods, we have developed a Spatial Heterodyne imaging technique. It is a nondestructive method, capable of imaging with fewer than 0.001 scattered photons per atom, and it requires no specially fabricated components. It is robust against imperfect optics such as vacuum chamber windows, and it can achieve a figure of merit (signal to noise ratio per scattered photon) higher than phase contrast imaging.

2.3 Spatial Heterodyne

Our Spatial Heterodyne imaging technique [Kadlecek *et al.*, 2001], seen in Figure 2.1, is analogous to lock-in detection, with the modulation taking place in the spatial domain instead of the temporal domain. A collimated near-resonant probe beam passes through the atoms and is incident on a CCD camera. A lens in the probe beam projects the

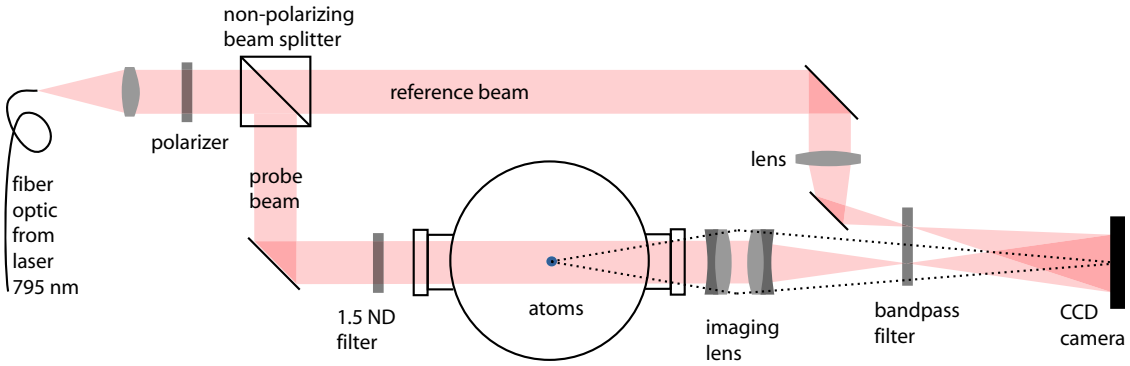

Figure 2.1: Spatial Heterodyne Imaging apparatus

plane of the atoms onto the camera. A reference beam, derived from the same laser and thus coherent with the probe beam, goes around the atoms and strikes the same CCD camera. The resulting interference pattern is a set of straight line fringes, with a slight shift in the center where the atoms induced a phase shift on the probe beam. With our analysis computer we take the Fourier transform of this image, shift it so that the fringes are at zero spatial frequency, filter out higher spatial frequencies, and take the inverse Fourier transform. The result is an image of the phase shift induced on the probe beam by the atoms. Given the detuning of the imaging laser, the number of atoms can then be easily calculated.

2.4 Theory

Consider the interference pattern of two beams of coherent light, a probe beam with intensity I_p and a reference beam with intensity I_r. If the beams have equal radii of curvature, and converge at an angle θ, we can write the resulting intensity distribution

of their interference pattern as

$$I(\mathbf{x}) = I_r + I_p + 2\sqrt{I_r I_p}\ \ cos\left(\delta + 2\pi\theta\hat{k_\perp} \times \frac{\mathbf{x}}{\lambda}\right) \tag{2.13}$$

where δ is an overall phase shift between the beams. If we now place in the probe beam an object which creates a spatially-varying phase shift $\phi(\mathbf{x})$, this shift affects the interference pattern:

$$I(\mathbf{x}) = I_r + I_p + 2\sqrt{I_r I_p}\ \ cos\left(\delta + 2\pi\theta\hat{k_\perp} \times \frac{\mathbf{x}}{\lambda} - \phi(\mathbf{x})\right) \tag{2.14}$$

We now consider two cases in which extraction of the phase information $\phi(\mathbf{x})$ is straightforward: parallel mode and tilted mode.

2.4.1 Parallel mode

If we are interested in resolving phase objects of length scale σ we can define parallel mode imaging as the case in which the angle θ is small compared to σ/λ. In this configuration the interference pattern is essentially a uniformly illuminated field with a bright or dark spot in the center corresponding to $\phi(\mathbf{x})$. More rigorously, it is

$$\begin{aligned} I(\mathbf{x}) &= I_r + I_p + 2\sqrt{I_r I_p}\ \ \cos\left(\delta - \phi(\mathbf{x})\right) && (2.15)\\ &= I_r + I_p + 2\sqrt{I_r I_p}\ \ \sin(\phi(\mathbf{x})) && (2.16) \end{aligned}$$

where in the last step we've assumed $\delta = \pi/2$. The localized phase difference created by the atoms becomes a localized intensity difference on the detector, just as in phase contrast imaging. Two important advantages remain, however: we can increase the intensity of the reference beam, or decrease the intensity of the probe beam, or both, and thereby increase the signal size by $\sqrt{I_r/I_p}$. Further, we have retained the full spatial resolution of the camera, no averaging over multiple pixels required.

To implement parallel mode imaging, it would be necessary to actively stabilize the path length difference between the two beams to ensure $\delta = \pi/2$. If δ were to be held fixed at some value other than $\pi/2$ it would still be possible to reconstruct $\phi(\mathbf{x})$, although the sensitivity of the detection would be reduced. We have not implemented parallel mode imaging, due to the technical requirements involved.

2.4.2 Tilted mode

An alternate configuration in which $\phi(\mathbf{x})$ can be readily deduced is one in which $\theta \gg \sigma/\lambda$. In this case a series of fringes appears on the detector, with fringes in the center shifted spatially by the phase shift induced by the atoms. The image is then processed in a manner analogous to lock-in detection: we take the 2D spatial fourier transform of the image, shift the spatial frequency corresponding to the fringes to zero spatial frequency, and apply a low-pass filter to the result. The image that is produced is a map of the spatial phase shift of the fringes, and thus directly corresponds to the induced phase shift $\phi(\mathbf{x})$. Operating in the tilted mode does not require active stabilization of any optics.

2.5 Apparatus

2.5.1 Imaging laser

We use a custom-built extended cavity diode laser in the Littrow configuration for our imaging laser. The laser is detuned from resonance with the $^2S_{1/2}$ $F = 1$ to $^2P_{1/2}$ $F' = 2$ transition at 795.0 nm. Following the work of Lancaster *et al.* [Lancaster *et al.*, 2000] this laser was built with a diode using a cylindrical focusing element in the output window which circularizes the beam (Blue Sky Research PS026), making an anamor-

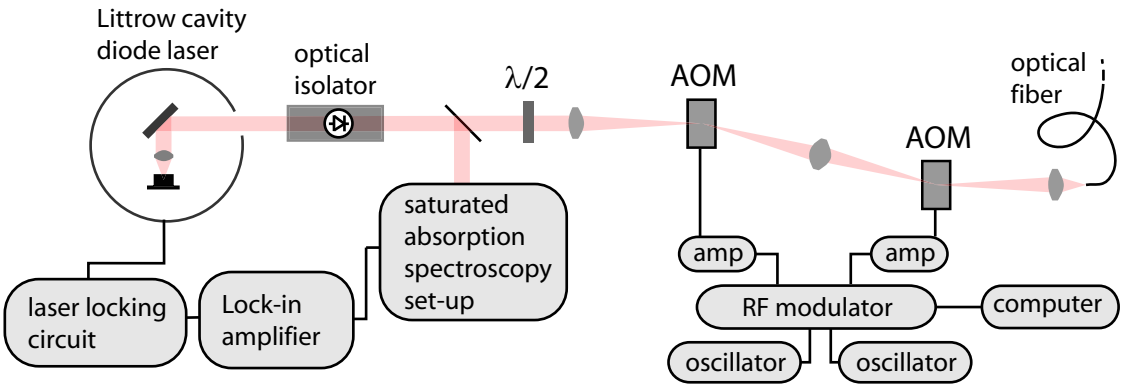

Figure 2.2: Diagram of the imaging laser apparatus

phic prism pair unnecessary. The diode's free-running wavelength is 787 nm at room temperature, so it must be heated with a Peltier thermoelectric device and feedback circuit in order to operate at 795 nm. Using an 1800 line/inch grating the laser delivers 14.5 mW of power. A small amount of light is picked off with a polarizing beam splitter and sent to a saturated absorption spectroscopy setup. The laser is locked to the ${}^2S_{1/2}$ $F = 1$ to ${}^2P_{1/2}$ $F' = 2$ feature with a lock-in amplifier and feedback circuit. The frequency of the light is shifted $+\delta_1$ and $-\delta_2$ by two AOMs, so that the final detuning from resonance is the difference between the two. The light is coupled into a single-mode fiber and carried to the chamber table.

When imaging the atoms we want to generate an pulse of light which is as short as possible so that movement of the atoms during the exposure does not blur the image. This is done by chopping the RF power applied to the AOMs so that light is coupled into the fiber only when they are on. In practice we have found that this is not trivial: the application of RF power (typically around 1 Watt) to the AOM's transducer generates a temperature gradient inside the crystal. This gradient slightly changes the orientation of the acoustic standing waves and consequently steers the

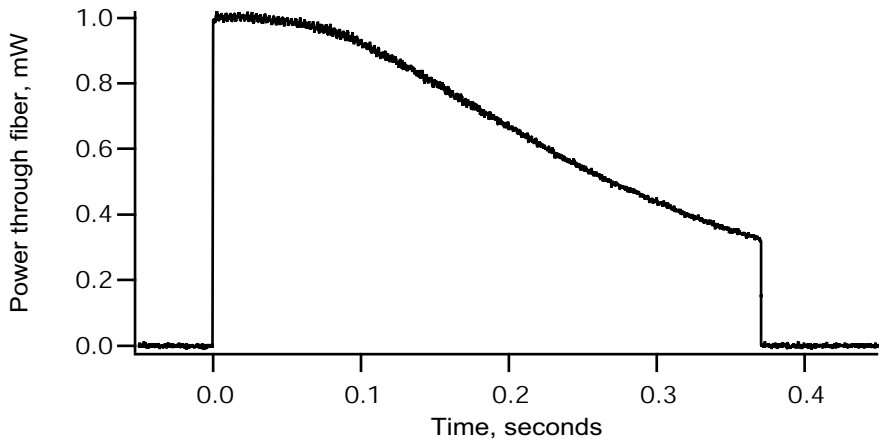

Figure 2.3: Temporal profile of imaging laser pulse through fiber. Note that our usual 100 μs pulse only samples the leading edge.

diffracted beams to the side. When RF power is applied constantly, the temperature gradient is stable and the diffracted orders do not change their steering, but when power is first applied the diffracted beams swing as much as 10 mRad to the side. This is more than enough to spoil the fiber coupling and prevent light from reaching the chamber table. Our solution has been to use a pulse generator to make a series of short RF pulses separated by several seconds and couple the fiber so for maximum transmission of the leading edge of the pulses. The fiber is then poorly coupled in the case of constantly-on AOMs, but is well coupled for short bursts of light. We typically receive 1 mW from the fiber at the beginning of a pulse, falling to 0.2 mW in steady-state (see Figure 2.3).

2.5.2 Probe and reference beams

A diagram of our spatial heterodyne imaging apparatus appears in Figure 2.1. Following the fiber the imaging light is collimated to 2.64 mm waist and linearly polarized

by a filter. A 50/50 non-polarizing beam splitter cube separates the light into probe and reference beams, the reference beam is directed around the trapping chamber and the probe beam is sent through the center. Each beam can be blocked by a computer controlled shutter. A neutral density filter with optical density 1.5 attenuates the probe beam before it enters the chamber. The choice of a cube beam splitter is convenient, but not ideal for our application. The parallel input and output faces produce interference fringes which tend to move from one picture to the next, ultimately degrading the signal to noise on the processed image. A beam splitter without parallel faces, such as a pellicle or coated wedge, would be preferable.

The plane of the MOT is projected onto the CCD camera with a pair of achromatic doublet lenses with focal lengths of $f = 150$ mm (Newport PAC086) and $f = 750$ mm (PAC094). The magnification of this system is 1:4.8 and we believe the aberrations are limited to contributions from the vacuum chamber window.

An $f = 125$ mm planoconvex lens in placed in the reference beam so that its focal plane coincides with that of the probe beam. The two beams then diverge with the same radius of curvature, so that the resulting interference fringes will be straight lines. A bandpass interference filter centered at 795 nm is used to prevent unwanted background light, particularly MOT fluorescence, from reaching the camera. We have found that placing this filter at the focal plane of the two lenses substantially reduces the unwanted fringes it creates in the imaging beams, presumably because those beams sample smaller regions of the filter.

2.5.3 Detector

Both beams are incident on our Hamamatsu ORCA-ER CCD camera. This device has a number of features which make it well-suited to our application: its small pixel size

(6.45 μm square) helps with the loss of resolution inherent in tilted-mode imaging, its 1344 $\times$ 1024 format is easily masked to 1024 $\times$ 1024 for efficient fast-Fourier transform processing, and it has a reasonably high quantum efficiency (16%) at 795 nm. The camera's analog-to-digital converter has an overall efficiency of 4.6 counts per photo-electron. This camera also enjoys a low read-noise level of 8 electrons and a full-well capacity of 18,000 electrons, for a total dynamic range of 2250:1.

2.5.4 Software

Images are downloaded from the camera with a digital image-acquisition board (National Instruments PCI-1422) and processed with a LabVIEW program. This program controls all the timing signals which set the lasers' detunings, intensities, and magnetic field strength. Running on a 2.0 GHz Pentium-4 processor it takes and analyzes images in approximately 30 seconds.

2.6 Procedure

Once a cloud of atoms has been trapped in the MOT or HAT, a series of five exposures begins. In each instance the camera's electronic shutter is opened for several hundred milliseconds during which time a pulse of RF power (typically 100 μsec) is applied to the imaging laser's AOMs and a pulse of light is sent to the atoms. After each exposure a 1024 pixel $\times$ 1024 pixel area of the CCD is read out and the image is stored in memory.

To image atoms in the HAT, atoms are loaded in under the desired conditions, then the YAG beam is extinguished 1 microsecond before the first exposure pulse begins. It is possible to image the atoms with the YAG still on, but the spatially varying AC stark shift effectively changes the detuning of the imaging laser and thus the sensitivity

of detection over the image. It is very difficult to extract the phase information $\phi(\mathbf{r})$ from the image if the probe detuning is varying rapidly.

The second exposure is made several seconds after all trapping lasers and magnetic fields have been extinguished; it is a picture with no atoms used for background subtraction. The final three images are taken with the probe beam only, the reference beam only, and both beams blocked.

After all five images have been taken and downloaded, processing begins. The probe-beam-only, reference-beam-only, and no-beam pictures are subtracted from the fringes-with-trap and fringes-with-no-trap pictures. This removes the I_r and I_p terms from equation 2.14 leaving only the signal term. We then calculate the discrete 2D fourier transform of the image with the trapped atoms. The real component of the resulting pattern in the frequency plane is a large peak centered around zero spatial frequency and two peaks containing the fringe information centered at $k_0 = 2\pi\theta/\lambda$. We multiply the real component by $\cos(k_{0,x}x + k_{0,y}y)$ and the imaginary component by $\sin(k_{0,x}x + k_{0,y}y)$, which serves to shift the complex image by $e^{i\mathbf{k_0}\cdot\mathbf{r}}$. Now the information which was at the spatial frequency of the fringes is at zero spatial frequency, and what was at zero spatial frequency has been shifted to appear as fringes.

Once the demodulation has taken place, we apply a low-pass filter to the images in frequency space. This is done by multiplying the real and complex parts of the image by the asymmetric Gaussian filter

$$I(k_\parallel, k_\perp) = I_0 \ \exp\left[-\left(\frac{s\ k_\parallel}{k_0}\right)^2 - \left(\frac{s\ k_\perp}{a\ k_0}\right)^2\right] \tag{2.17}$$

Here $k_\parallel$ and $k_\perp$ are the coordinates of a point in phase-space k_x and k_y expressed in terms of unit vectors parallel and perpendicular to the fringe k-vector k_0. The filtering width factor s determines the size of the filter: frequency components s pixels away from zero are suppressed by $1/e^2$. The asymmetry factor a is used to make the filter less

restrictive along the axis parallel to the fringes. This permits higher spatial resolution in this direction, since more information at high spatial frequency is retained.

After filtering, we take the inverse fourier transform of the image and calculate the phase angle $\phi = \tan^{-1}[Imaginary(I(x,y))/Real(I(x,y))]$ to reveal a map of the phase shift $\phi(x,y)$ between the probe and reference beams. We apply the same procedure to the picture taken without atoms in the probe beam, and subtract it from the processed picture with the atoms. The result is an image of the phase shift created by the atom cloud.

2.6.1 Photon scattering rate

The rate at which atoms absorb and scatter photons from the imaging beam is given by the off-resonant absorbtion cross-section times the photon fluence.

$$R = \frac{\sigma_0 f_e}{1 + 4\Delta^2/\Gamma^2} \times \frac{I}{hc/\lambda} \tag{2.18}$$

Here σ_0 is the on-resonance cross-section $\sigma_0 = 4\pi r_e c/\gamma$, $f_e = 5/18$ is the oscillator strength of the $^2S_{1/2}\ F = 1 \rightarrow\ ^2P_{1/2}\ F' = 2$ transition, $\gamma = (2\pi) \times 5.98$ MHz is its natural lifetime, and I is the intensity of the probe beam. For an exposure that lasts T seconds, the total number of photons scattered is $N = RT$. Our typical imaging pulse contains $\simeq 0.1$ mW/cm^2, lasts 50 μs, and is detuned $\Delta = -1\Gamma$ from resonance. We therefore calculate 0.5 photons scattered per atom. We have shown that we can image the MOT with detunings as large as -11Γ and fluences as low as 61 pJ/cm^2, corresponding to 0.0004 photons scattered per atom.

We are able to correct our phase shift measurements for the effects of photon scattering. This is necessary because an atom which absorbs a photon has some probability of decaying to the wrong ground state and ceasing to interact with the imaging laser. If an atom has two hyperfine ground states F=1, 2 and the branching ratio to decay

to the F=2 level is B_2, the probability that an atom which started in the F=1 state remains there is given by

$$P_1 = e^{-R \cdot B_2 \cdot t} \tag{2.19}$$

after being exposed to the imaging light for a time t. If the imaging laser is coupled to the F=1 state, the average phase shift measured during the exposure is decreased by the loss of atoms from that state:

$$\langle \phi \rangle = \phi_0 \times e^{-R \cdot B_2 \cdot t} \tag{2.20}$$

Integrating t over the total exposure time T we find

$$\langle \phi \rangle = \frac{\phi_0}{N B_2} \left(1 - e^{-N B_2}\right) \tag{2.21}$$

Thus we can multiply our measured phase shifts $\langle \phi \rangle$ by $N B_2/(1 - e^{-N B_2})$ to correct for optical pumping into the F=2 state. In practice we have found that this correction is necessary only for optically thin samples.

2.7 Results

Figure 2.4 shows a spatial heterodyne image of our magneto-optical trap. This image was taken with the imaging laser detuned 11 Γ from resonance, and with a neutral-density ND=1.2 filter in the probe beam. We thus calculate that an average of 1.2×10^{-3} photons were scattered per atom during this exposure.

Figure 2.5 is an image of the same magneto-optical trap taken with an ND= 1.5 filter in the probe beam. Even with the ratio of the reference beam and probe beam intensities at 60:1, we still find a signal-to-noise ratio greater than ten for this image. The corresponding scattering rate is 4×10^{-4} photons scattered per atom. The amount of heating caused by this pulse of imaging laser light is easily calculated (see Section

Figure 2.4: Spatial Heterodyne image of MOT with imaging laser detuning of 11Γ and reference to probe intensity ratio of 20:1.

5.5.1). The momentum imparted by one scattering event is $\hbar^2\ k^2/m = 365$ nK, so on average the atoms were heated by 0.15 nK by the imaging process which led to Figure 2.5.

Figure 2.6 shows a representative image of the Holographic Atom Trap. This image was made with the probe laser detuned 3Γ from resonance. By fitting a gaussian peak to cross sections of the central Talbot fringe, we find the maximum phase shift to be 0.56 radians, the width ($1/e^2$ radius) in the z-direction to be 28 μm, and the width in the x-direction to be 43 μm. This corresponds to 335,000 atoms in the center Talbot fringe. The standard deviation of phase shifts in the background of this picture is 0.239 radians, so we conclude that the signal-to-noise ratio is 24.

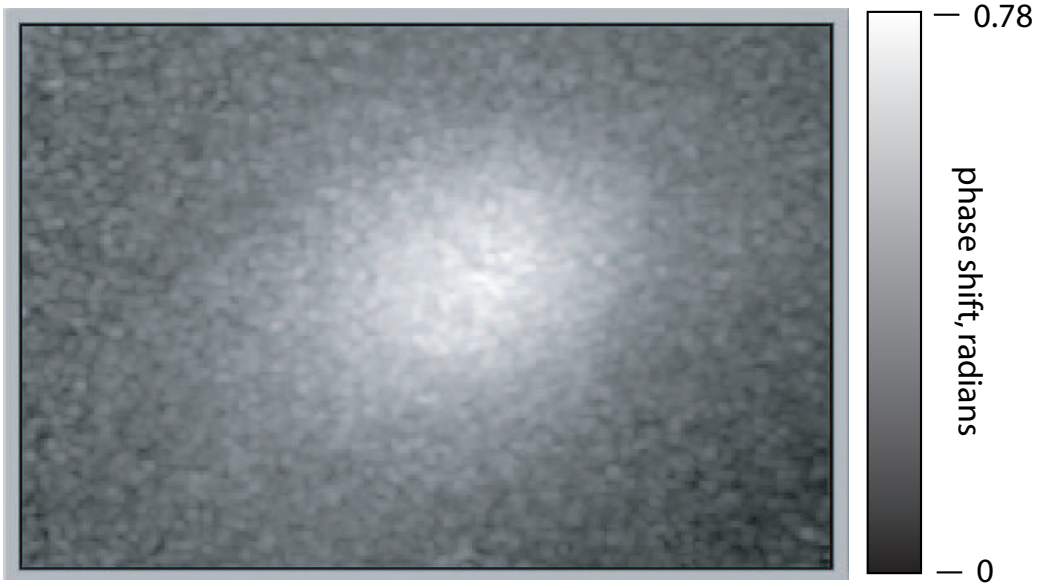

Figure 2.5: Spatial Heterodyne image of MOT with imaging laser detuning of 11Γ and reference to probe intensity ratio of 60:1. This corresponds to 0.0004 photons scattered per atom.

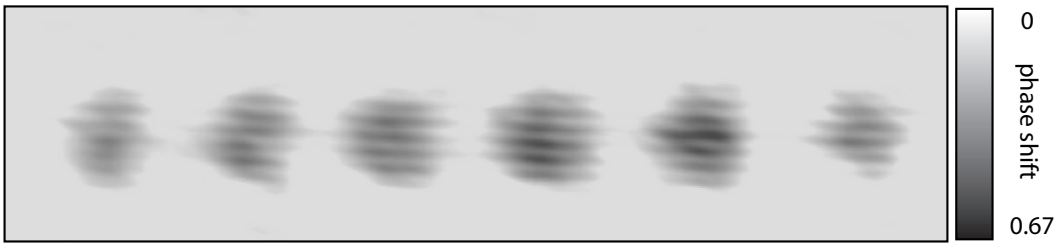

Figure 2.6: Spatial Heterodyne image of taken with probe laser detuning of 3Γ

2.8 Absorption Imaging

2.8.1 Introduction

This chapter briefly describes absorption imaging. We have found absorption imaging to have superior signal-to-noise characteristics when the camera's read-noise is significant, discussed in Section 2.8.2. Absorption imaging enjoys a self-calibration feature which makes measuring the number atoms particularly straightforward. When calibration is not important, the signal can be enhanced by a factor of 10 to 15 with the introduction of an optical pumping "image booster" beam. These points are discussed in the theory section, 2.8.3. Our experimental procedure and representative images are presented in Sections 2.8.5 and 2.8.6. Despite these advantages, absorption imaging remains a destructive process; Spatial Heterodyne imaging is clearly superior when an experiment calls for minimal perturbation of the atom cloud being imaged.

2.8.2 Comparison with Spatial Heterodyne

Despite its advantages, there are situations for which Spatial Heterodyne Imaging is not ideally suited. It excels when the atomic cloud is optically dense; diffuse optically thin clouds are more amenable to traditional absorption imaging methods. We have found that when performing time-of-flight temperature measurements on small cold samples, the expansion of the atomic cloud yields a signal which is too small and diffuse to give a measurable phase shift.

Further, we have found that in these cases the read noise of the CCD camera is the primary source of noise. Binning the camera's pixels together into 2x2, 4x4, or 8x8"superpixels" keeps the read-noise constant but increases the number of signal counts per pixel by the binning factor of 4, 16 or 64. Thus in low-light situations it

is advantageous to bin the pixels together until shot-noise becomes the limiting factor. Once the read noise becomes small compared to the shot noise, binning continues to improve the signal to noise ratio. Shot-noise scales as $\sqrt{N}$, where N is the number of counts in a pixel. Binning pixels together into, for example, 4x4 superpixels increases the signal N by 16, but the shot noise only rises by $\sqrt{N} = 4$.

Even 2x2 binning washes out the interference fringes necessary for Spatial Heterodyne imaging, so we must use absorption imaging to take advantage of this feature.

2.8.3 Theory

In the absence of any optical pumping effects, a beam of nearly resonant light is attenuated according to $e^{-n\,l\,\sigma'}$ where n is the volume density of atoms, l is the length of the atom cloud and σ' is the near-resonant scattering cross section given by equation 2.3.

In practice, the atoms are not able to scatter an arbitrarily large number of photons: after being excited there is a possibility that the atom will spontaneously decay to a different hyperfine ground state and become transparent to the imaging beam. We perform absorption imaging with the ${}^2S_{1/2}$ $F = 1$ to ${}^2P_{1/2}$ $F' = 1$ transition, for which the probability of reradiating to the ${}^2S_{1/2}$ $F = 2$ state is 1/2. Consequently, in the limit of long exposure time, each atom scatters an average of two $F = 1$ to $F' = 1$ imaging photons before being pumped into the $F = 2$ state. The intensity distribution seen by the camera is

$$I(\mathbf{r}) = I_p(\mathbf{r})\,(1 - N_\gamma\,h\nu\,n(\mathbf{r})\,l) \tag{2.22}$$

where $I(\mathbf{r})$ is the intensity of the probe beam, $h\nu$ is the energy per photon, $n(\mathbf{r})$ is the number density of atoms, l is the thickness of the atom cloud in front of location $\mathbf{r}$, and N_γ is the number of photons scattered per atom, two for this transition. In practice this is quite straightforward; the camera measures the number of photons incident on

a pixel, so it is more useful to write this in terms of incident photons per pixel, $P(\mathbf{r})$.

$$P(\mathbf{r}) = \frac{I_p(\mathbf{r})}{h\ \nu}\ (1 - N_\gamma\ h\nu\ n(\mathbf{r})\ l) \tag{2.23}$$

A nice feature of this method is its self-calibration property: since each atom in the sample scatters two photons, a measurement of the total number does not depend on the details of the imaging pulse.

In situations in which we wish to image very small numbers of atoms, it is possible to increase N_γ and thus the signal generated by each atom. We apply a beam of light resonant with the $^2S_{1/2}\ F = 2$ to $^2P_{3/2}\ F' = 2$ transition simultaneously with the imaging laser pulse. This light pumps any atoms which have decayed to the $F = 2$ state back into $F = 1$. This "image booster" beam permits each atom in the trap to scatter many photons from the imaging beam and thus increase the signal size. This is equivalent to multiplying the factor of N_γ in equation 2.23 by a factor η.

$$P'(\mathbf{r}) = \frac{I_p(\mathbf{r})}{h\ \nu}\ (1 - \eta N_\gamma\ h\nu\ n(\mathbf{r})\ l) \tag{2.24}$$

2.8.4 Apparatus

We perform absorption imaging by passing a probe beam resonant with the $^2S_{1/2}\ F = 1$ to $^2P_{1/2}\ F' = 1$ transition at 795 nm. This light is produced with the same diode laser and AOM setup described in section 2.5.1 and seen in figure 2.2. The absorption imaging probe beam is identical to that used by our spatial heterodyne setup, we merely block the spatial heterodyne reference beam. We have found that it is helpful to remove the 3 nm bandpass interference filter from the probe beam. Its peak transmission of 35% is low enough to degrade the signal to noise ratio of absorption images. We also remove the polarizing filter, since absorption imaging does not require any particular polarization of light, and the polarizer produces unwanted interference fringes in the beam.

The image booster beam is derived from the Ti:sapph laser (described later, see Section 3.2.1 and Figure 3.2). A beam of light +9 Γ from the $^2S_{1/2}$ $F = 2$ to $^2P_{3/2}$ $F' = 2$ transition is brought to the trapping table by an optical fiber and split by a beam splitter cube. 20% is used as the depumping beam for the MOT, as described in section 3.2.2. The other 80% passes through an AOM which shifts its frequency down 9 Γ so that it is on resonance with $F = 2$ to $F' = 2$ and can be turned on and off quickly. After the AOM the beam has a $1/e^2$ radius of approximately 1 mm and contains 800 μW of power for a peak intensity of 50 mW/cm^2. The beam enters the trapping chamber from below.

Image acquisition and analysis are performed with the same Hamamatsu ORCA-ER CCD camera and LabVIEW software used for spatial heterodyne imaging.

2.8.5 Procedure

Absorption images are generated through a simple background subtraction procedure. After an atom cloud has been prepared we initiate an acquisition with the CCD camera and apply a pulse of imaging laser light. The exposure time is variable and is chosen to maximize the signal to noise ratio for a given sample. After the first picture is taken, the atoms are dumped and a second exposure is taken of the probe intensity only. Finally the probe beam is blocked and an picture is taken of the dark background.

We subtract the dark background image from both the image with atoms and the image without. We then calculate the average number of counts in each of these two images. We have found that the total flux of photons on the camera will change by a few percent from one picture to the next as a result of variable coupling efficiency into the optical fiber. To compensate for this, we find the ratio of the average number of counts for the two images and multiply the second picture by this factor. Once this

compensation has been done, we subtract the image with no atoms from the image with atoms to recover the image.

This image is in units of photoelectron counts read by the camera. We convert this to number of incident photons by multiplying by the ADC's conversion efficiency of 4.6 photons/count and dividing by the quantum efficiency of 0.16. We have experimentally verified both of these values by exposing the camera to a pulse of known intensity and duration and summing the total number of counts. Both values agreed with the manufacturer's specifications within the uncertainty of the measurement.

Once the background subtraction and unit conversions are complete, we are left with an image of the number of photons removed from the probe beam. Typically we are interested in finding the number of atoms held within a single Talbot fringe (see section 4.2.4). This is done by summing up the photons absorbed in a window surrounding the Talbot fringe and dividing the result by η. It is essential to use a window that is no wider than the Talbot fringe period of 100 μm.

When we wish to measure the number of atoms in the trap, we need to find the value of the enhancement factor η. This is done by preparing a sample with enough atoms to have a good signal to noise ratio both with and without the imaging beam. We find the number of photons absorbed when the image booster beam is present and divide it by the number absorbed when the booster is absent. The result is $\eta/2$.

2.8.6 Results

Figure 2.7 displays the number of photons absorbed by one Talbot fringe as function of the incident pulse energy. The saturation of the absorption signal as atoms are optically pumped into the $F = 2$ ground state is clearly visible. We see that the maximum number of absorbed photons is reached with an incident energy of around

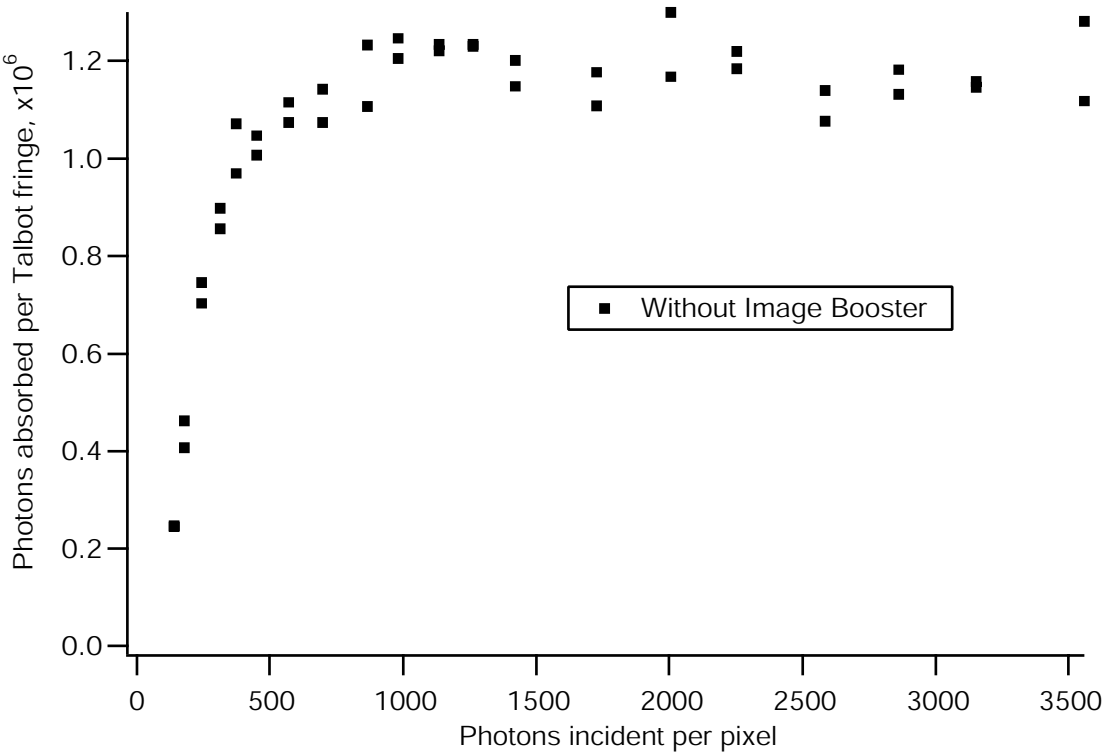

Figure 2.7: Number of photons absorbed per Talbot fringe.

1000 photons per pixel, corresponding to an incident energy of 1.4×10^{-8} J/cm^2. At typical imaging laser intensities, this power density corresponds to an exposure time of 70 microseconds. Images taken with this exposure time are in the saturated regime and the 2 photon/atom calibration applies.

Figure 2.8 displays the same curve in the presence of the image booster beam. We can see that the saturation of the absorption signal is suppressed and many more photons can be scattered per atom.

Figure 2.9 shows an absorption image of our HAT in the absence of the image booster beam. The x and y axes are in units of camera pixels, and the z axis is the number of photons absorbed per square pixel. This image was taken with 4x4 binning, so each pixel is a square 5.38 μm on a side.

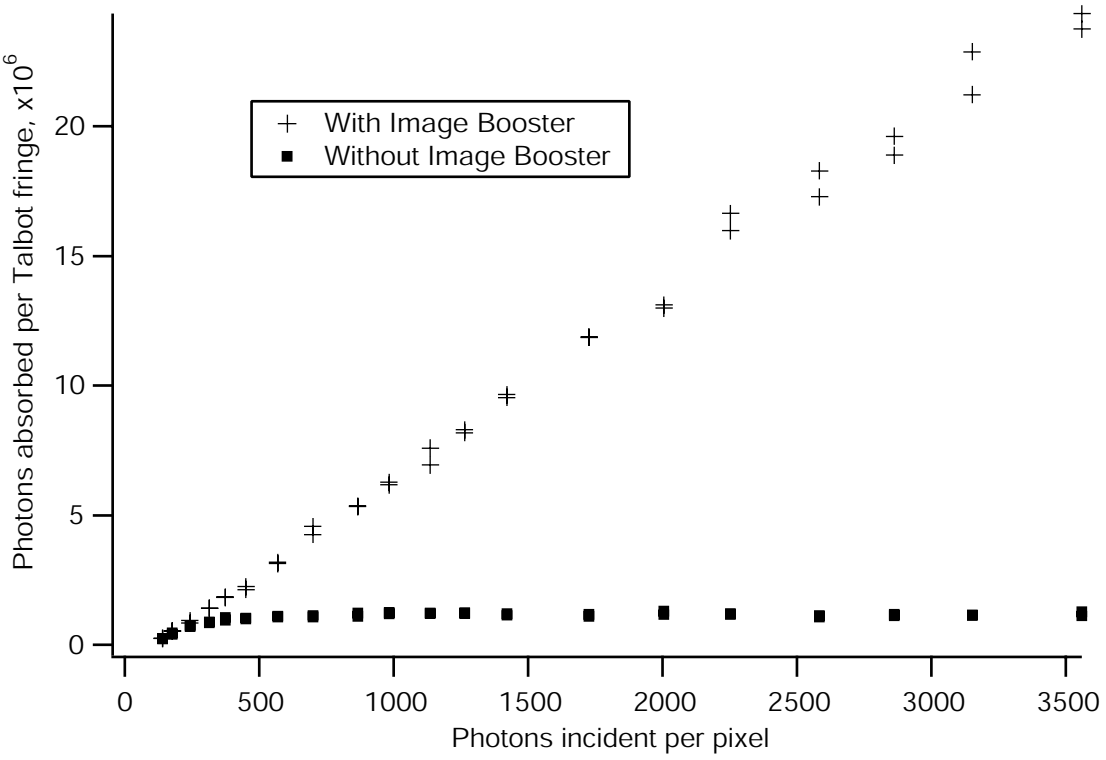

Figure 2.8: Number of photons absorbed per Talbot fringe with image booster beam.

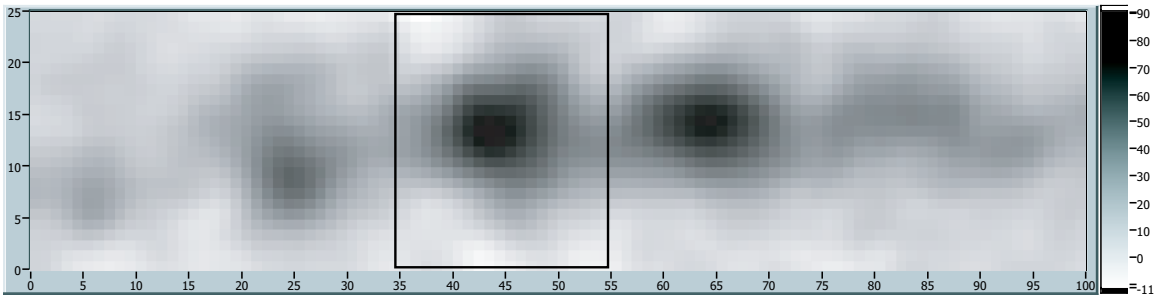

Figure 2.9: Absorption image of HAT without image booster beam.

We calculate the number of atoms in a Talbot fringe by summing up all the photons absorbed in a Region Of Interest (ROI) containing the fringe and dividing by two photons/atom. For the image shown, the ROI indicated by the black rectangle contains 3.44×10^5 photons, or 1.72×10^5 atoms. Comparing the size of the maximum absorption signal to the fluctuations in the background, we find a signal to noise ratio of 22.

Figure 2.10 shows an absorption image of a sample prepared identically to that in Figure 2.9, but imaged in the presence of the image booster beam. Note that the scale on the z-axis is approximately 14 times larger, indicating the vast enhancement of signal created by the booster beam. Again we choose a region of interest containing one Talbot fringe and find the total number of photons absorbed, in this case 2.07×10^6. Given that the atom clouds were generated under the same conditions, we may assume that the number of atoms is the same as in the no-image-booster case and find the enhancement factor η. For this pair of pictures, we find $\eta = 12.8$, and the signal to noise ratio is 120.

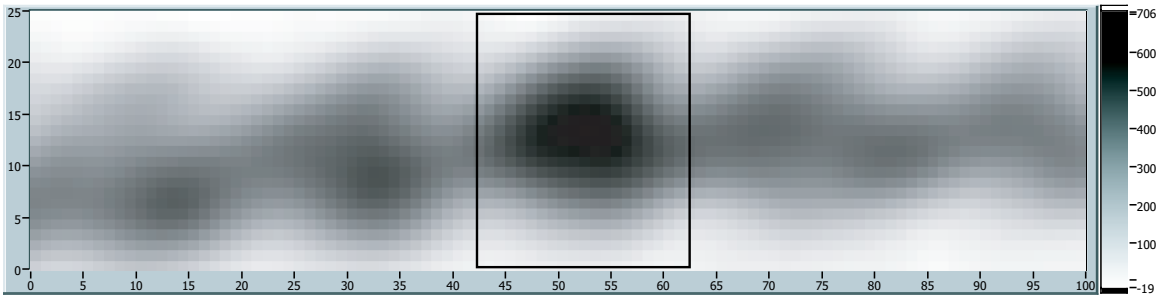

Figure 2.10: Absorption image of HAT with image booster beam. Note z-axis scale different from Fig. 2.9.

Chapter 3

Magneto-Optical Trap

3.1 Background

Since its first demonstration in 1985 [Chu *et al.*, 1985], the Magneto-Optical Trap (MOT) has become a cornerstone of atomic physics research. The ability to collect hundreds of millions of atoms in a cloud cooled to microKelvin temperatures has been exploited in a vast array of experiments. The theoretical and experimental basis for the MOT has been reviewed in several publications and will not be presented here. The interested reader is referred to the article by Foot [Foot, 1991] and the book by Metcalf and van der Straten [Metcalf and van der Straten, 1999].

While not a central focus of this dissertation, the MOT apparatus is central to the following chapters and is thus presented separately. This chapter begins with a description of our Titanium:sapphire and diode lasers, the magnetic field coils, and optical pumping setup used to generate our MOT in Section 3.2. We proceed in Section 3.3 to describe our methods to characterize the MOT, and present typical results: 10^7 atoms loaded into the MOT at $\simeq 6\mu K$ temperature.

3.2 Apparatus

3.2.1 Trapping laser

The light used to pump the main trapping transition $^2S_{1/2}$ $F = 2$ to $^2P_{3/2}$ $F' = 3$ comes from our custom-built Titanium:Sapphire laser (see Figures 3.1 and 3.2). An 8 Watt Argon-Ion laser (Coherent Innova 310) pumps the Ti:Sapph. The laser cavity is a ring oscillator in a bow-tie arrangement, a birefringent filter provides coarse wavelength tuning, while an intracavity etalon and piezoelectric-controlled mirror provide fine adjustment of the lasing frequency. This laser is described in greater detail in [Williamson, 1997]. The laser typically provides 700 mW of power at 780 nm.

A portion of the beam is split off and used in our spectroscopy system. It is passed through an electro-optic modulator running at 14.7 MHz which produces sidebands on the output beam. The beam passes through a rubidium vapor cell and is retroreflected, then directed onto a fast photodiode. Only those atoms with the same velocity relative to both incident and reflected beams will have no relative Doppler shift and absorb photons from both beams; thus the absorption signal seen by the photodiode is not Doppler broadened. The signal from a second beam which passes through the cell but which is not retroreflected is subtracted from the first photodiode, to remove the wide Doppler broadened background. The signal from the photodiodes is beat against the the ± 14.7 MHz oscillator signal so that the two sidebands generate a differential signal consisting of dispersion-like S-curves centered on each of the absorption features. The laser is locked to the crossover between the $^2P_{3/2}$ $F' = 1$ and $F' = 3$ levels, and is thus 212.2 MHz below resonance with the $F' = 3$ level (see Figure 3.1).

The frequency and intensity of the laser are further controlled by an acousto-optic modulator (AOM) in a double-pass configuration. See Figure 3.3. The beam is sent through the AOM and a +1 order diffracted beam is retroreflected back into the crystal.

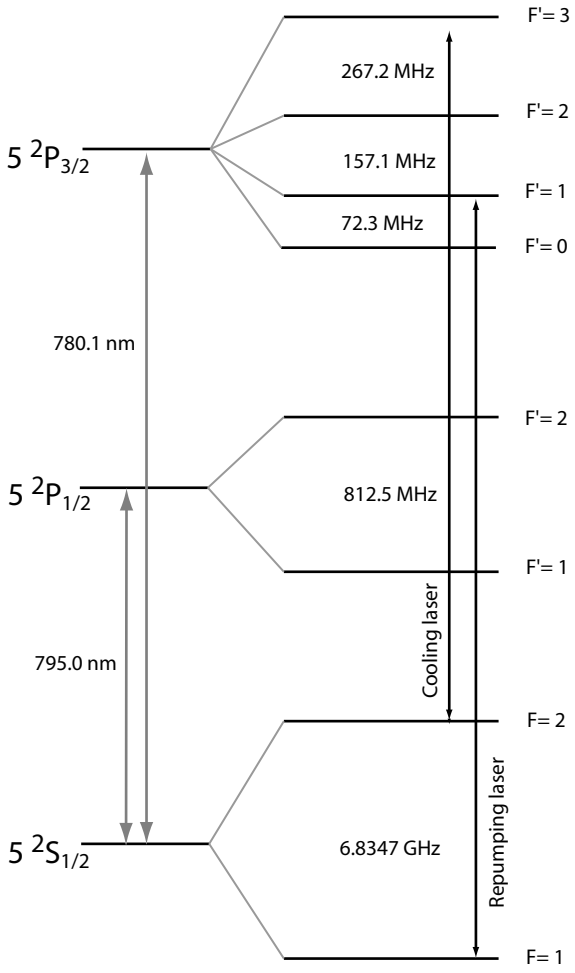

Figure 3.1: Energy level diagram of ^{87}Rb.

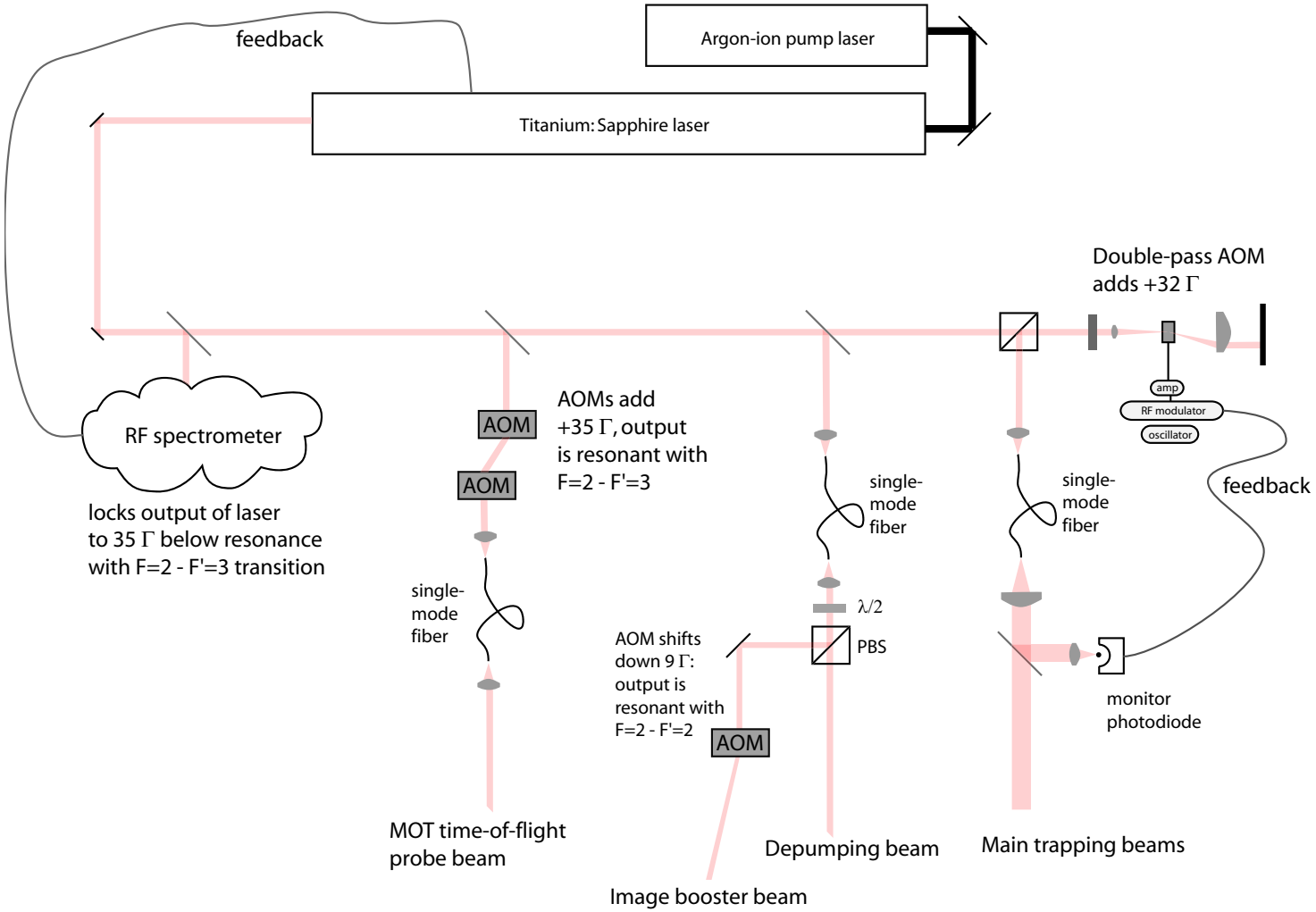

Figure 3.2: Diagram of Ti:Sapph laser and output beams.

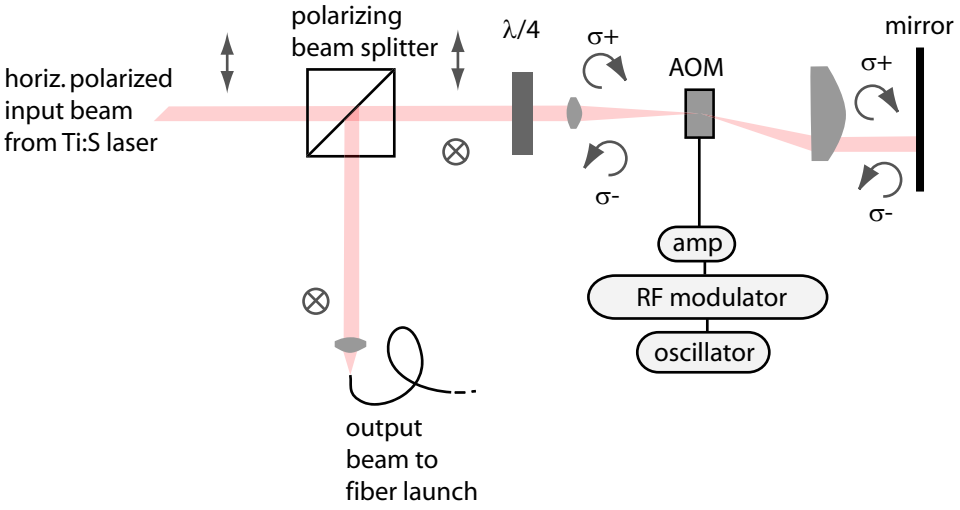

Figure 3.3: Diagram of double-pass AOM.

Having been diffracted twice, the returning beam is shifted by twice the drive frequency of the AOM. The incident beam is σ^+-polarized so the returning beam is σ^- and the two can be separated with a $\lambda/4$ waveplate and polarizing beam splitter. We have found so significant polarization sensitivity in the AOM used, as is required for this configuration to work well. For steady-state loading of the MOT, the AOM is driven at 97 MHz, for a total shift of +194 MHz. The laser is 18 MHz, or three natural linewidths (3 Γ) detuned from the trapping transition.

This double-pass arrangement has the advantage that the angle of the output beam does not depend on the frequency of the AOM. We are able to shift the laser frequency by over 40 MHz and still remain coupled into a single-mode fiber over one meter away. We are also able to control the intensity of the output beam by attenuating the radio-frequency drive signal to the AOM. An analog variable attenuator inserted between the voltage-controlled oscillator and RF amplifier allows over 55 dB of intensity modulation.

Following the AOM, the light is coupled into a single-mode polarization maintaining

fiber to carry it to the optical table with the MOT apparatus. As with all polarization maintaining fibers, it is necessary to align the polarization of input beam with the slow axis of the fiber. The output of the fiber is collimated with an $f = 100$ mm lens to create a beam with an intensity of 35 mW/cm^2. This is divided into three beams which are directed along the three orthogonal axes of the MOT and retroreflected, with the appropriate polarization optics.

A portion of the light is picked off by an uncoated glass slide and focused onto a photodiode. This signal is input into a "noise-eater" circuit which adjusts the RF power to the double-passed AOM until the photodiode signal equals an input reference voltage. This serves two purposes: it stabilizes the intensity seen by the atoms, and it allows rapid, repeatable changes in intensity through control of the reference voltage.

3.2.2 Repumping laser

The $^2S_{1/2}$ $F = 1$ to $^2P_{3/2}$ $F' = 2$ repumper light comes from a home-made external cavity diode laser in the Littrow configuration [Arnold *et al.*, 1998]. The diode is an Hitachi HL785 50 mW diode which free-runs at 783 nm. Its temperature is stabilized with a Peltier cooler and PID feedback circuit which monitors a thermistor mounted in the diode holder. The output diffracts off an 1800 lines/inch holographically produced grating; the first diffracted order is fed back into the laser diode. The zeroth-order reflected beam, containing 21 mW exits the cavity and passes through a half-wave plate and anamorphic prism pair before entering an optical isolator.

A fraction of the beam is picked off by an uncoated glass slide and sent to a saturated absorption spectrometer, which generates a Doppler-free spectrum of the $^2S_{1/2}$ $F = 1$ to $^2P_{3/2}$ $F' = 0, 1, 2$ manifold in ^{87}Rb. A lock-in amplifier modulates the laser current at 20 kHz and produces a derivative of the spectrum signal. The laser is locked to the

crossover peak between $^2P_{3/2}$ $F' = 1$ and $F' = 2$ which is 78.6 MHz below resonance with the transition to $F' = 2$. After passing through a second optical isolator, the beam is shifted 75 MHz higher in frequency by an acousto-optic modulator (AOM), so that it is 0.5 Γ to the red of resonance with the $F = 1$ to $F' = 2$ transition. By interrupting the RF drive power to the AOM, we are able to extinguish the repumping light in less than a microsecond. Following the AOM, the light is launched into a single mode fiber and carried to the trapping table.

A beam of repumping light containing 2.5 milliwatts exits the fiber and is collimated to a 6 mm waist. It passes through an optical flat with an 3.5 mm diameter circular obstruction (a slice of a Viton O-ring) glued to it. The shadow of this obstruction creates the dark SPOT in the center of our MOT, forcing approximately 50% of the atoms into the $^2S_{1/2}$ $F = 1$ ground state. This is done to decrease the fraction time atoms in the center of the trap spend in the $^2S_{1/2}$ $F = 2$ state. Atoms in the $F = 2$ state scatter photons from the cooling laser and these scattered photons can be rescattered by other atoms in the trap, and this "radiation pressure" limits the peak density attainable [Ketterle *et al.*, 1993, Anderson *et al.*, 1993].

The repumper light is split by a non-polarizing beam splitter into one beam which travels through the vacuum chamber horizontally and a second which travels vertically from top to bottom. Neither beam is retroreflected. A single $f = 400$ mm biconvex lens images the dark spot onto the center of the MOT with 1:1 magnification. We align each of the repumping beams separately to ensure that the dark spots overlap in the center of the trapping volume. This is done by blocking one beam and steering the other until the shadow of the dark spot is seen in a fluorescence image of the MOT.

The fraction of atoms in the $^2S_{1/2}$ $F = 1$ ground state is further increased with the addition of a depumping laser tuned to near-resonance with the $^2S_{1/2}$ $F = 2$ to $^2P_{3/2}$ $F' = 2$ transition (see Figure 3.2). Atoms which are pumped out of the $F = 2$ to

$F' = 3$ cycling transition and into the $F' = 2$ level have a 50% chance of falling into the $F = 1$ dark state. This laser is taken directly from the Ti:sapphire laser and is 9Γ to the red of resonance with the depumping transition. Like the trapping laser, it is carried from the Ti:sapph table to the trapping table by a single mode fiber, which reduces the effects of relative movement of the tables. After the fiber the beam is collimated to a $1/e^2$ radius of 1.2 mm. The laser is mixed in with the repumper beam at its center, so that the depumper is collinear with the dark spot. We use a set of neutral density filters to adjust the intensity of the depumping beam, a power of 300 μW is typical.

3.2.3 Vacuum chamber

Our experiments are conducted inside an ultra-high vacuum chamber held at a pressure $\sim 10^{-9}$ torr. This chamber is stainless-steel construction with eight 2.75-inch glass windows around its circumference, and two 2.75-inch windows on the top and bottom. The distance from the center of the chamber to the nearest circumferential window is approximately 10 cm, and to the top and bottom windows approximately 8 cm. The chamber is evacuated by means of a Varian 8 liter/sec ion pump which runs continuously at approximately 0.1 μA. One gram of Rubidium metal is held in a smaller appendage chamber which is connected to the main chamber. To load more rubidium into the system we heat the appendage chamber to $\sim 50°$C.

3.2.4 Magnetic fields

The anti-Helmholtz magnetic field used to create the MOT is made by a pair of opposing wire coils. Each coil contains 90 turns of 14 awg magnet wire, has an average radius of 4.25 cm and is 4.6 cm above or below the center of the vacuum chamber. We desire a magnetic field gradient of 20 Gauss/cm at the trap, which corresponds to a

field of 92 Gauss at the center of each coil. Since the field given by a loop of wire is $B = \mu_0 NI/2R$, we typically run a current of 6.9 Amperes. During the loading of the HAT, we often increase the current to 14 A to double the field gradient and compress the MOT, forcing more atoms into the HAT loading region.

To prevent overheating and possible damage to the wire, we inserted a thermistor inside the windings of the top coil. It is in close thermal contact with the magnet wire and is thus able to monitor its temperature. Under normal operating conditions the thermistor reads approximately 30 $k\Omega$, which corresponds to 35 C. An electronic circuit is connected to the thermistor which will sound an alarm and shut off the current supply if the resistance falls below 10 $k\Omega$, or 70 C.

Three pairs of Helmholtz coils are wound around the chamber along three orthogonal axes to shim the magnetic field. Each coil contains approximately 20 turns of wire and is roughly 2 cm in radius. The currents through these coils are adjusted daily to compensate for external magnetic fields which would tend to pull the MOT away from the center of the trapping beams. Typical currents are below 2 A, corresponding to fields below 5 Gauss.

3.2.5 Optical pumping

As described in Section 4.2, to increase the phase space density of atoms in the HAT we wish to optically pump them into a single magnetic sublevel of the $F = 1$ ground state. This spin-polarization is achieved with a single beam of circularly polarized light resonant with the $^2S_{1/2}$ $F = 1$ to $^2P_{3/2}$ $F' = 1$ transition. The ground state magnetic sublevels are split by a pair of Helmholtz magnetic field coils aligned with the propagation direction of the optical pumping light. The coils are 3 cm in radius and 8.5 cm from the atom cloud. They contain 4 turns of wire carrying 12 Amperes,

and thus generate a reasonably uniform 1 Gauss field at the center of the trap. This field creates an ± 1.4 MHz energy shift in the $m_F = \pm 1$ sublevels. The magnetic field axis and propagation of the spin-polarizing beam are collinear with the imaging laser direction, so that the imaging laser can be used to probe the polarization.

For optical pumping to be effective the atoms must make several $F = 1$ to $F' = 1$ transitions. The probability of making a transition from $F' = 1$ to the undesired $F = 2$ state is 1/5 the probability of returning to $F = 1$. Thus, after scattering an average of six photons, the atoms are pumped into the unpolarized $F = 2$ ground state. To prevent this from happening, we perform optical pumping in the presence of our ${}^2S_{1/2}$ $F = 2$ to ${}^2P_{3/2}$ $F' = 2$ depumping laser. This excites any atoms in the undesired $F = 2$ ground state to $F' = 2$, from which it has equal probabilities to decay back to $F = 2$, or to $F = 1$. We wish to suppress any optical pumping by the depumper, in particular to the dark $F = 2, m_F = \pm 2$ states. This is done by circularly polarizing the downward-travelling beam, and linearly polarizing the beam which travels askew to the magnetic field axis. The polarization of the depumper field is thus a hodge-podge of directions varying rapidly throughout space.

3.3 Results

3.3.1 Number of atoms

We measure the number of atoms trapped in the MOT by collecting light scattered from the trapping beams, calculating the scattering rate for a single atom, and deducing the total number. Scattered light is gathered with a single $f = 125$ mm planoconvex lens and focused onto a silicon photodiode. We measure the output of a current-to-voltage converter which monitors the photocurrent. The total power radiated by the MOT is

thus

$$P_{rad} = \frac{V}{g_{I-V}} \times \frac{1}{\eta_{diode}} \times \frac{1}{\eta_{optical}} \tag{3.1}$$

where g_{I-V} is the gain of the current-to-voltage converter (10^8 V/A), the photodiode conversion efficiency (0.48 A/W) is η_{diode} and the optical collection efficiency is $\eta_{optical}$. This last term includes contributions from the solid angle subtended by the lens and the transmission efficiencies of two interference filters and a beam splitter.

The number of atoms is easily deduced from the radiated power by taking into account the energy released in one emission $E_\gamma = 2.55 \times 10^{-19}$ J, the excited-state lifetime τ and the excited-state fraction f_e.

$$N = P_{rad} \times \frac{\tau}{E_\gamma f_e} \tag{3.2}$$

In our steady-state MOT with $I = 72$ mW/cm^2 total power at the center and $\Delta = 3\,\Gamma$ we measure between 1 and 2 Volts of fluorescence, which corresponds to a number of atoms between 5×10^6 and 10^7. We have found that it is necessary to increase the background vapor pressure in our chamber by heating the attached Rubidium ampoule every day. We believe the pressure in the chamber stays around 2×10^{-9} torr, but overnight the partial pressure of Rubidium will fall and only 1 or 2 $\times 10^6$ atoms will be collected by the MOT. After 30 minutes of heating the Rb ampoule, the number of atoms in the MOT will have increased by two or three times.

3.3.2 Temperature measurements

We have measured the temperature of atoms in our magneto-optical trap using a free-fall time-of-flight technique. We proceed through the usual preparation of a highly-detuned MOT and simultaneously turn off the magnetic field and the MOT lasers. As it falls, the cloud of atoms expands ballistically at a rate related to its temperature. We use a narrow probe beam resonant with the trapping transition and located just

below the MOT to induce florescence in the falling atoms. A lens images the resulting pulse of light onto a photodiode, and we record the width of the pulse. Subsequent analysis yields the MOT temperature, as described below.

The probe beam is derived from the Ti:sapphire laser and shifted by two acousto-optics modulators tuned to 96 MHz each. The beam is thus 192 MHz above the crossover frequency, or 20 MHz (3.3 Γ) to the red of resonance with the trapping transition. We launch the light into a single mode fiber and collimate the output with a waist approximately 500 microns. This beam passes through the vacuum chamber horizontally several millimeters below the MOT and is retroreflected back to the fiber. Alignment of the beam is easily done by steering it until it hits the MOT, which produces an obvious dark hole in its center. It is then straightforward to steer the beam down the required distance.

A mirror mounted to a magnetic removable base is placed by the window normally used for the entrance of the HAT beams. It redirects the fluorescence from the probe beam through an $f = 100$ mm lens and onto a silicon photodiode. We use an interference filter centered at 780 nm with a 5 nm passband to remove signal from other sources. We align the photodiode by finding the position which maximizes the florescence signal from a steady-state MOT, then tilt the down slightly so that the area directly below the MOT is imaged on the photodiode.

Our typical timing sequence is similar to the standard HAT loading scheme. We start with a steady state MOT with trapping beams with total intensity around 5 mW/cm^3 and detuning of 3 Γ. We reduce the intensity by factor of three and shift the detuning to 9 Γ, wait 20 ms, and extinguish the MOT beams and magnetic field. We see a pulse of fluorescence from the cloud falling through the probe beam 45 milliseconds later. The rempumping laser is kept on throughout this process to increase the number of photons scattered by the atoms when they fall into the probe

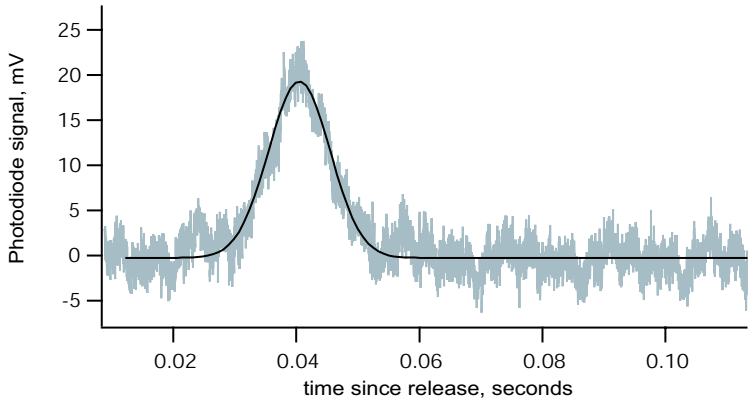

Figure 3.4: Time of Flight signal for MOT temperature measurements. Waist of gaussian fit is 7.1 ms

beam.

The photocurrent is amplified with a 10^8 Ohm I-V converter and recorded on a scope. We find that it is typically necessary to average 4 or more measurements to achieve satisfactory signal to noise ratios. A sample trace is shown in 3.4. Fitting the fluorescence pulse to a gaussian peak we measure the half-width at the $1/e$ point to be 7.1 ± 0.05 ms.

The probability for an atom of mass m in a thermal cloud at temperature T to have velocity v is given by

$$P(v) = \frac{e^{-\frac{v^2}{v_T^2}}}{\sqrt{\pi} v_T} \tag{3.3}$$

where v_T is the mean thermal velocity

$$v_T = \sqrt{2k_B T/m} \tag{3.4}$$

Since an atom which has initial velocity v will fall a distance d in time t given by $d(t) = \frac{1}{2}gt_0^2 - vt_0$ we can solve for the velocity as a function of time.

$$v = \frac{\frac{1}{2}gt_0^2 - d}{t_0}$$

$$= \frac{\frac{1}{2}gt(t+2\sqrt{2d/g})}{(t+\sqrt{2d/g})} \tag{3.5}$$

where we have made the substitution $t = t_0 - \sqrt{2d/g}$. Inserting this into our function for $P(v)$ gives

$$P(t) = \frac{e^{-\frac{g^2t^2}{4v_T^2}}}{\sqrt{\pi}v_T\left(t+\sqrt{2d/g}\right)} \tag{3.6}$$

which, for values of v_T small compared to gt is essentially a gaussian peak with $1/e^2$ width of

$$\sigma_t = \frac{4v_T}{g} \tag{3.7}$$

We thus conclude that our observed 7.1 ms pulse corresponds to a MOT temperature of 6.1 μK. A more rigorous mathematical treatment is given by Yavin *et al.* [Yavin *et al.*, 2002] and reduces to equation (3.6) in the limit of a cold and small cloud. Our measured temperatures are in good agreement with the predictions of Gerz *et al.* [Gerz *et al.*, 1993];

$$T = \frac{\hbar\Gamma}{k_B}\left(c_\perp \frac{I}{I_{sat}}\frac{\Gamma}{\Delta}\right) + const. \tag{3.8}$$

where Γ is the natural linewidth of the trapping transition ($5.89 \times 2\pi$ MHz), Δ is the detuning of the MOT beams, I_{sat} is the saturation intensity 3.2 mW/cm^2 and $c_\perp$ and *const.* are scale factors experimentally determined to be 0.40 and 5 μK.

3.3.3 Spin polarization

We measure spin polarization by detecting circular dichroism in the atom cloud. After milliseconds of optical pumping with the $F = 1$ to $F' = 1$ and $F = 2$ to $F' = 2$ beams, we take absorption images with σ^+ and σ^- circularly polarized imaging beams which are collinear with the optical pumping axis. We have observed a factor of 2.8 difference

in the absorption of these two cases, indicating that a substantial fraction of the atoms have been optically pumped into the $F = 1, m_F = \pm 1$ magnetic sublevel.

Chapter 4

The Holographic Atom Trap

4.1 Introduction

This chapter presents the theoretical background and experimental apparatus used to develop the Holographic Atom Trap. A summary of our typical results is also given. Section 4.2 describes the physical mechanism by which an array of potential wells is created by the interference of five laser beams. Similar experiments in the field are discussed and related to ours in Section 4.3. The majority of the chapter, Section 4.4 is devoted to the apparatus employed in creating the HAT; our far off resonant Nd:YAG laser and the associated optics and control electronics. Section 4.5 describes the optimized loading procedure used to transfer atoms from the initial MOT into the HAT. The chapter concludes in Section 4.6 with a discussion of our typical results: $\simeq$ 16,000 atoms per lattice site at 50 microkelvin, with a trap lifetime of $\simeq$ 800 milliseconds and peak densities near 5×10^{-14} cm^{-3}.

4.2 Theory

4.2.1 Dipole force

In this section we discuss the dipole force on an atom in a highly-detuned electric field. Consider the case of a two-level atom with states $|e\rangle$ and $|g\rangle$; at any time t its wavefunction can be written as a superposition of the two $|\Psi\rangle = C_g(t)|g\rangle + C_e(t)|e\rangle$. The Schrödinger equation describes the time-evolution of the coefficients C_g and C_e

$$i\hbar\frac{d}{dt}C_g = C_e H_{ge} e^{-i\omega_0 t} \tag{4.1}$$

$$i\hbar\frac{d}{dt}C_e = C_g H_{eg} e^{-i\omega_0 t} \tag{4.2}$$

where ω_0 corresponds to the energy spacing between the states, and H_{eg} and H_{ge} are the matrix elements of the Hamiltonian connecting the ground and excited states. If the atom is now exposed to a plane-wave electric field oscillating at ω_{laser}, we transform the coefficients according to

$$C'_g = C_g \quad C'_e = C_e e^{-i\Delta t} \tag{4.3}$$

and make the rotating wave approximation:

$$i\hbar\frac{d}{dt}C'_g = C'_e\frac{\hbar\Omega}{2} \tag{4.4}$$

$$i\hbar\frac{d}{dt}C'_e = C'_g\frac{\hbar\Omega}{2} - C'_e\hbar\Delta \tag{4.5}$$

which is expressed in terms of the Rabi frequency Ω which is defined

$$\Omega = \frac{-e\ E}{\hbar}\langle e|r|g\rangle \tag{4.6}$$

where E is the electric field of the driving laser. We can thus rewrite the Hamiltonian in terms of the new coefficients

$$H' = \frac{\hbar}{2}\begin{bmatrix} -2\Delta & \Omega \\ \Omega & 0 \end{bmatrix} \tag{4.7}$$

The eigenvalues of this new Hamiltonian correspond to shifts in the two energy levels caused by the laser, the a.c. Stark shifts.

$$\Delta E_g = \frac{\hbar\Omega^2}{4\Delta} \tag{4.8}$$

$$\Delta E_e = -\frac{\hbar\Omega^2}{4\Delta} \tag{4.9}$$

Since $\Omega^2 \propto E^2$, the shift is proportional to the laser intensity and is called the light shift or the AC Stark shift. We finally conclude that the presence of the far-off resonant laser field depresses the ground state energy by an amount proportional to the laser intensity. A spatially varying laser field creates a spatially varying potential $U(\mathbf{r})$. It is most convenient to express the constant of proportionality in terms of α, the atomic polarizability.

$$U(\mathbf{r}) = -\alpha|E|^2 = -\frac{2\pi\alpha}{c} I(\mathbf{r}) \tag{4.10}$$

The polarizability α is in general a tensor quantity whose components depend on the details of the atom in question and the wavelength of off-resonant light. The derivation presented is a simplification; in particular the rotating wave approximation is invalid when the laser is detuned by a sizable fraction of the energy level spacing, as in our case. Nonetheless, this discussion is qualitatively correct, and breaks down only in the quantitative prediction of α. A more detailed analysis of the situation is discussed by Gordon and Ashkin [Gordon *et. al*, 1980], and Dalibard and Cohen-Tannoudji [Dalibard *et al.*, 1985].

Our experiments involve trapping rubidium-87 atoms in a potential well created by a far-off resonant Nd:YAG laser operating at $\lambda = 1064\,nm$. The polarizability of rubidium at this wavelength has been accurately measured by Kadar-Kallen and Bonin [Kadar-Kallen and Bonin, 1992] to be 105 $\mathring{A}$.

4.2.2 Far-off resonant trap

It is possible to employ the dipole force to create a potential well in which to confine atoms [Ashkin, 1970]. The simplest possible far-off resonant trap (FORT) is made by bringing an intense Gaussian beam to a small focus. If the focused waist is w_0, the intensity varies as

$$I(r) = I_0 e^{-r^2/w_0^2} \tag{4.11}$$

in the transverse directions. This creates a confining force on the atoms

$$F = -\nabla U(\mathbf{r}) = \frac{2\pi\alpha}{c}\nabla I(\mathbf{r}) = -\frac{\pi\alpha\ r\ I_0}{c\ w^2} e^{-r^2/w_0^2} \tag{4.12}$$

Similarly, there is attractive force in the longitudinal direction which depends on the focusing properties of the laser beam. Thus the atoms are confined in a three-dimensional trap with a maximum trap depth $U_0 = -2\pi\alpha I_0/c$.

Atoms are drawn to the regions of highest laser power, increasing the probability of scattering photons from the trapping beam. This scattering leads to heating and ejection from the trap as atoms recoil. An advantage to the FORT is that this problem can be easily overcome by noting that the confining dipole force decreases as $1/\Delta$, but the scattering rate decreases as $1/\Delta^2$. Thus an intense laser beam far from resonance can produce the same trapping force as a less-intense beam closer to resonance, but will enjoy a much lower scattering rate.

The first demonstration of such a trap was performed by Chu *et al.* in 1986 [Chu *et al.*, 1986]. Sodium atoms were confined in a 200 mW beam detuned 650 GHz below resonance and focused to a 10 μm waist. At this detuning the light scattering rate was still appreciable. Miller *et al.* demonstrated the first truly far-off resonant trap in 1993 with light tuned several nanometers from resonance with the 795 nm transition in rubidium atoms [Miller *et al.*, 1993]. At this detuning the scattering rate was a few hundred photons per second, and the trap lifetime was several hundred milliseconds.

4.2.3 Density and phase space density

We can draw an analogy between atoms held in the FORT and the canonical mass-on-a-spring harmonic oscillator. We use the equation $\mathbf{F} = \kappa \cdot \mathbf{r}$ to define a spring constant tensor κ. As in the case of a mass on a spring, the oscillation frequency of atoms of mass M caught in the trap is given by $\nu = \frac{1}{2\pi}\sqrt{\frac{\kappa}{M}}$. The peak density of atoms in the FORT is

$$n_0 = N\left(\frac{\kappa}{2\pi k_B T}\right)^{3/2} \tag{4.13}$$

where N is the number of atoms, T is their temperature and k_B is Boltzmann's constant. As the trap is likely to have different dimensions in the x, y, and z directions, it is convenient to express this in terms of the oscillation frequencies along three axes:

$$n_0 = N\left(\frac{2\pi M c^2}{k_B T}\right)^{3/2}\left(\frac{\nu_x \nu_y \nu_z}{c^3}\right) \tag{4.14}$$

Similarly, the phase space density, or number of atoms per energy level in the trap, is

$$\rho = N\frac{h\nu_x}{k_B T}\frac{h\nu_y}{k_B T}\frac{h\nu_z}{k_B T} \tag{4.15}$$

It is important to note that both these quantities increase with increasing trap oscillation frequencies, not with the maximum trap depth. Consequently, for a given temperature, number of atoms, and trap depth, we can increase phase space density by using a trap which is spatially smaller (higher κ) and thus has higher oscillation frequencies. This is primary motivation for our Holographic Atom Trap (HAT); by trapping atoms in the antinodes of a standing wave interference pattern, we achieve much tighter confinement of the atoms and thus much higher phase space densities. The disadvantage to confining atoms in an interference pattern is the difficulty associated with loading a large number of atoms into the lattice cells; the improvement in phase space density arising from tight confinement must not be outweighed by a loss in atom number.

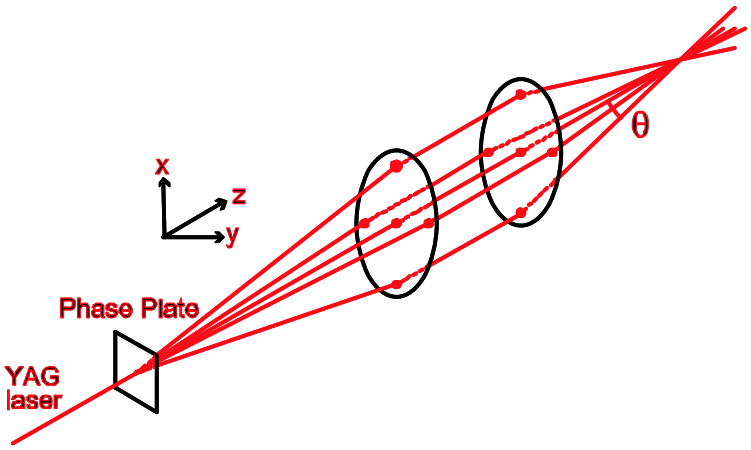

Figure 4.1: The Holographic Atom Trap.

4.2.4 Intensity pattern of the HAT

Our Holographic Atom Trap (HAT) is formed by the intersection of five far-off-resonant laser beams as shown in Figure 4.1. A single beam from our YAG laser ($\lambda = 1064$ nm) propagating in the z-direction is diffracted into five beams as it passes through a holographically-produced phase plate. The five beams are superposed via two transfer lenses so that they cross each other as they pass through a cloud of laser cooled atoms generated by our MOT.

The electric field pattern at the intersection of the five beams is given by

$$E = E_0 \left[1 + 2\beta e^{-ikz\theta^2/2} \left(\cos k\theta x + e^{i\delta} \cos k\theta y\right)\right] \tag{4.16}$$

where β is the ratio of the electric field magnitudes of the center beam and one of four outer beams, $k = \frac{2\pi}{\lambda}$ is the wavevector of the laser, and θ is the angle between the center and the outer beams. The relative phase between the zeroth-order beam and the first-order beams, δ, depends on the details of the phase grating and the optical path length difference between the beams. In the case with $\delta = 0$ all the fields add up in phase at the center and the intensity is maximized. For this case, the intensity is

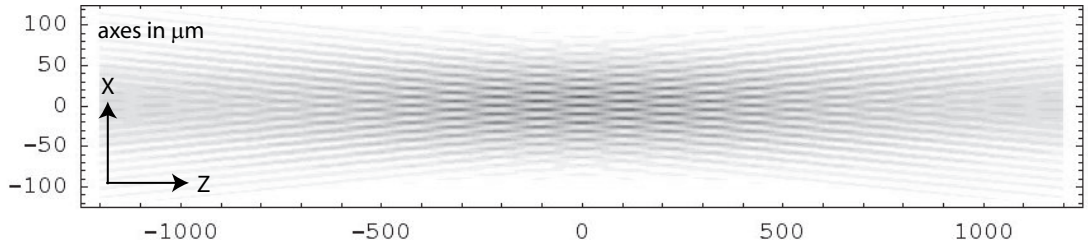

Figure 4.2: Intensity pattern at the HAT.

given by

$$I(x,y,z) = I_0[1 + 4\beta^2(coskx\theta + cosky\theta)^2 + 4\beta cos\frac{kz\theta^2}{2}(coskx\theta + cosky\theta)] \quad (4.17)$$

where I_0 is the intensity of the center beam. At the center of the interference pattern $x = y = z = 0$ and we find $I_{max} = I_0\,(1 + 8\beta + 16\beta^2)$ and we see that the coherent addition of the five beams leads to a substantial enhancement of the peak intensity.

Figure 4.2 shows a calculation of this intensity pattern in the x-z plane. This calculation uses our measured values of $\beta = 0.46$ and $\theta = 100$ mrad. The ratio of the beam intensities, β^2 is determined by measuring the power in the center beam and each of the four outside beams with an optical power meter. Note that the x axis of Figure 4.2 has been stretched relative to the z-axis to display the transverse interference pattern. We refer to a lattice site as a microtrap; each one measures $10\mu m \times 10\mu m \times 100\mu m$. The fringes along the z-direction arise from the Talbot effect [Boiron *et al.*, 1998], and as such we refer to them as Talbot fringes.

4.2.5 HAT parameters

Given the intensity pattern (Equation 4.17) and the result from Equation 4.10 that $U(\mathbf{r}) = -\frac{2\pi\alpha}{c}I(\mathbf{r})$ we can calculate the effective spring constant tensor κ for the HAT. Since $\mathbf{F} = -\nabla U = \kappa \cdot \mathbf{r}$, the components of κ correspond to the spatial derivatives of

$I(\mathbf{r})$.

$$\kappa_{xx} = U_0 \frac{16\,\pi^2\,\beta\,\theta^2\,(1+4\beta)}{\lambda} = U_{max} \frac{16\,\pi^2\,\beta\,\theta^2\,(1+4\beta)}{\lambda^2\,(1+8\beta+16\beta^2)} \tag{4.18}$$

$$\kappa_{yy} = \kappa_{xx} \tag{4.19}$$

$$\kappa_{zz} = U_{max} \frac{8\,\pi^2\,\beta\,\theta^4}{\lambda^2\,(1+8\beta+16\beta^2)} \tag{4.20}$$

From these it is straightforward to find the oscillation frequencies along three directions.

$$\nu_x = \frac{2\,\theta}{\lambda}\left[\frac{\beta\,(1+4\beta)\,U_{max}}{(1+8\beta+16\beta^2)\,M}\right]^{1/2} \tag{4.21}$$

$$\nu_y = \nu_x \tag{4.22}$$

$$\nu_z = \frac{\theta^2}{\lambda}\left[\frac{2\,\beta\,U_{max}}{(1+8\beta+16\beta^2)\,M}\right]^{1/2} \tag{4.23}$$

For our values of θ, β, λ, and M, we can write these equations in the convenient form

$$\nu_x = \nu_y = 9.1\ kHz\sqrt{\frac{U_{max}}{150\ \mu K}} \tag{4.24}$$

$$\nu_z = 0.38\ kHz\sqrt{\frac{U_{max}}{150\ \mu K}} \tag{4.25}$$

Our typical YAG power at the HAT is 4.6 Watts in the center beam, focused down to an 85 μm by 75 μm waist. This corresponds to a maximum intensity of 3.7 $\times 10^5$ Watts/cm^2, for a maximum trap depth of 620 microkelvin. For these parameters, we find the transverse oscillation frequencies $\nu_x = \nu_y = 18.5$ kHz and the longitudinal frequency $\nu_z = 780$ Hz. The geometric mean oscillation frequency is therefore 6.4 kHz.

4.3 Other lattice FORTs

A number of experiments have been described which seek to combine high oscillation frequencies with lattice cells large enough to load many atoms into each site.

Among the first was the creation of a hexagonal array of lattice sites for Cesium by Boiron *et al.* [Boiron *et al.*, 1998]. By illuminating a hexagonal grating with light from a YAG laser, this group created an array of potential wells with 10^4 atoms in each 3.5 $\mu m \times 3.5$ $\mu m \times 20$ μm site. By applying blue Sisyphus cooling they reached a temperature of 10 μK. The high oscillation frequency in the two radial directions (5 kHz) leads to densities greater than 10^{13} atoms/cm^{-3} and a phase space density greater than 10^{-3}. A single retro-reflected beam provides one of the simplest geometries for a confining lattice. The interference of the incident and retro-reflected beams creates a standing wave with lattice sites at each antinode. In a second experiment, Friebel *et al.* demonstrated confinement of rubidium in a retro-reflected CO_2 laser beam ($\lambda = 10.6\mu$m) with oscillation frequencies of 15 kHz in the two transverse directions and 720 Hz in the longitudinal [Friebel *et al.*, 1998]. With 14000 atoms in each lattice site, they calculated a peak density of 3 $\times 10^{13}$ atoms per cm^3 and a phase space density of 1/300. Granade *et al.* used a similar geometry to evaporatively cool ^{6}Li to Fermi degeneracy [Granade *et al.*, 2002]. Starting with 10^5 atoms loaded into 6.6 kHz $\times$ 6.6'kHz $\times$ 340 Hz lattice site, they cooled the atoms to 4 μK, where the Fermi temperature is 8 μK.

A similar retroreflected geometry is employed by Vuletic *et al.* to confine atoms in a standing wave interference pattern [Vuletic *et al.*, 1998, Kerman *et al.*, 2000]. These experiments employ degenerate Raman sideband cooling in the lattice to reach temperatures as low as 300 nK with densities of 1.1 $\times 10^{11}$ and phase space densities of 1/500.

A 3D lattice of retroreflected beams detuned 165 GHz from resonance in Cesium achieved a phase space density of 1/30 by laser cooling 5×10^7 atoms in a lattice sites with all three oscillation frequencies equal to 180 kHz [Han *et al.*, 2000]. This group used a novel geometry which combined a retroreflected beam travelling vertically with

two orthogonal horizontal beams which are interferometrically locked to have a constant relative phase. This far-off resonant lattice employed 3D Raman sideband cooling to a temperature below 8 μK.

Dumke *et al.* demonstrated a dipole trap lattice made by passing an off-resonant beam through a microlens array [Dumke *et al.*, 2002]. The 50×50 array of $f = 625$ μm lenses generates an array of potential wells separated by 125 μm. Each lattice site traps $\simeq$ 1000 atoms at 20 μK temperatures. This experiment has the novel feature that individual lattice sites are addressable by a readout laser which is used to alter or detect the ground state of atoms in a site. This ability is useful for studies with quantum gate operations using lattice sites as data registers.

To date, evaporative cooling to Bose-Einstein Condensation in an optical trap has been reported by three groups, Takasu *et al.* [Takasu *et al.*, 2003], Weber *et al.* [Weber *et al.*, 2003], and Barrett *et al.* [Barrett *et al.*, 2001]. The group of Takasu *et al.* produced BEC in a cloud of ^{174}Yb atoms held at the intersection of a horizontal and a vertical far-off resonant beam. Ytterbium atoms are initially trapped in a MOT and approximately 10^6 are transferred to the crossed-beam FORT and confined at a temperature of 180 μ K. The authors report that evaporation does not lead to efficient cooling when the horizontal and vertical beams have similar intensities, as number losses are too high. When the two beams are initially held at different intensities, however, evaporation does not eject so many atoms. They begin with the horizontal beam of 5.0 Watts focused to 14 μm, and a vertical beam of 0.2 Watts focused to 11 μm, for maximum trap depths of 630 and 53 μK. Both beams are derived from a 532 nm wavelength frequency-doubled Nd:YAG laser. By gradually decreasing the power of the horizontal beam to 34 mW, the authors cool the atoms below the critical temperature of 730 nK, and achieve BEC of approximately 5×10^3 atoms. This Yb BEC has a number of interesting features which arise from ytterbium's two valence electrons: it

has singlet and triplet states coupled by very narrow intercombination transitions, and its singlet state is insensitive to external magnetic fields.

Weber *et al.* report on the creation of a Cesium BEC through evaporation in an all-optical trap. This is a remarkable achievement, given that the scattering length of Cesium is normally large and negative, - 160 nm [Kerman *et al.*, 2001], so that inelastic collisions prevent condensation of Cesium through traditional methods. The authors exploit a large Feshbach resonance at -8 Gauss to tune the scattering length of the atoms and thereby control the strength of their interactions by adjusting externally applied magnetic fields. Cesium atoms are loaded from a MOT into a large ($\sim$ 1 mm^3) and shallow ($\sim$ 10μK) FORT created by the intersection of two 100 Watt beams at 10.6 μm wavelength. The oscillation frequencies in this trap are low at 14 Hz, but its large volume permits the capture of 2×10^7 atoms. Free evaporation from this large and shallow trap is assisted by tuning the scattering length to a large a positive value, so that 10^6 atoms remain after cooling to 1 μK in 10 seconds. Atoms are further confined by the introduction of a second FORT, a $\lambda = 1064$ nm beam focused to 30 μm superposed on the wide and shallow FORT. Atoms collect into the more tightly confined FORT and phase space density increases to 10^{-2}. Three-body collisions are suppressed by decreasing the scattering length. Finally, the power in the narrow FORT is decreased over 17 seconds to a few milliwatts, and forced evaporation cools the cloud to 30 nK, and a condensate with 1.6×10^4 atoms forms.

Of the FORT experiments which have achieved condensation, the work of Barrett *et al.* is most similar to ours [Barrett *et al.*, 2001]. Their experiment employs two intersecting beams from a CO_2 laser at $\lambda = 10.6$ μm to collect 2×10^6 atoms from a ^{87}Rb MOT into a FORT. One beam is oriented horizontally, the second crosses it at 45 degrees in the vertical plane. Both begin with 12 Watts focused to 50 μm, for a mean trap oscillation frequency of 1.5 kHz. The authors pass both FORT beams through

acousto-optic modulators and introduce an 80 MHz frequency difference between them so that their electric fields are not coherent and no interference patterns are created. Thus only one potential well is formed, not a lattice. Free evaporation from the FORT occurs bringing the temperature to 38 μK in 1.5 seconds. The power in the beams is then decreased to 190 mW over two seconds. This produces a pure condensate with 3.5×10^4 atoms.

4.4 Apparatus

In this section we review the experimental apparatus used to achieve the Holographic Atom Trap. As seen in Figure 4.3, laser light at 1064 nm is generated by a Nd:YAG laser, modulated by an AOM, split by a holographic phase plate and relayed to the atoms by two transfer lenses.

4.4.1 YAG laser

Our flashlamp-pumped Nd:YAG laser is a model 818-ST manufactured by the Lee Laser corporation. Its active material is a rod of Neodymium-doped YAG crystal which is continuously pumped by a Xenon flashlamp. The laser is rated at 15 Watts output but we routinely are able to produce 18 or 19 Watts CW. The laser is equipped with a beam pick-off and photodiode which are used in a power-stabilizing servo circuit to regulate the output power. We rarely take advantage of this feature, choosing instead to operate the laser at maximum available power and regulate the intensity with our own noise-eater (see section 4.4.3).

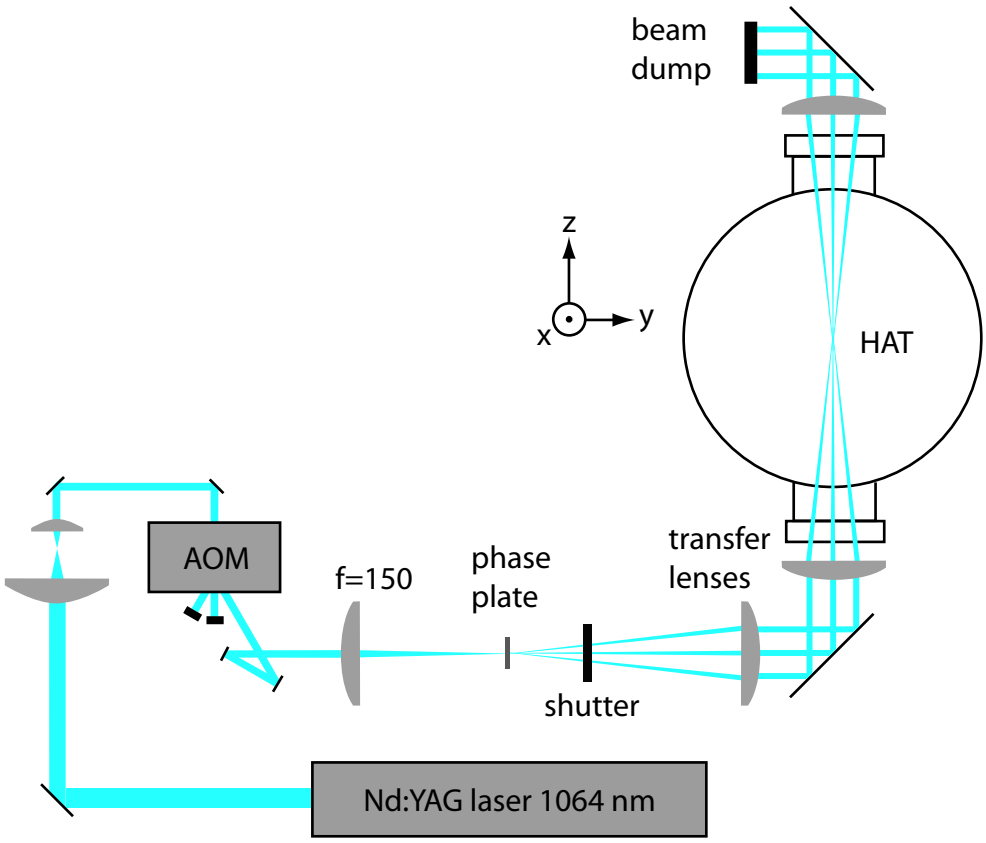

Figure 4.3: Experimental apparatus used for Holographic Atom Trap.

4.4.2 Acousto-optic modulator

We use an acousto-optic modulator (AOM) to control the intensity of YAG light sent to the atoms. The AOM is an Isomet model 1201-E2 driven by an 231-A2 variable-amplitude 40 MHz oscillator and RFA-108 amplifier. We use the first-order diffracted beam from the AOM for the HAT and block zeroth-order and higher-order beams in a beam dump. With 8W of RF power applied to the AOM, we achieve 86% diffraction efficiency into the first order beam. This corresponds to a loss of about 2.5 Watts. A simple telescope before the AOM reduces the YAG beam waist to 1 mm, the value recommended by Isomet. We have found that the diffraction efficiency has no significant dependence on the polarization of input light, as predicted by Isomet.

We found that the diffraction efficiency of the AOM as well as the profile of the diffracted beam were substantially improved by increasing the size of the entrance and exit windows on its case. The AOM was originally shipped with rectangular windows 5 mm by 4 mm. In this configuration we found that the first-order diffracted beam typically exited the AOM with a aspect ratio between 1.5:1 and 2:1. After drilling the windows out to 9 mm we achieved a more circular output beam.

This AOM exhibits the same tendency to steer the output beam as it heats up as the one which switches the imaging laser, discussed in greater detail in Section 2.5.1. To turn the AOM on we apply 8 Watts of radio-frequency power. Some of this power is transformed to heat by the RF transducer mounted on one of the crystal faces. This asymmetric heating establishes a temperature gradient in the AOM crystal once it is turned on. As a consequence, the output beam steers by a few milliradians in the first few hundred milliseconds after power is applied. This steering results in a translation of the YAG beam on the holographic phase plate on the order of a few tens of microns. Since the transfer lenses relay the plane of the phase plate to the center of the MOT,

this means the HAT slides to the side by the same few tens of microns when it is first turned on. Since the spatial extent of the MOT is a millimeter or more, we believe that this translation has no effect on the atoms in our HAT. Nonetheless it is a source of concern, and an AOM that exhibited less or no steering would clearly be preferable.

4.4.3 Noise eater

The intensity of the HAT beams is controlled by a simple feedback circuit which adjusts the amount of RF power applied to the AOM, Figure 4.4. A small amount of YAG light is picked off after the AOM and monitored with a fast photodiode. An op-amp compares the signal from this photodiode to a reference voltage and generates an error signal proportional to the difference. The error signal is fed back into the modulation input of the RF oscillator, so as to correct for any difference between the two. In this manner, intensity noise is substantially reduced, as seen in Figure 4.5.

The noise-eater circuit is further useful as a convenient way to ramp down the intensity of the HAT beams for forced evaporation. Since the circuit will always seek to equalize the photodiode signal and the reference voltage, decreasing the input reference voltage decreases the amount of light diffracted by the AOM. The highly linear response of the photodiode guarantees that the light intensity will respond linearly to changes in the reference voltage: the noise-eater circuit automatically compensates for the highly non-linear RF modulator and AOM efficiency.

The RF modulator used to control the YAG power is far from ideal for this application. The control input accepts an input signal voltage between -0.5 and +0.5 volts. A bias adjustment knob on the modulator allows the user to determine what input voltage within that range corresponds to zero output power, V_0. An input voltage different from V_0, whether more positive or more negative, will increase the output RF

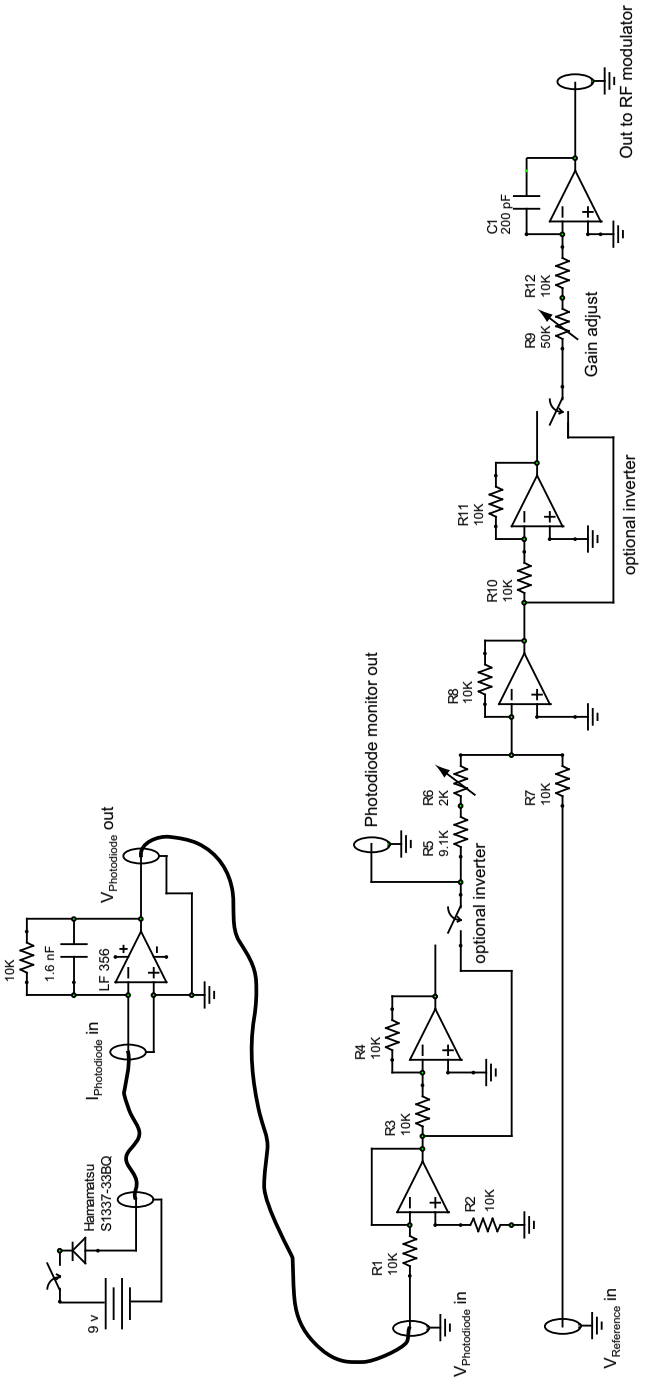

Figure 4.4: Circuit diagram for YAG intensity noise-eater.

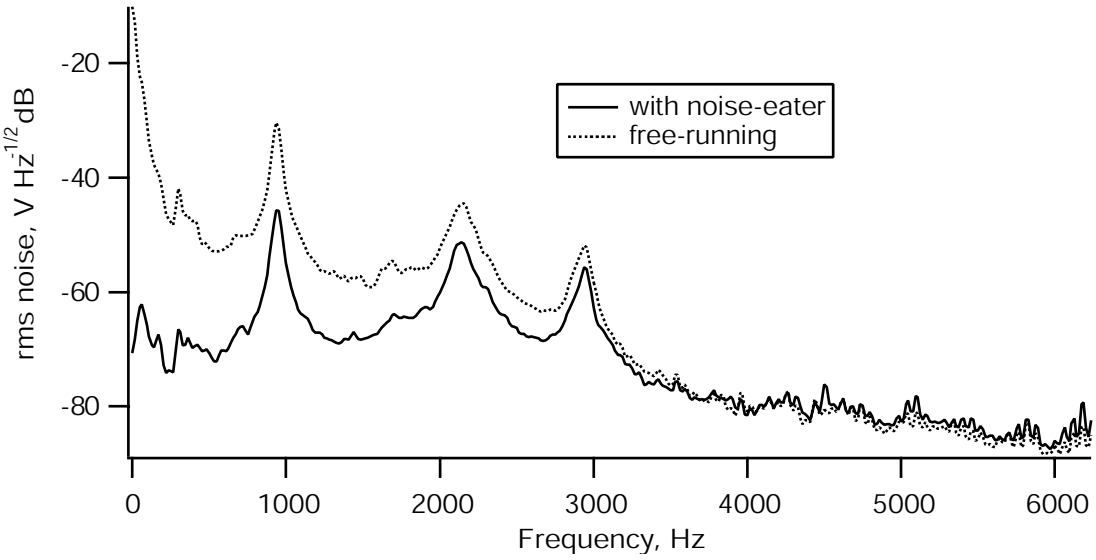

Figure 4.5: Intensity noise spectra with and without the noise-eater circuit.

power, as sketched in Figure 4.6.

This non-monotonic dependence on the control voltage is a problem for the noise eater circuit; the feedback loop will work for only one sign of the response curve. When performing forced evaporation experiments, we wish to decrease the intensity of the YAG laser to very low levels. As the control voltage is brought closer and closer to V_0, it is increasingly likely that a noise spike in that voltage will cross over to the other side of V_0 and the response curve of the modulator will change sign. This will drive the noise eater from negative feedback into positive feedback, and it will immediately maximize the YAG intensity. The result is that V_0 is an unstable point; it is not possible for the feedback circuit to regulate at zero light output, since the sign of the feedback changes there.

Our solution to this problem is to reduce the noise in the feedback system to an acceptable level. Forced evaporation experiments typically require that we decrease the intensity of the YAG laser to 1 to 2 milliwatts in the center beam. Given that

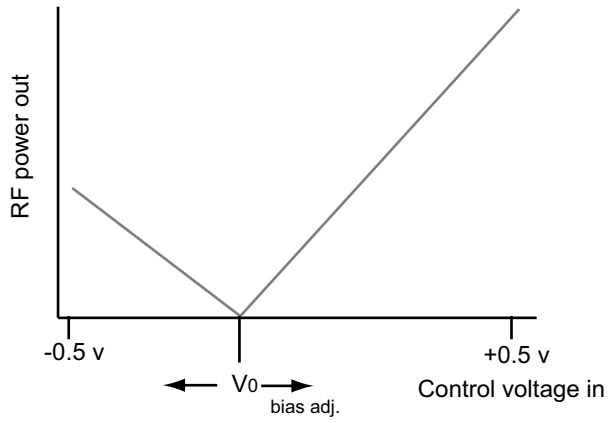

Figure 4.6: Qualitative diagram of RF power out versus control voltage in for RF modulator.

the center beam contains 5 Watts at full power, this requires a dynamic range in the intensity regulating circuit between 2500 and 5000. The maximum voltage generated by the photodiode and current-to-voltage converter is 10 Volts, so this dynamic range requires a noise level below 4 millivolts.

A number of steps have been taken to achieve this low noise level. A significant source of noise is the reference voltage output by the digital to analog converter on our National Instruments DAQ card. We found over 15 mV of ripple at 60 Hz and its harmonics, on top of 6 mV of high-frequency hash. Luckily, this DAQ card has multiple analog output channels, and the noise is highly correlated between them. We take advantage of this fact by subtracting the signals from two output channels in a differential amplifier: one channel outputs 0 V plus noise, the second outputs V_{ref} plus noise. The differential amplifier subtracts the two signals, creating a much cleaner version of V_{ref}. A circuit diagram is seen in figure 4.7.

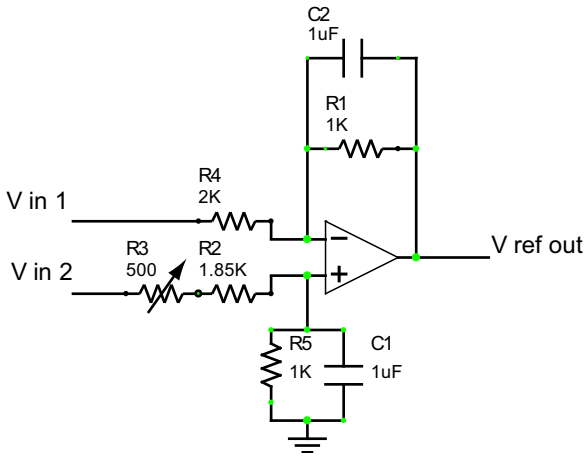

Figure 4.7: Differential amplifier used to reduce noise in reference voltage.

4.4.4 Holographic phase plate

Our holographic phase was manufactured by MEMS Optical, Inc. from fused silica. It consists of two perpendicular diffraction gratings of period 15.8 microns. This diffracts the incident beam into a square array of output beams. Typically 50%, or 5 Watts, of YAG light remain in the undiffracted zeroth order beam, and 10%, or 1 Watt, is diffracted into each of the four first-order beams. The remaining 10% of incident light is split into higher diffraction orders or scattered.

We use an $f = 150$ mm plano-convex lens to bring the light to a focus as it passes through the phase plate. We have measured the beam waist as a function of distance from the lens, as seen in Figure 4.8.

As seen in the figure, there is still an asymmetry in the beam as a result of diffraction in the AOM. The beam comes to a minimum waist of 70 μm in the horizontal plane and 91 μm in the vertical. The phase plate is positioned at 15.2 cm, where the waists are nearly equal.

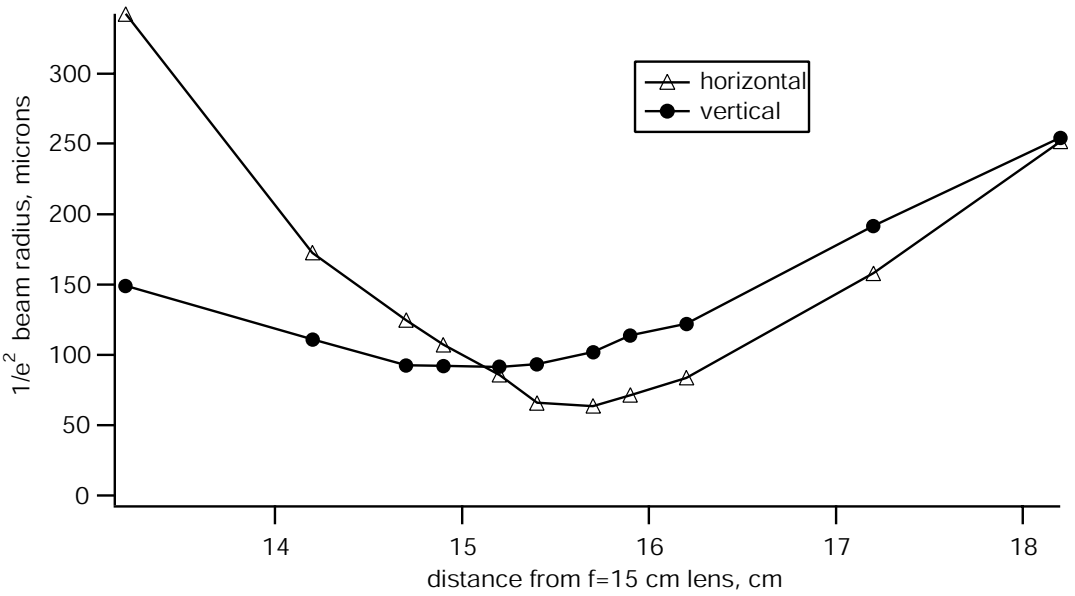

Figure 4.8: YAG beam waist vs position from $f = 15$ cm lens. Holographic phase plate is at 15.2 cm.

4.4.5 Transfer lenses

A pair of plano-convex lenses transfers the plane of the phase plate onto the middle of the atom cloud, creating the HAT. The lenses are $f = 300$ mm and $f = 200$ mm for a magnification of 2/3. Thus the laser beams at the HAT have a waist of 84 μm in the x-direction and 75 μm in the y-direction. Following their intersection at the HAT, the five YAG beams exit the vacuum chamber and strike an opaque beam dump.

4.5 Optimized loading procedure

In this section we review the steps necessary to load large numbers of atoms from the MOT into the HAT. The steps required are changes in the intensity and detuning of the MOT cooling laser and an increase in the magnetic field gradient.

We start with the steady state dark-SPOT MOT described in Chapter 3. This MOT typically contains $\approx 5 \times 10^6$ atoms. As discussed in Section 6.6, we believe that increasing the number atoms in the MOT past this number would substantially increase the number of atoms in the HAT. The primary trapping beams have a total intensity around 5 mW/cm^3 and detuning of -3 Γ. The anti-Helmholtz magnetic field has a gradient of 20 Gauss/cm at the center of the MOT.

The loading sequence begins when we increase the magnetic field gradient to 40 Gauss/cm by doubling the current in the anti-Helmholtz coils. This compresses the MOT spatially and temporarily increases the density of atoms at the trap center. We simultaneously shift the detuning of the cooling laser 3 Γ further from resonance. The addition of these steps increases the number of atoms trapped by a factor of two to four.

Twenty milliseconds after doubling the magnetic field gradient, and increasing the detuning we apply RF power to the AOM and turn on the YAG laser. For atoms in the center of the HAT, the AC Stark effect created by the YAG shifts the excited state $^2P_{3/2}$ manifold 6 Γ farther from the ground state $^1S_{1/2}$ manifold. (See section 5.2). The result is to shift the repumping laser from resonance to -6 Γ detuning, the cooling lasers from -6 Γ to -12 Γ detuning, and the depumping laser from +9 Γ to +3 Γ. Atoms in microtraps other than the centermost see less than the full intensity of YAG light and thus are Stark shifted by a value between zero and 6 Γ.

We allow atoms to load from the MOT into the FORT for 50 milliseconds. We then decrease the intensity of the cooling light by a factor of three. This increases the number of atoms loaded by a factor of two or more.

After spending 20 milliseconds in this highly-detuned low intensity state, we interrupt the current to the anti-Helmholtz coils and release the MOT into an optical molasses. After 5 milliseconds, the repumping laser and cooling lasers are extinguished.

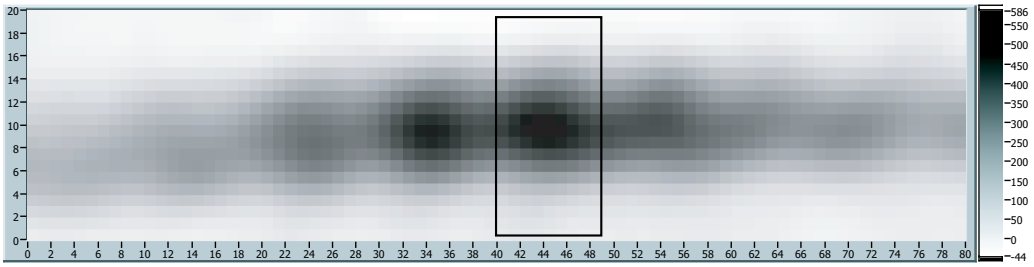

Figure 4.9: Absorption image of the HAT after optimized loading procedure.

4.6 Results

This section reviews general results obtained with our Holographic Atom Trap, including number, density, trap lifetime, and temperature after loading.

4.6.1 Number of atoms in the HAT

The most straightforward way to measure the number of atoms in the HAT is absorption imaging. As described in section 2.8, in the limit of long exposure times each atom will scatter an average of two $F = 1$ to $F' = 2$ photons before being pumped into the $F = 2$ ground state. With our calibrated detector it is thus rudimentary to count the number of photons absorbed from a probe beam and divide by two to find the number of atoms.

Figure 4.9 shows an image of the HAT after an optimized loading sequence (see Section 4.5). This image was taken with 8x8 binning so each pixel corresponds to a square 10.75 μm on a side. The z axis is in units of photons scattered per square pixel. We find the number of atoms in the Talbot fringe identified by the black rectangle to be 5.2×10^5.

Finding the number of atoms in a single microtrap is less straightforward. Since

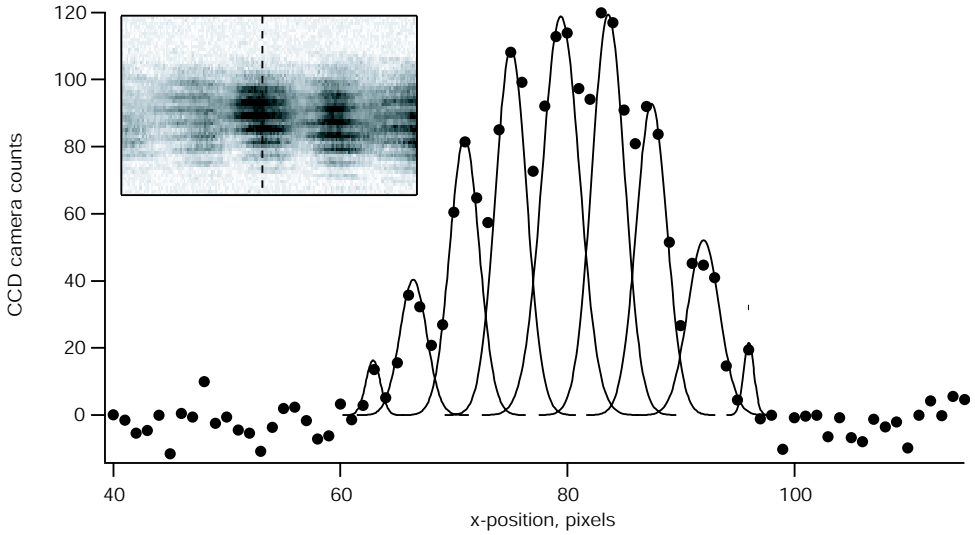

Figure 4.10: Cross-section of microtraps fit to series of Gaussian peaks.

the camera sees a side-view of a lattice, it sums over all the microtraps in the y-direction. Luckily the lattice is symmetric along the x- and y-directions, so we may make conclusions about the y-distribution based on our knowledge of the x-distribution. We take an image of the atoms with high spatial resolution (using 1x1 or 2x2 binning) and fit a cross-section in the x-direction to a series of gaussian peaks. We are generally interested in the fraction of atoms in the centermost microtrap, so we find the ratio of the height of the tallest peak to the sum of all the peak heights. This is the ratio of the number in the center well to the total number, as seen along the x-direction. We assume that this ratio is the same along the y-direction, and so the fraction of atoms in the center well is the square of what we measure along the x-direction.

Figure 4.10 shows a cross section in the x-direction fit to a series of gaussian peaks. The centermost peak has an amplitude of 120 counts and the sum of all their amplitudes is 652. Thus we estimate a center well fraction of $(120/652)^2 = 3.4\%$. We have found that 3% is a typical number. Thus we have 5.2×10^5 atoms in a Talbot fringe, and

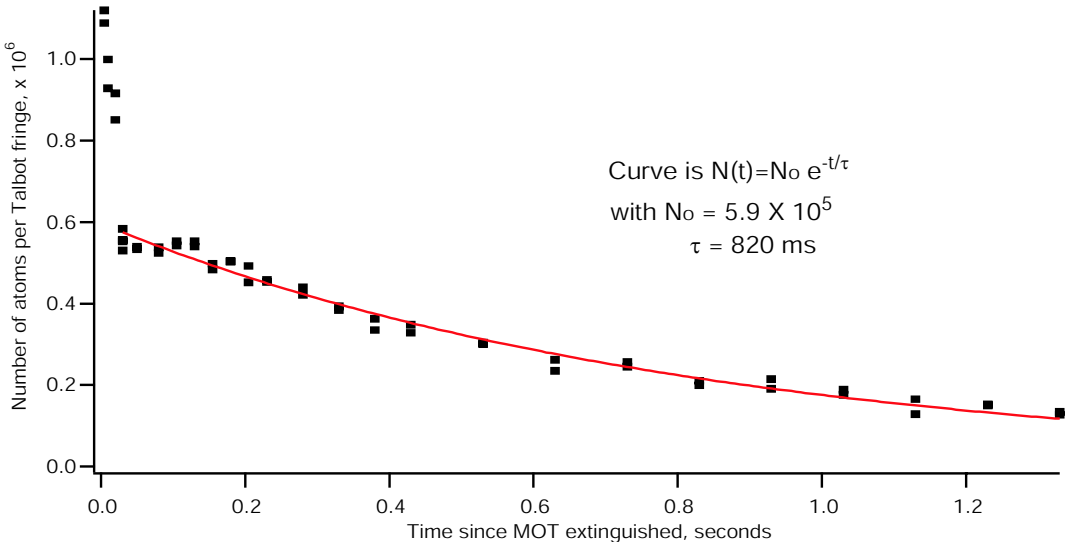

Figure 4.11: Number of atoms per Talbot fringe vs. time since MOT extinguished.

16,000 in the centermost microtrap.

4.6.2 Trap lifetime

We measure the lifetime of atoms in our Holographic Atom Trap by loading it as described in Section 4.5 and measuring the number of atoms remaining after a variable amount of time. After an initial period of high loss which we believe is due to rapid free evaporation from the HAT, the primary loss method is collision with untrapped background atoms. We thus expect the loss rate to be proportional to the number of atoms in the trap, and the number to follow an exponential decay curve. A lifetime curve is shown in Figure 4.11, fit to an exponential it corresponds to a $1/e$ lifetime of 820 milliseconds.

4.6.3 Temperature

The temperature of atoms in the HAT is measured with a time-of-flight expansion technique. After a sample is prepared the YAG laser beams are extinguished in $< 1\mu s$ by cutting RF power to the AOM. Once released, the atom cloud expands ballistically as it falls. We take images of the cloud at a series of times thereafter, and measure the expansion of the cloud. The expansion rate is related to the velocity distribution within the HAT prior to its release.

If the atom cloud has some initial width σ_0 and thermal velocity v prior to release, the observed width $\sigma(t)$ some time t later is the quadratic sum of the initial width and the expansion:

$$\sigma(t) = \sqrt{\sigma_0^2 + (vt)^2} \tag{4.26}$$

We analyze images of the expanded cloud by averaging along the z-axis and fitting the resulting profile to a gaussian bump on a linear background. We plot the growth of the gaussian versus time and fit it to equation 4.26 to find the initial width σ_0 and thermal velocity v.

Figure 4.12 shows one such expansion curve for atoms released from our HAT. The fit to equation 4.26 gives a velocity of 9.4 cm/s and an initial half-waist at the $1/e$ point of 40.5 μm. This velocity corresponds to a temperature of 45.9 μK in the HAT. We have found that 50 μK is a typical temperature for atoms in the HAT; regardless of the temperature of the MOT or the presence of doppler cooling light, we find the HAT temperature to be near 50 μK. This subject is discussed in more detail in Chapter 5, where we posit that this temperature is set by free evaporation from the trap.

4.6.4 Density

We calculate the peak density of atoms in the HAT according to equation 4.14.

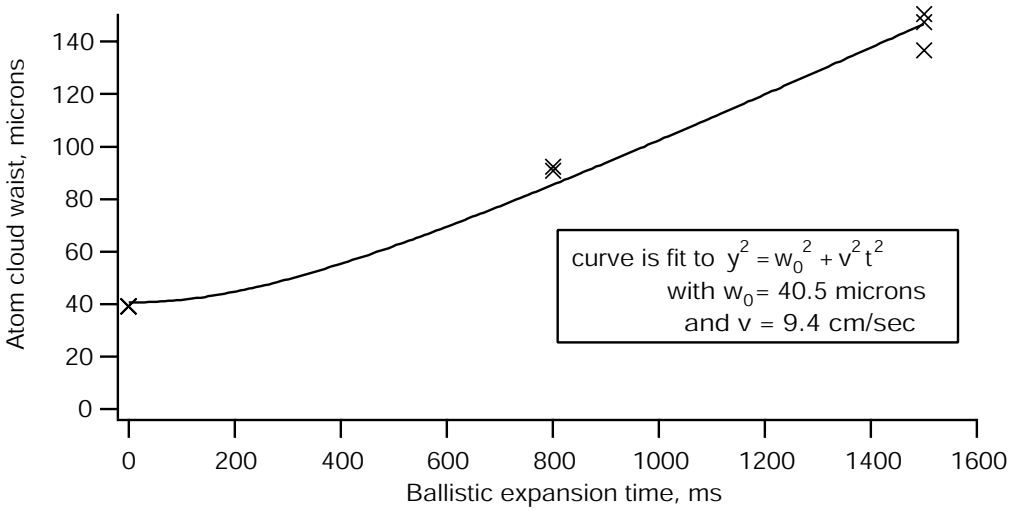

Figure 4.12: Ballistic expansion of atoms released from the HAT.

$$n_0 = N \left(\frac{2\pi M c^2}{k_B T} \right)^{3/2} \left(\frac{\nu_x \nu_y \nu_z}{c^3} \right) \tag{4.27}$$

With $N = 16,000$, $T = 50\mu$K and $\nu_x = \nu_y = 18.4$ kHz, $\nu_z = 780$ Hz, we find $n_0 = 2 \times 10^{14}$ cm^{-3}.

Similarly, phase space density is calculated with equation 4.15

$$\rho = N \frac{h\nu_x}{k_B T} \frac{h\nu_y}{k_B T} \frac{h\nu_z}{k_B T} \tag{4.28}$$

With the same input parameters, this indicates a phase space density of 1/260. Uncertainties in these measurements are discussed in Section 6.4.1.

4.7 Alternate geometries

As discussed in Section 4.2.3, the mean oscillation frequency of atoms in a trap decreases as the spatial size of the trap is increased. The advantage to making larger microtraps is that the number of atoms collected from the MOT increases. We must therefore find

a compromise between small traps with fewer atoms and high oscillation frequencies, and large traps with many atoms but low oscillation frequencies. Our HAT geometry allows us to vary the spatial size of our potential wells by altering the angle θ at which the five off-resonant beams converge. This is done by changing the focal lengths of the transfer lenses between the holographic phase plate and the HAT. Our standard $f = 300$ mm and $f = 200$ mm lenses give a magnification of 2/3, for our canonical $\theta = 100$ mrad geometry. A typical spatial heterodyne image is shown in Figure 4.13.

For this image we calculate 1.8×10^5 atoms per Talbot fringe, 12,600 atoms in the central mircotrap, and a peak phase space density of 1/420. These data and the data from other geometries presented here were collected before our HAT was fully optimized, and thus this image is not representative of the numbers presented above. Nonetheless, it is valid for comparison of the different geometries, as the imaging system and loading procedure was equivalent for each.

By swapping the $f = 300$ mm transfer lens for one with $f = 200$ mm, we changed the angle θ to 71 milliradians. In this configuration the microtraps each measure $14\mu m \times 14\mu m \times 200\mu m$ and the volume occupied by a single microtrap increases fourfold. The oscillation frequencies fall to 12 kHz, 12 kHz, and 350 Hz; lower by a factor of four. Thus the different geometry may or not be an overall improvement, depending on whether the number of atoms loaded into the microrap is greater or lesser than that expected. To implement this geometry we also had to change the lens which focuses the YAG onto the phase plate to counteract the change in magnification of the transfer lens system. A representative image is shown in Figure 4.14.

This image corresponds to 6.7×10^5 atoms per Talbot fringe, with 47,000 in the centermost microtrap. This corresponds to a peak phase space density of 1/500. So we conclude that there is no significant gain in this geometry.

We have also tried a $\theta = 50$ milliradian HAT, as seen in Figure 4.15.

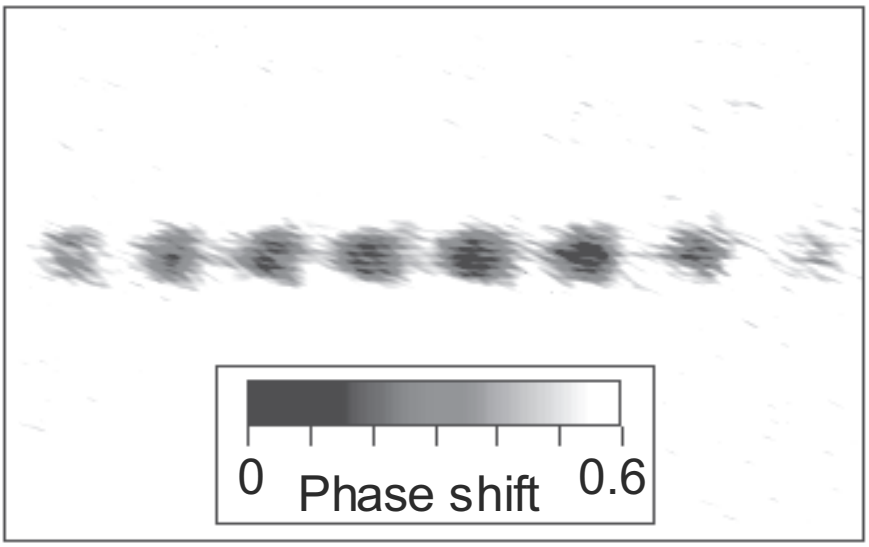

Figure 4.13: Image of HAT with $\theta = 100$ mrad.

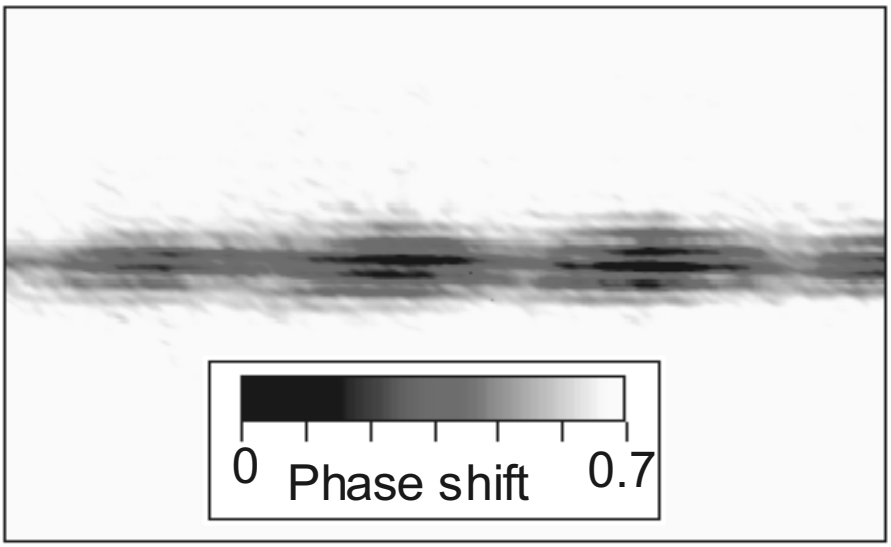

Figure 4.14: Image of HAT with $\theta = 71$ mrad.

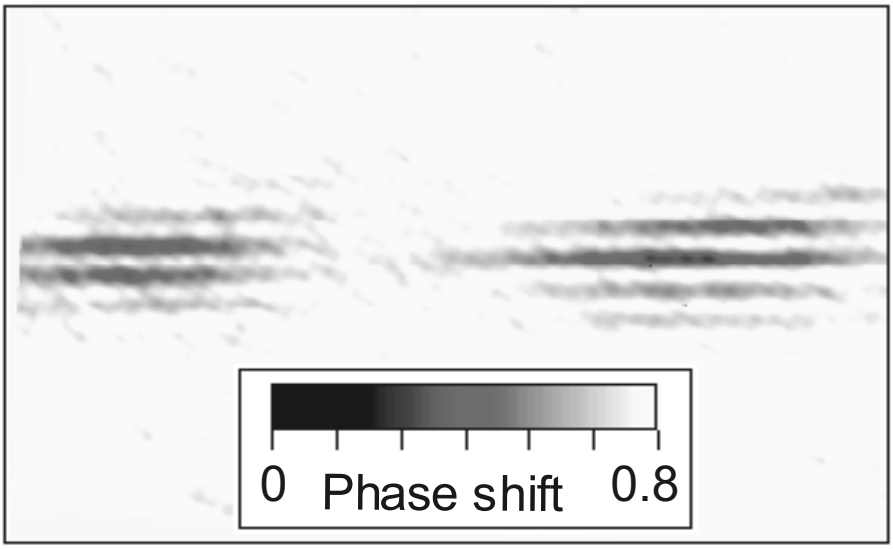

Figure 4.15: Image of HAT with $\Theta = 50$ mrad.

In this geometry the microtraps have increased in size to $20\mu m \times 20\mu m \times 400\mu m$, but the oscillation frequencies have fallen to 8 kHz, 8 kHz, and 175 Hz. This did not appear to be an advantageous trade-off, as the number of atoms in each Talbot fringe was only 3.2×10^5 and the center microtrap had 87,000 atoms. This was not enough to overcome the decrease in oscillation frequency, and the phase space density was 1/1000.

We also tried increasing the angle θ to generate smaller microtraps with higher oscillation frequencies. This was a difficult pursuit, as we found that the number of atoms loaded into the HAT fell sharply. With $\theta = 140$ milliradians we measured only a few thousand atoms per Talbot fringe under the best of circumstances. Based on these results we concluded that our chosen geometry with $\theta = 100$ mrad is a good choice.

Chapter 5

Laser Cooling in the HAT

5.1 Introduction

In this chapter we discuss studies achieve laser cooling in the Holographic Atom Trap. The results show that laser cooling is ineffective, as the temperature of atoms in HAT depended only on the intensity of the far-off resonant YAG laser and not on the intensity or detuning of more nearly resonant cooling lasers. As shown in Section 5.4, the temperature attained due to rapid free evaporation of atoms from the trap. In Section 5.2 we discuss the AC Stark shift created by the YAG laser and conclude that it is approximately 6 - 8 Γ at the maximum trap depth. The effects of this detuning on our prospects for laser cooling are discussed in Section 5.3. Section 5.5 reviews a number of possible heating mechanisms in the HAT, including Rayleigh scattering and laser intensity noise heating, and concludes that they should all be negligible. In Section 5.6 we describe an excited-state mixing process driven by the YAG laser and discuss the possibility that it prevents sub-Doppler cooling. A test experiment is described, and possible remedies are proposed.

5.2 AC Stark shift

As discussed in section 4.2.1, the presence of the intense YAG laser shifts the energy levels of the rubidium atoms by an amount proportional to the polarizability; $U(\mathbf{r}) = -\alpha|E|^2$. The polarizability is in general a tensor quantity given by

$$\tilde{\alpha} = \sum_b \frac{-2\omega_{ba}e^2}{\hbar\left(\omega^2 - \omega_{ba}^2\right)} \langle a|\hat{r}|b\rangle \langle b|\hat{r}|a\rangle \tag{5.1}$$

which depends on the frequency of the laser field and the two states $|a\rangle$ and $|b\rangle$. For linearly polarized light the scalar component α_0 can be related to the oscillator strength f_{ab} through

$$\alpha_0 = \frac{e^2 f_{ab}}{M\left(\omega_{ba}^2 - \omega^2\right)} \tag{5.2}$$

Similarly, the tensor polarizability can be written as

$$\alpha_2 = \frac{e^2 f_{ab}\, \Phi_2(J_a, J_b)}{M\left(\omega_{ba}^2 - \omega^2\right)} \tag{5.3}$$

where $\Phi_2(J_a, J_b)$ depends on the J-values of $|a\rangle$ and $|b\rangle$. These relations are valuable because they are in terms of oscillator strengths which have been carefully measured [Heareus *et al.*, 1961]. We can thus calculate the polarizabilities of the $5S_{1/2}$, $5P_{1/2}$ and $5P_{3/2}$ states at the 1064 nm wavelength of our YAG laser:

$$\alpha\left(5S_{1/2}\right) = 98.8\ \mathring{A}^3 \tag{5.4}$$

$$\alpha\left(5P_{1/2}\right) = -187.4\ \mathring{A}^3 \tag{5.5}$$

$$\alpha\left(5P_{3/2}\right) = -271.0\ \mathring{A}^3 \tag{5.6}$$

One of these values has been measured and reported in the literature, Kadar-Kallen and Bonin found $\alpha_0\left(5S_{1/2}\right) = 114 \pm 9\ \mathring{A}^3$, which agrees with our prediction within 10% [Kadar-Kallen and Bonin, 1992].

With these values we can calculate not only the depth of the potential well created by our HAT (done in section 4.2.5), but also the shift in spacing between the energy

levels. This is important because the cooling and detection lasers are all locked to non-shifted transitions: as the ac-Stark shift moves the energy levels up or down, it changes the effective detuning of the lasers. The frequency shift of a single energy level is given by $\Delta\nu_a = -\alpha_a I/\hbar c$ and so the shift of a transition between two levels is $\Delta\nu_{ab} = -(\alpha_a - \alpha_b)I/\hbar c$. It is convenient to relate the scalar portion to the trap depth $U_{max} = -2\pi\alpha_0 \left(5S_{1/2}\right) I/c$.

$$\frac{\Delta\nu_{5P_{1/2}\rightarrow 5S_{1/2}}}{U_{max}} = \frac{\alpha\left(5P_{1/2}\right) - \alpha\left(5S_{1/2}\right)}{h\ \alpha\left(5S_{1/2}\right)} \tag{5.7}$$

$$\Delta\nu_{5P_{1/2}\rightarrow 5S_{1/2}} = -6.0\ MHz \times \frac{U_{max}}{100\ \mu K} \tag{5.8}$$

Similarly for the $5P_{3/2}$ manifold,

$$\Delta\nu_{5P_{3/2}\rightarrow 5S_{1/2}} = -7.8\ MHz \times \frac{U_{max}}{100\ \mu K} \tag{5.9}$$

For every 100 μK of trap depth, the $5S_{1/2}$ ground state moves down 0.35 Γ, the $5P_{1/2}$ excited stated moves up 0.65 Γ, and the $5P_{3/2}$ excited state moves up 0.95 Γ.

Our spatial heterodyne imaging system offers a convenient way to measure these Stark shifts. The measured phase shift created by the atom cloud depends on the detuning of the imaging laser from resonance, so a change in the energy spacing of the transition effects the measured signal. Sweeping the laser frequency across resonance with the Stark shifted atoms reveals that the resonance occurs when the laser is off resonance with non-Stark shifted atoms; this difference is the amount of Stark shift.

One such resonance curve is seen in Figure 5.1. This data was taken with a less-intense YAG so the maximum trap depth was 430 μK. We would thus predict that the $P_{1/2} \rightarrow S_{1/2}$ imaging transition is Stark shifted by 4.3 Γ. As seen in the figure, the Stark-shifted atoms are resonant with the imaging laser when it is detuned by 3.2

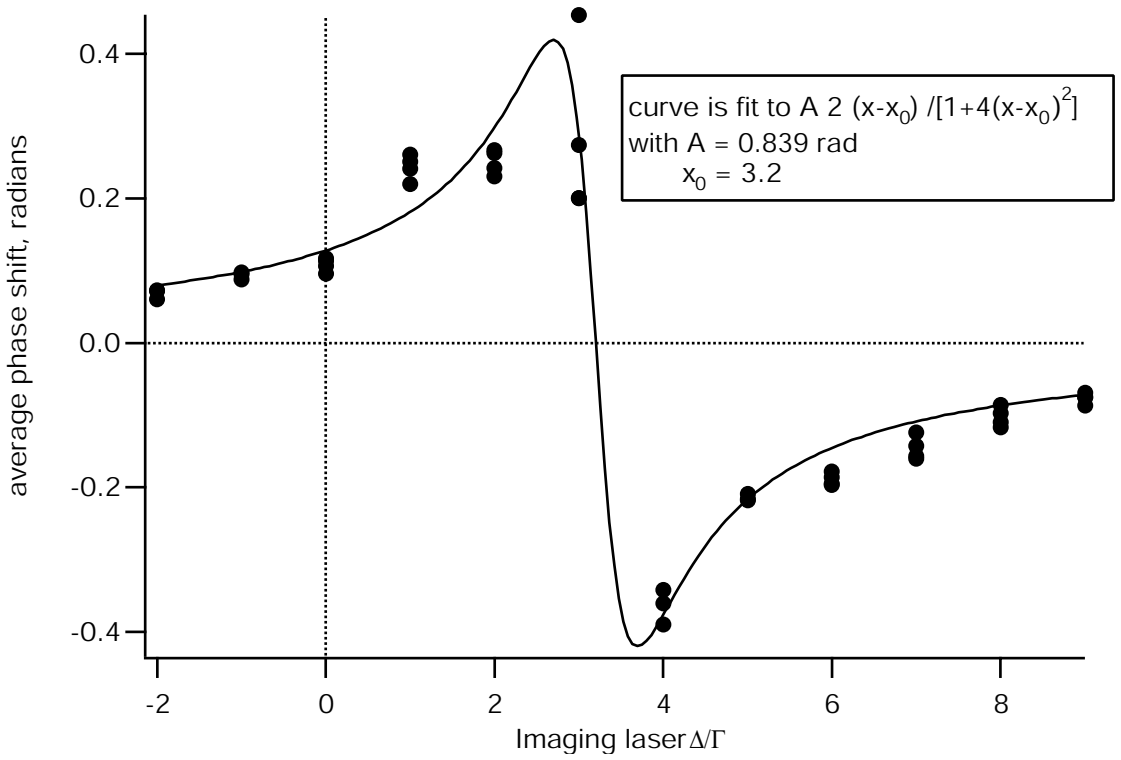

Figure 5.1: Detected phase shift vs imaging laser detuning

Γ from resonance with non-shifted atoms. This discrepancy may be attributed to the uncertainty in the potential depth, and the need to correct the phase shift measurements for absorption near resonance (see Section 2.6.1).

5.3 Sub-Doppler cooling

Although we have found the MOT temperature to depend on the intensity and detuning of the cooling laser (Section 3.3.2), the temperature of atoms in the HAT remains fixed at a value one-tenth the maximum trap depth (Section 4.6.3).

If sub-Doppler cooling were to occur in the HAT, we would expect to see the temperature of trapped atoms decrease with decreasing intensity of the $5S_{1/2}F = 2 \rightarrow$

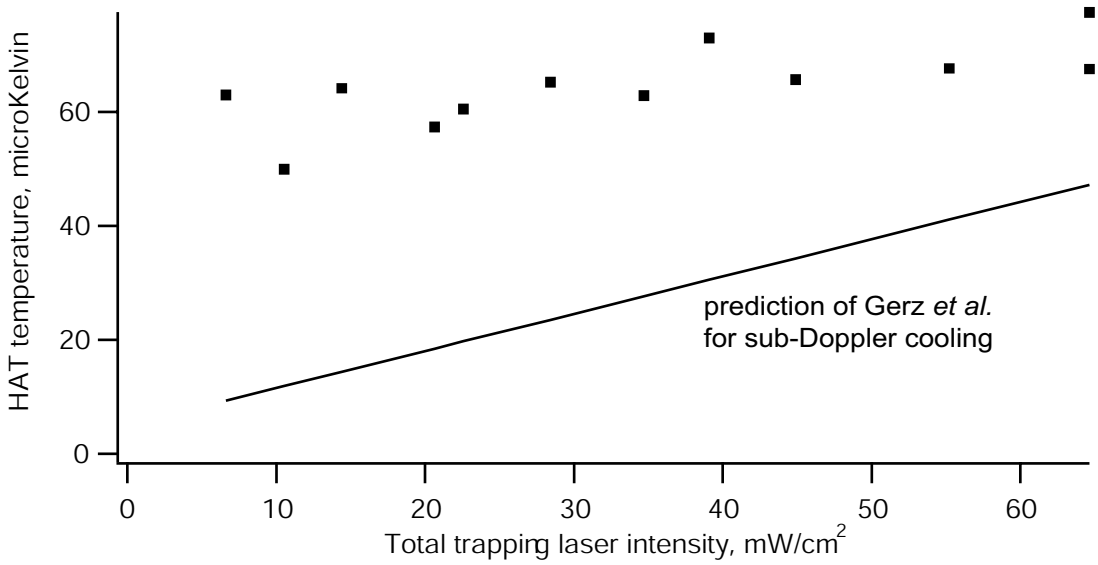

Figure 5.2: HAT temperature versus total intensity of cooling laser.

$5P_{3/2}F' = 3$ cooling light [Metcalf and van der Straten, 1999, Gerz *et al.*, 1993]. To test this we loaded the HAT according to our standard procedure and varied the intensity to which the cooling light is switched for the final 20 milliseconds of loading. The results are seen in Figure 5.2. The temperature shows little if any dependence on the laser intensity, and certainly does not follow the values predicted for sub-Doppler cooling.

One possible explanation for the inhibition of sub-Doppler cooling is the effect of the Stark shift on the repumping laser. This laser is locked to be on resonance with non-Stark shifted atoms, but those held in the HAT see a larger effective detuning because the levels are shifted away from resonance. This detuning decreases the repumper effectiveness and leaves atoms in the uncooled $F = 1$ state longer. To compensate for this, we varied the repumper detuning while measuring the HAT temperature to see sub-Doppler cooling, Figure 5.3. The horizontal scale shows the detuning from resonance, in units of the natural linewidth Γ, as seen by the Stark shifted atoms. The

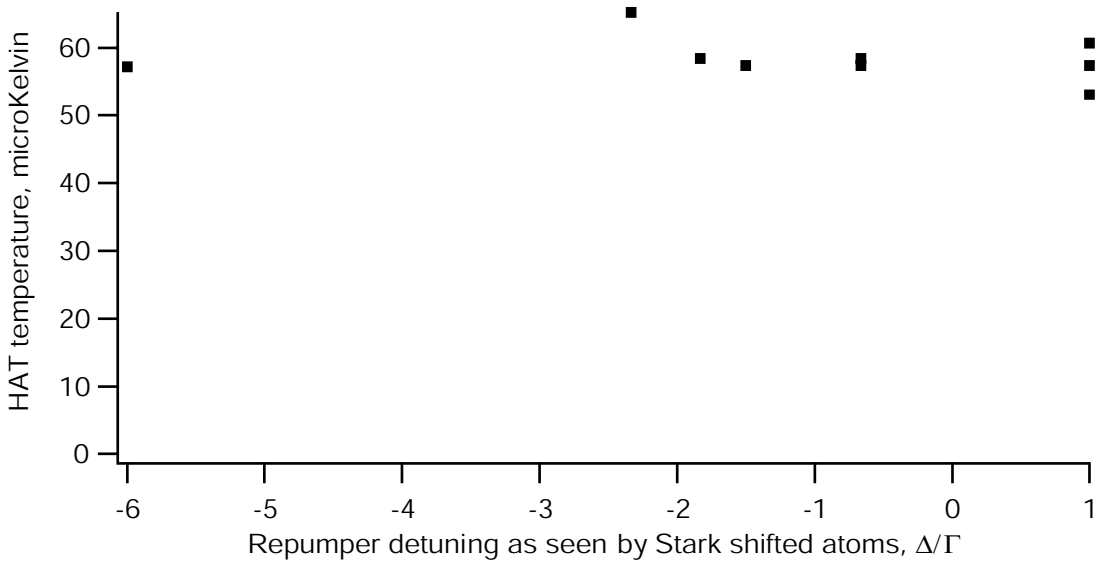

Figure 5.3: HAT temperature versus detuning of repumper laser.

data points at -1.5 Γ correspond to a repumper scattering rate of one photon every 12 microseconds. Since the low-intensity cooling stage lasts 20 milliseconds, there should be no suppression of sub-Doppler cooling due to an overly dark sample. Nonetheless, the HAT temperature does not indicate any sub-Doppler cooling.

For laser cooling, the temperature of trapped atoms should decrease with increasing cooling laser detuning. To look for this effect we varied the final Ti:sapph laser detuning in our standard loading sequence. As can be seen in Figure 5.4, atoms in the HAT again remained near 50 μK, rather than cool to the molasses temperature predicted. These data were taken with the repumping laser shifting to 2 Γ below resonance with the Stark shifted atoms during the highly-detuned cooling laser phase.

Once again we see that the HAT temperature does not follow the molasses temperature one would predict if sub-Doppler cooling were taking place.

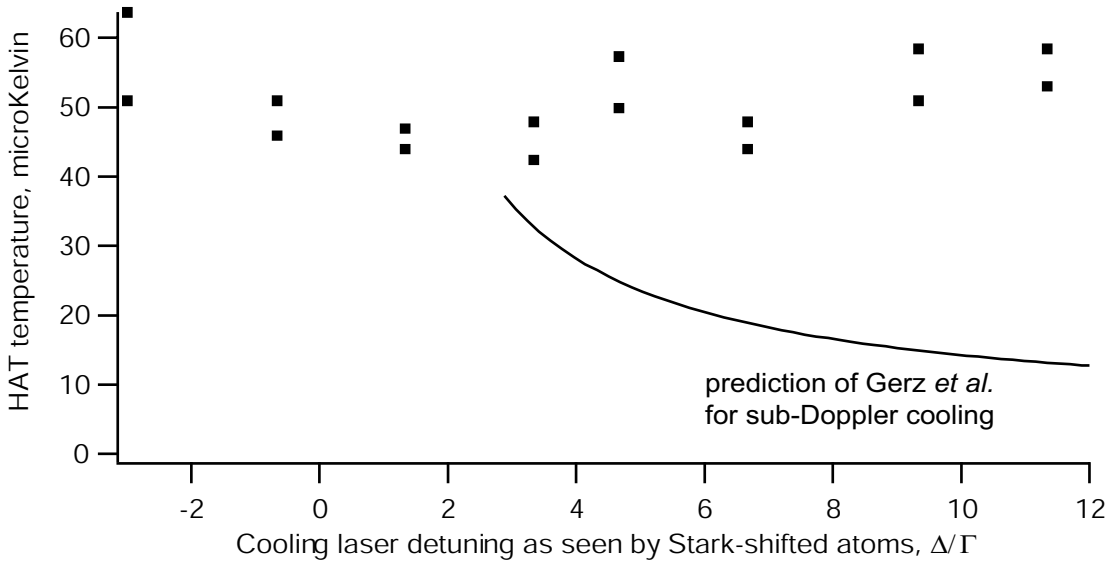

Figure 5.4: HAT temperature versus detuning of cooling laser.

5.4 Free evaporation

We believe that the temperature of atoms in the HAT is determined by the process of free evaporation [Ketterle and van Druten, 1996]. An elastic collision between two trapped atoms will occasionally give one of them the majority of their shared kinetic energy. If this kinetic energy is greater than the potential depth of the trap, the atom will be ejected and lost to the background gas. Over the course of several such elastic collisions, the trap loses energy and is cooled. This process proceeds until the temperature in the trap is low enough that no collisions result in an atom with enough energy to escape. This temperature is typically one-tenth the depth of trap.

We have seen that the temperature in the HAT falls from above 70 μK to 50 μK (one-tenth the trap depth) within 25 milliseconds of the end of the loading process (see Figure 5.5). This decrease in temperature is accompanied by a rapid fall in the number of atoms from over 1×10^6 per Talbot fringe to 5.8×10^5 over the same time period,

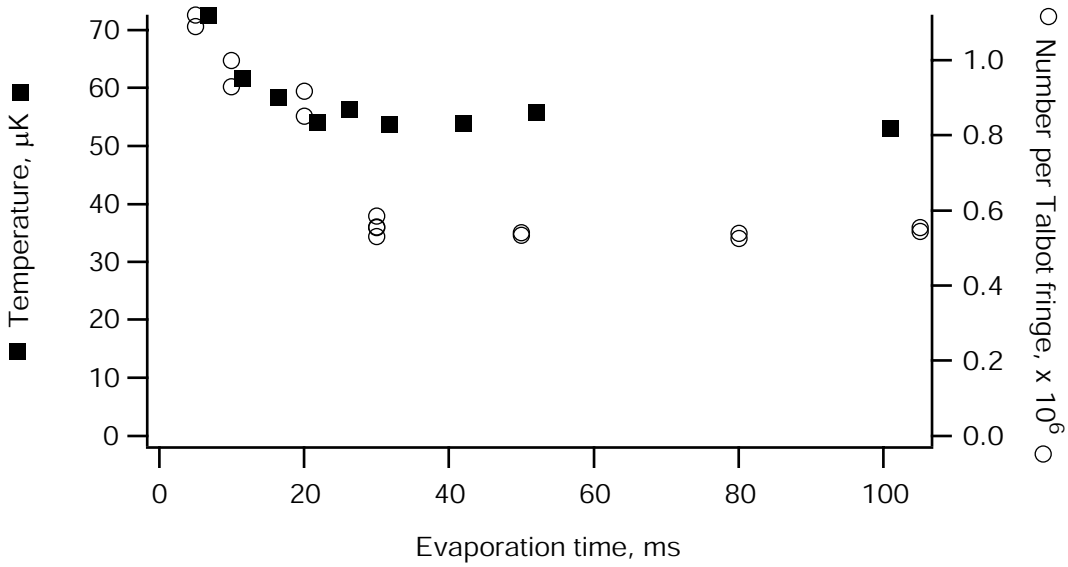

Figure 5.5: Temperature (black squares, left) and number of atoms (white circles, right) in the HAT during free evaporation.

just as one would expect for free evaporation.

It is certainly not surprising that free evaporation should occur rapidly in our HAT; the high densities lead to high collision rates. The question addressed in the rest of this chapter is why the temperature seems to be determined only by free evaporation– why laser cooling is unable to reduce the temperature further.

5.5 Heating mechanisms

In this section we discuss several possible heating mechanisms within the Holographic Atom Trap. These were analyzed in an attempt to account for the 50 μK HAT temperature, even when the MOT and associated molasses temperatures are only 6 to 8 μK. Ultimately, none of these heating sources is found to be large enough to explain the discrepancy.

5.5.1 Rayleigh scattering

Even though the YAG laser at $\lambda = 1064nm$ is far from resonance with any transition in Rubidium, there remains a nonzero probability of atoms scattering photons from it. Since each scattered photon imparts momentum to the atom, many such events would heat the trapped atom cloud.

The cross-section for Rayleigh scattering is

$$\sigma_{Rayleigh} = \frac{8\pi}{3} r_e^2 \omega_L^4 \left(\sum_e \frac{f_{eg}}{\omega_{eg}^2 - \omega_L^2} \right)^2 \tag{5.10}$$

where r_e is the classical electron radius and ω_L is the angular frequency of the exciting laser. ω_{eg} is the frequency corresponding to the energy difference between the atoms ground state g and an excited state e, and f_{eg} is the oscillator strength of that transition. The sum runs over all excited states, but in practice it is necessary only to sum over the transitions closest to resonance with the incident photons, for the $\omega_{eg}^2 - \omega_L^2$ denominator makes other terms negligible. Summing over the $^2S_{1/2} \rightarrow {}^2P_{3/2}$ and $^2S_{1/2} \rightarrow {}^2P_{1/2}$ excited states at 780 nm and 795 nm, we find

$$\sigma_{Rayleigh} = 4.23 \times 10^{-23} cm^2 = 5.32 \times r_e \tag{5.11}$$

This is a very small cross section, as we would expect given the off-resonant light.

It is straightforward to calculate the heating rate from this cross section. The scattering rate is the photon flux times the cross section, which for our standard 8 Watt beam focused to an 85 μm waist is 0.36 photons/second. The energy change resulting from one scattering event is $\hbar^2 k^2/m = 204\, nK$, for a total heating rate of 74 nK/second. This is low enough to be irrelevant to our 50 μK HAT.

5.5.2 Intensity noise heating

The intensity of the YAG laser fluctuates with noise in its power supply and shot noise in the gain medium. Even with the noise-eater circuit (see section 4.4.3) stabilizing the intensity, fluctuations are measurable. These fluctuations change the effective depth of the HAT potential well, and change the effective spring constants of the potential. These two effects were analyzed in the papers by Savard and Gehm [Savard *et al.*, 1997, Gehm *et al.*, 1998]. Given the fractional intensity noise $\varepsilon(t) = (I(t) - I_{avg})/I_{avg}$, the effect is treated as a first-order perturbation to a harmonic oscillator hamiltonian:

$$H = \frac{p^2}{2m} + \frac{1}{2}\, m\, \omega_{trap}^2\, r^2\, [1 + \varepsilon(t)] \tag{5.12}$$

The rate to make a transition from $|n\rangle \rightarrow |m\rangle$ in time T is

$$R_{m \leftarrow n} = \frac{1}{T} \left| \frac{-i}{\hbar} \int_0^T H'_{mn} e^{i\omega_{mn} t'} dt' \right|^2 \tag{5.13}$$

If T is short compared to changes in populations but long compared to fluctuations in $I(t)$, it can be expressed

$$R_{m \leftarrow n} = \left(\frac{M\omega_{trap}^2}{2\hbar} \right)^2 \left| \langle m|r^2|n\rangle \right|^2 \int_{-\infty}^{\infty} \langle \varepsilon(t)\varepsilon(t+\tau)\rangle\, e^{i\omega_{mn} t} d\tau \tag{5.14}$$

where we have defined the first-order correlation function

$$\langle \varepsilon(t)\varepsilon(t+\tau)\rangle = \frac{1}{T} \int_0^T \varepsilon(t)\varepsilon(t+\tau) dt \tag{5.15}$$

Using matrix elements for the position operator r^2 with $m = n \pm 2$ and $\omega_{m=n\pm2} = \pm 2\omega_{trap}$, we find the transition rate to be

$$R_{n\pm2,n} = \frac{\pi\omega_{trap}^2}{16} S_\varepsilon(2\omega_{trap})(n + 1 \pm 1)(n \pm 1) \tag{5.16}$$

where $S_\varepsilon(\omega)$ is the one-sided noise power spectrum

$$S_\varepsilon(\omega) = \frac{2}{\pi} \int_0^\infty cos(\omega\tau) \langle \varepsilon(t)\varepsilon(t+\tau)\rangle d\tau \tag{5.17}$$

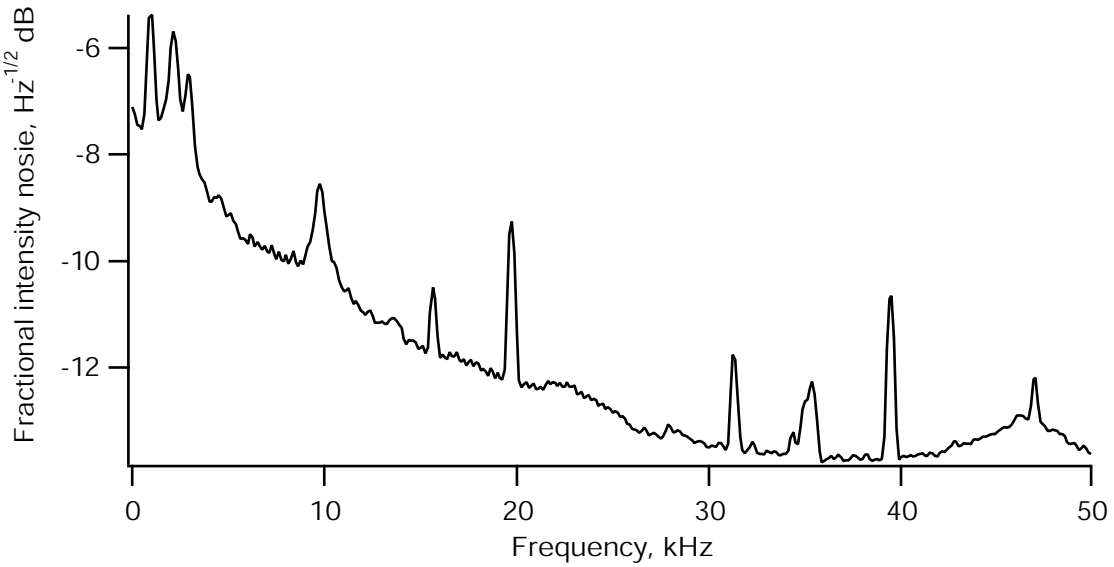

Figure 5.6: Intensity noise spectrum of YAG laser.

For an initial average energy $\langle E \rangle$, the resulting heating rate is

$$\left\langle \frac{dE}{dt} \right\rangle = \pi^2 \omega_{trap}^2 \, S_\varepsilon(2\nu_{trap}) \, \langle E \rangle \tag{5.18}$$

so we conclude that intensity noise on the laser causes an exponential increase in temperature, with a rate constant of $\Gamma_{Inoise} = \pi^2 \omega_{trap}^2 \, S_\varepsilon(2\nu_{trap})$.

We have measured the intensity noise of our flashlamp pumped Nd:YAG laser with a low-noise, 50 MHz- bandwidth photodiode and Stanford Research model SR760 spectrum analyzer. A sample spectrum is shown in Figure 5.6. At twice the transverse oscillation frequency of 18 kHz, the intensity noise is $S_\varepsilon(2\nu_{trap}) = 7.7 \times 10^{-14} \, Hz^{-1/2}$, and at twice the longitudinal frequency of 780 Hz, it is $S_\varepsilon(2\nu_{trap}) = 5.5 \times 10^{-12} \, Hz^{-1/2}$. Based on these measurements, we conclude that intensity noise heats the trap at a rate $\Gamma_{Inoise} = 0.0022 \, Hz$, or it takes 453 seconds for the temperature to increase by a factor of e. This is far below the trap lifetime, and thus negligible.

5.5.3 Pointing fluctuation heating

Just as intensity noise in the far-off resonant laser can cause heating in the trap, so too can mechanical vibrations in the optics or pointing fluctuations in the laser. Once again the papers by Savard and Gehm [Savard *et al.*, 1997, Gehm *et al.*, 1998] treat this effect as a perturbation to the Hamiltonian:

$$H = \frac{p^2}{2m} + \frac{1}{2}\, M\, \omega_{trap}^2\, [r - \varepsilon_r(t)]^2 \tag{5.19}$$

In this case the rate to make a transition is

$$R_{n\pm1,n} = \frac{\pi\omega_{trap}^3}{2\hbar} M\; S_\varepsilon(\omega_{trap})\; (n + 1/2 \pm 1/2) \tag{5.20}$$

and the resulting heating rate is

$$\left\langle \frac{dE}{dt} \right\rangle = \frac{\pi}{2} M\; \omega_{trap}^4\; S_\varepsilon(\omega_{trap}) \tag{5.21}$$

We measured the movement of the YAG laser beam by dividing it into two equal beams with a 50/50 non-polarizing beam splitter. One beam was attenuated by 50% with a neutral density filter, the other was half obstructed by a razor blade. Both beams were incident on photodiodes, and the photocurrents were subtracted. Any movement of the YAG beam would change the amount of light blocked by the razor blade but would not change the amount transmitted by the neutral density filter, so the subtraction circuit would register a difference. On the other hand, any changes in the total amount of light from the laser would affect both beams identically, so the subtraction circuit would not register a change. Thus the difference signal was sensitive only to steering changes in the YAG laser beam, not overall intensity noise.

As seen in Figure 5.7, the pointing noise is very small at frequencies above 2 kHz. This is not surprising, given that this noise is primarily mechanical in nature. At the longitudinal trap frequency of 780 Hz we measure the noise to be $S_\varepsilon(\nu_{trap}) \leq 1.8 \times$

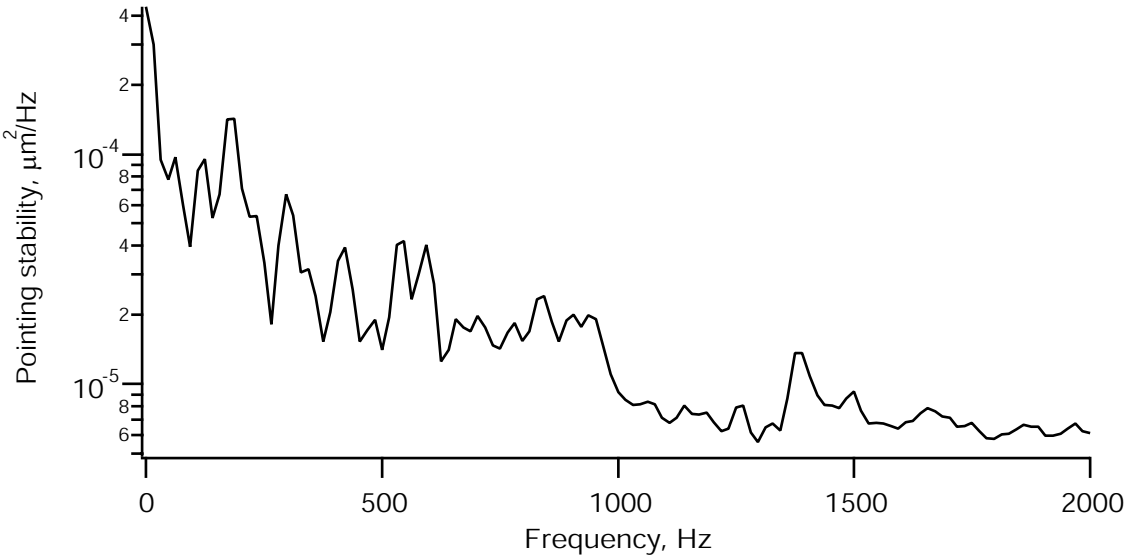

Figure 5.7: Pointing fluctuation spectrum of YAG laser.

10^{-5} $\mu m^2/Hz$, for a heating rate of $< dE/dt >= 1.2\ nK/sec$. For the transverse trap frequencies of 18 kHz, the noise is $S_\varepsilon(\nu_{trap}) \leq 6.0 \times 10^{-6}\ \mu m^2/Hz$, which corresponds to a heating rate of $< dE/dt >= 1.0\ \mu K/sec$. Neither of these heating rates is large enough to be significant to our HAT.

5.5.4 Background collision heating

The magneto-optical trap, and thus our HAT, are loaded from a room-temperature vapor of rubidium at $\sim 10^{-8}$ torr. Collisions between hot untrapped atoms and atoms in the HAT, whether elastic or inelastic, almost always eject the trapped atoms. Diffractive collisions, in which the recoil angle is very small, can transfer a tiny amount of momentum; enough to heat the trapped atom without ejecting it. These collisions were analyzed in the paper by Bali *et al.* [Bali *et al.*, 1999]. They found that the maximum energy which can transferred to an atom through a diffractive collision is related to the

classical scattering cross-section σ:

$$\Delta E_d = \frac{4\pi\hbar^2}{M\sigma} \tag{5.22}$$

For ^{87}Rb, this works out to $\Delta E_d = 2.8\,mK$. Given that our trap is at most 0.6 mK deep, only collisions well into the diffractive regime can cause heating without loss.

The rate for an incident atom to scatter into a solid angle $d\Omega$ is given by

$$\gamma_d \Omega = n_p\, v_r\, \frac{d\sigma}{d\Omega} d\Omega \tag{5.23}$$

where n_p is the background gas density, v_r is the recoil velocity, and $d\sigma/d\Omega = |f(\theta_r)|^2$ is related to the scattering amplitudes $f(\theta)$. We can define a threshold recoil angle θ_0 above which atom escapes as $\Delta E(\theta_0) = U_0$ where U_0 is the maximum trap depth. The heating rate is the rate of all collisions with $\theta_r \leq \theta_0$ times the amount of energy each collision imparts.

$$\frac{dE}{dt} = n_p\, v_r \int_0^{\theta_0} 2\pi\, |f(\theta_r)|^2\, \Delta E(\theta_r)\, \sin\theta_r\, d\theta_r \tag{5.24}$$

We cannot measure $|f(\theta_r)|$ or v_r directly, but they are related to the collisional loss rate γ_{col} through

$$\gamma_{col} = n_p\, v_r \int_{\theta_0}^{\pi} 2\pi\, |f(\theta_r)|^2\, \sin\theta_r\, d\theta_r \tag{5.25}$$

which is measurable. Combining these equations and assuming a Maxwell distribution for v_r yields a heating rate in terms of measurable quantities:

$$\frac{dE}{dt} = 0.37 \times \gamma_{col}\, \frac{U_0^2}{\Delta E_d} \tag{5.26}$$

As discussed in Section 4.6.2, we have measured the loss rate of atoms in the HAT. Assuming that all this loss is the result of collisions with background atoms (the worst case scenario for the collisional heating rate), our measurement corresponds to $\gamma_{col} =$ 1.22 /sec. Combining this with our measured typical trap depth $U_0 = 660\ \mu$K, we find

the heating rate $\langle dE/dt \rangle = 70\,\mu$ K/sec. This is large enough to be a concern only when the atoms are held in the HAT for times comparable to 1 second. For our typical 50 millisecond loading sequence it is not an appreciable effect.

5.6 Excited state mixing

Since none of the heating processes considered appears capable of generating the 50 μK HAT temperature, we must find another explanation for the inhibition of sub-Doppler cooling. Our current belief is that laser cooling within the HAT is frustrated by an excited state mixing process driven by the YAG laser. Sub-Doppler cooling relies upon the atoms making transitions between the $|m_J\rangle$ sublevels of the J= 1/2 ground state at specific locations within the laser cooling field [Dalibard and Cohen-Tannoudji, 1989, Ungar *et al.*, 1989]. If the atoms are allowed to make transitions between the ground states at inappropriate times, sub-Doppler cooling will be spoiled.

We believe that the broad spectrum of our far-off resonant YAG laser may be driving a two-photon Raman transition which mixes the excited states ${}^2P_{3/2}F' = 1$ with $F' = 2$ or $F' = 2$ with $F' = 3$. If two photons from the YAG laser are produced with an energy difference equal to the level splitting in the atom, a two-photon Raman transition between those levels can occur. Figure 5.8 sketches this process: if the frequency difference between the photons γ_A and γ_B is equal to 267 MHz, the two-photon detuning δ is zero and transitions from $|F' = 2\rangle \rightarrow |e\rangle \rightarrow |F' = 3\rangle$ (and the reverse) are resonant. This resonant transition process leads to mixing of the excited states so that F is no longer a good quantum number and the usual selection rules do not apply. In this instance, the normal laser cooling transition ${}^2S_{1/2}F = 2 \rightarrow {}^2P_{3/2}F' = 3$ could easily decay to $F = 1$. The spurious transition between the ground states would corrupt sub-Doppler cooling.

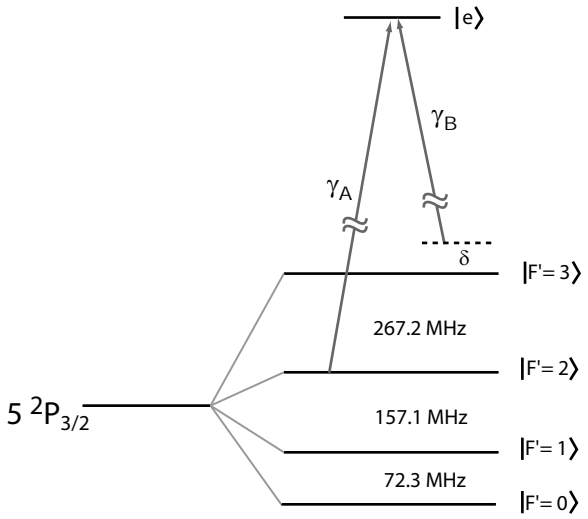

Figure 5.8: Diagram excited-state mixing process.

5.6.1 YAG laser spectrum

To assess the possibility of this effect we sought to characterize the lineshape of our laser. For this purpose a Michaelson interferometer was built to measure the coherence length of the laser. Since the linewidth is likely to depend on the conditions at which the laser is operated, we sought to make the measurement under our usual full-power setting. We used the front-surface reflections off two uncoated glass slides to pick off a small fraction of the output beam and coupled it into the interferometer. A plot of fringe contrast as a function of path-length difference in the interferometer is shown in Figure 5.9. These data are fit to the function e^{-x^2/l_c^2} where x is the path length difference and l_c is the coherence length. Assuming our laser has a Gaussian spectral distribution with a full width at half-maximum of 2δ, the coherence length is related to the spectral width by $l_c = \frac{1}{\sqrt{8\pi}\delta}$. The data are best fit by $l_c = 7.56\ cm$ which corresponds to a laser linewidth of 890 MHz. This is an impressively narrow linewidth for our high-power flashlamp-pumped laser, but it is still far broader than the 500 MHz

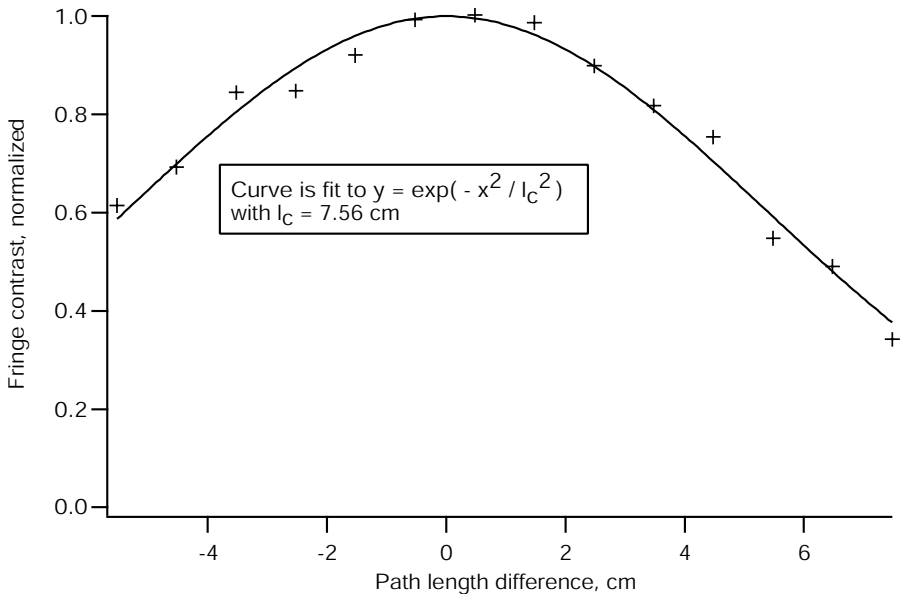

Figure 5.9: Coherence length measurement of YAG laser.

hyperfine splitting of the ${}^2P_{3/2}$ excited state manifold in ${}^{87}Rb$. We conclude that the proposed excited-state mixing effect could indeed be driven by our YAG laser.

To get a better understanding of the laser's spectral output we coupled a small fraction of its output light into a scanning Fabry-Perot spectrometer. The result is seen in Figure 5.10. Just as with the Michealson interferometer measurement, these data were taken with the laser running at full power and after a suitable 10 minute warm-up period. As expected, the spectrum is not a single 890 MHz wide Gaussian peak, but rather consists of narrower peaks spaced by the laser cavity free spectral range and modulated by the 890 MHz wide Gaussian envelope function. This is an important distinction; as can be seen in the figure, a great deal of the output power is generated in two modes separated by approximately 140 MHz. One photon from each of these two modes would have a frequency difference fairly well matched to the 157 MHz splitting between the ${}^2P_{3/2}F' = 2$ and ${}^2P_{3/2}F' = 1$ states. There are also a substantial number

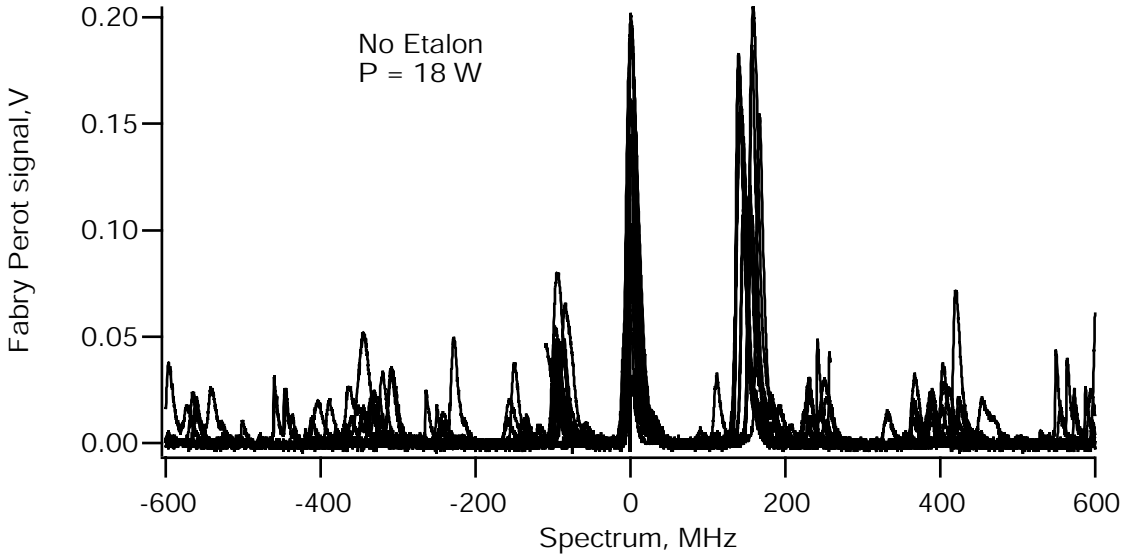

Figure 5.10: Spectrum of YAG laser with no intracavity etalon.

of spectral components separated by twice this value, 280 MHz. The ${}^2P_{3/2}F' = 3$ and ${}^2P_{3/2}F' = 2$ pair of states is responsible for effective sub-Doppler cooling, so we are primarily interested in spectral components separated by their splitting, 267 MHz. We conclude that the probability of a pair of YAG photons driving a Raman transition between these states and mixing the levels is much greater than the 890 MHz linewidth measurement indicates.

We performed a number of experiments with intracavity glass etalons in an attempt to improve the spectrum of the YAG laser. The first etalon was an uncoated glass flat 5 mm thick. This was placed inside the laser cavity on a rotatable stage between the Nd:YAG crystal and the high-reflectivity mirror. It was necessary to tweak the alignment of the laser's pinhole apertures and cavity mirrors to optimize the output power with etalon in place. This is not surprising, given that the etalon changes the optical path length in the cavity and translates the beam slightly. Even with the optimization, we were unable to get more than 15 Watts total output power, compared

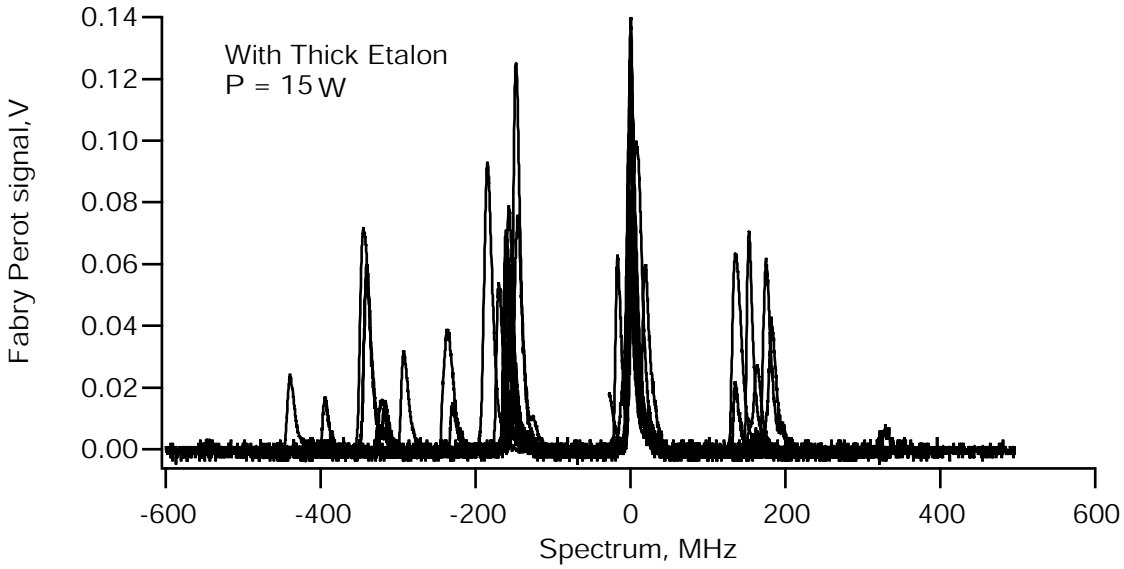

Figure 5.11: Spectrum of YAG laser with the thick intracavity etalon.

to 18 Watts without it. Data from the Fabry-Perot spectrometer with the thick etalon in place is shown in Figure 5.11. The overall envelope is much narrower, as all the power is contained within a 600 MHz bandwidth. The existence of large features separated by 140 MHz remains, however, so it is unlikely that this etalon would substantially reduce excited-state mixing effects.

We also measured the laser output spectrum with a second, thinner etalon in the cavity. This etalon was also an uncoated glass flat, approximately 1 mm thick. Once again it was necessary to optimize the output power by steering the pinhole apertures and the cavity mirrors. The maximum power we could achieve was 13 Watts. The spectrum with both etalons is shown in Figure 5.12. We can see that the spectrum has been cleaned up a great deal by the presence of both etalons, but the central problem remains; the majority of the power is concentrated into modes separated by 140 MHz. This is the longitudinal mode spacing we expect for our 94 cm long laser cavity.

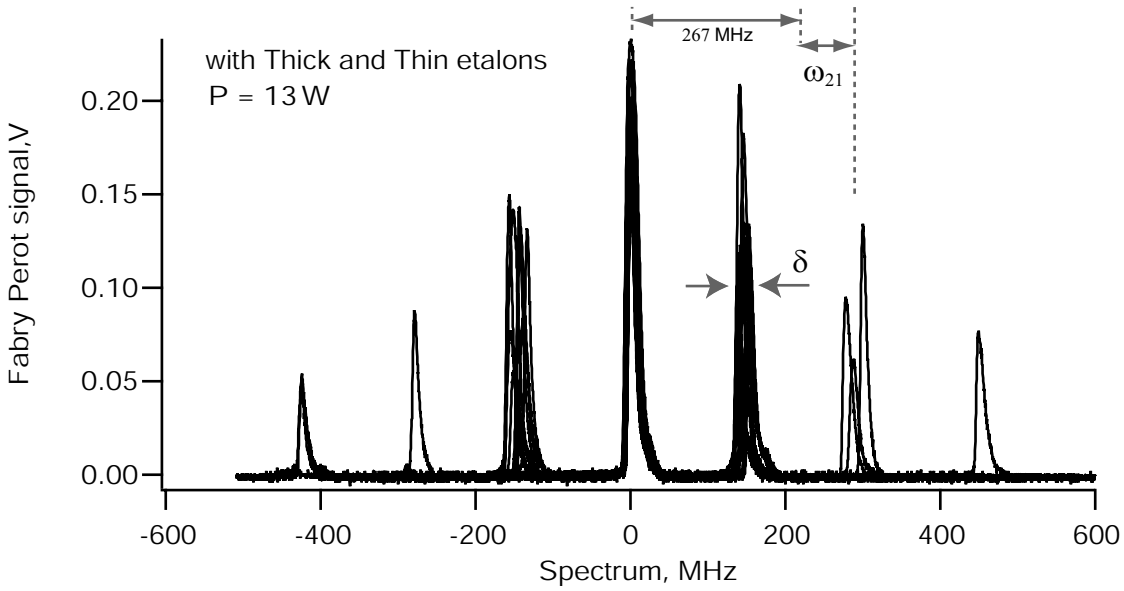

Figure 5.12: Spectrum of YAG laser with thick and thin etalons.

5.6.2 Raman scattering rate estimate

The rate for atoms to undergo a two-photon Raman transition is given by

$$\Gamma_R = \frac{\alpha_1^2\,\varepsilon^4}{8\,\hbar^2\,c^2}\langle 2|\mathbf{S}\cdot\mathbf{s}|1\rangle^2\frac{\delta}{\omega_{21}^2+\delta^2} \tag{5.27}$$

where α_1 is the vector polarizability of the excited state, ε is the electric field of the laser, δ is the spectral width of one of the laser's longitudinal modes, and ω_{21} is the longitudinal mode spacing and the hyperfine level spacing (see note in Figure 5.12). The matrix element $\langle 2|\mathbf{S}\cdot\mathbf{s}|1\rangle$ of the electron spin operator $\mathbf{S}$ is of order unity. We can use our spectral measurements to estimate this Raman scattering rate. The spectral width of each longitudinal mode is approximately $\delta \simeq 30$ MHz, and the spacing between two modes is roughly 280 MHz, so $\omega_{21} \simeq 10$ MHz. Using $\alpha_1 = 100\ \mathring{A}^3$ [Kadar-Kallen and Bonin, 1992], and 6×10^5 W/cm^3 for the peak intensity, we find $\Gamma_R = 2$ MHz.

This transition rate is one-third the natural lifetime of the exited state, 6 MHz. According to this analysis, the probability of an atom which has been exited to the $F' = 3$ upper hyperfine level being transferred to $F' = 2$ is one in three. This indicates a large degree of mixing between the excited states.

5.6.3 Proposed test experiment

We have not performed a measurement to conclusively show that this two-photon Raman excited-state mixing process occurs. We believe that such an experiment is feasible, and describe it here.

We wish to determine whether the presence of the YAG laser mixes the ${}^2P_{3/2}F' = 3$ with the $F' = 2$ state. This could be done by preparing a HAT in the ${}^2S_{1/2}F = 1$ ground state (see Section 4.5) and performing absorption imaging with a probe laser resonant with the ${}^2S_{1/2}F = 1 \rightarrow {}^2 P_{3/2}F' = 3$ transition. Normally this transition is completely forbidden, as it violates the $\Delta F = 0, \pm 1$ selection rule. We would expect atoms in the HAT to be completely transparent to the probe light. However, if the $F' = 2$ and $F' = 3$ are coupled, there is a nonzero probability of absorption since the $F = 1 \rightarrow F' = 2$ transition is allowed. Our procedure would be to image the HAT with $F = 1 \rightarrow F' = 3$ light with the YAG laser on and again just after extinguishing the YAG. If there is a perceptible increase in the number of photons absorbed with the YAG compared to the image with it off, we would conclude that the YAG mixes the two excited states.

One drawback with this plan is that it uses the same pulse of light to pump the transition and to image. The requirements for pumping the $F = 1 \rightarrow F' = 3$ transition (intensity, pulse duration, etc.) are likely to be different from the requirements for imaging (camera must not saturate, etc.). This problem could be overcome with a

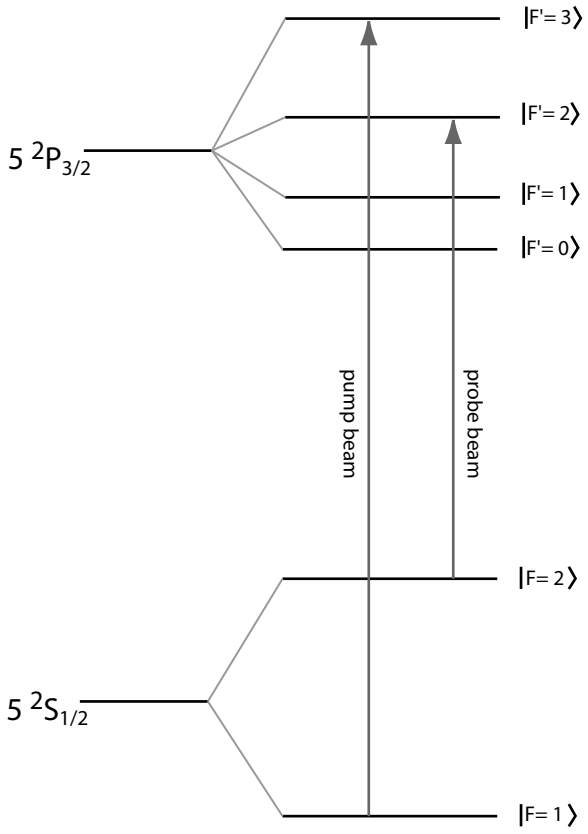

Figure 5.13: Proposed scheme for detecting excited-state mixing.

more refined procedure, sketched in Figure 5.13. Once again we would prepare a HAT with atoms optically pumped into the $F = 1$ ground state and apply a pulse of light resonant with the $F = 1 \rightarrow F' = 3$ transition. This pulse could be made as intense or long-lasting as necessary. We would follow the pump pulse with an imaging probe pulse tuned to the $F = 2 \rightarrow F' = 3$ transition. In the absence of excited-state mixing, the $F = 1 \rightarrow F' = 3$ light does nothing, the atoms stay in the $F = 1$ ground state and the imaging light is not absorbed. If the excited states are mixed by the YAG laser, some atoms are pumped into the $F' = 2$ state by the $F = 1 \rightarrow F' = 3$ pulse, from which they have a 50% probability of decaying to the $F = 2$ ground state and

being detected by the imaging pulse. As above, we would perform this series of pulses with the YAG laser on, and again immediately after turning it off. If the absorption of imaging light is substantially greater with the YAG on, we conclude that excited-state mixing is taking place.

5.6.4 Possible remedies

If this excited-state mixing is an effect which affects the temperature of atoms in our trap, it is clearly important to consider what might be done about it. One possibility is to change the cavity length of our existing YAG laser to move its longitudinal mode spacing further from resonance with allowed excited-state transitions. This is not easily done, however. The best possible mode spacing is halfway between the $F' = 2 \rightarrow F' = 1$ and $F' = 3 \rightarrow F' = 2$ transitions at 212 MHz. This corresponds to a cavity length of 70.7 cm, or 20 cm shorter than its current configuration. The laser's manufacturer, Lee Laser Incorporated, expressed their concern that this cavity length would not permit proper mode-matching with the Nd:YAG crystal rod, and strongly recommends against this modification.

A single-frequency YAG laser with comparable power would be an ideal solution. Such lasers have been demonstrated and described in the literature, the earliest by Nabors *et al.* in 1989 [Nabors *et al.*, 1989]. The authors coupled 40 mW of single-frequency master laser into a high-power ring oscillator slave laser to achieve 13 Watts of single-frequency output power. The master laser was a home-built monolithic non-planar ring oscillator (NPRO) pumped by a laser diode. A commercially available Nd:YAG laser was disassembled and its rod and flashlamp assembly were used as the active medium in the slave laser. A ring configuration was chosen for the slave laser to establish lasing in only one propagation direction for a unidirectional output beam.

This is necessary to ensure that no output power is directed back into the master laser. Since the original description of this technique, higher powers have been reported [Cregut *et al.*, 1989, Golla *et al.*, 1993, Shine *et al.*, 1995, Ottaway *et al.*, 2000]. A new technique employing a similar master laser but using a Ytterbium-doped fiber for the gain medium in the slave laser has recently been reported [Liem *et al.*, 2003]. This apparatus produces an impressive 100 Watt output beam in a pure TEM_{00} mode.

All of these injection-locking systems employ an NPRO master oscillator producing tens of milliwatts or more. Construction of such lasers has been described in the literature [Richards and McInnes, 1995] but is a serious undertaking; in particular the preparation of a cleaved Nd:YAG slab is beyond the means of this laboratory. Suitable single-frequency master lasers are also available commercially [InnoLight, Lightwave], but their expense has thus far ruled out their use in this experiment.

Chapter 6

Forced Evaporation

6.1 Introduction

The process of forced evaporation, in which the intensity of the far-off resonant YAG laser is deliberately decreased to remove the hotter atoms and leave the colder ones in the trap, is discussed in this chapter. We wish to investigate increasing the phase space density in our HAT. Reaching the critical value of 2.61 will achieve Bose-Einstein Condensation.

Conceptually, we view forced evaporative cooling in the HAT as a two-step process. In the first step, we reduce the trap depth by decreasing the YAG laser intensity. The change in the potential energy is made slowly with respect to the atoms' oscillation period in the trap, so that it is adiabatic and conserves the number of atoms and phase space density. In the second step, atoms elastically collide with each other in the trap. Some of these collisions result in an atom with a thermal energy greater than the trap depth, and those atoms are ejected, carrying away a disproportionate amount of energy. The remaining atoms reach a new, lower equilibrium temperature, after which the cycle is repeated. A net gain in phase space density occurs if the loss in atoms and decrease

in oscillation frequency is more than compensated for by the lower temperature.

This type of forced evaporation is different from evaporation in a magnetic trap. In our case, the shape of the potential energy curve is gradually flattened out, so that the oscillation frequency at the center of the trap decreases. In magnetic evaporation the shape of the potential energy curve remains fixed [Anderson *et al.*, 1995, Bradley *et al.*, 1995, Davis *et al.*, 1995a]. High-temperature atoms on the outermost portions of the trap are ejected when a radio-frequency electric field induces a transition to an untrapped state. This has the advantage that the oscillation frequencies at the center remain unchanged throughout the evaporation process. Our optical evaporation is therefore less efficient than evaporation in a magnetic trap; nonetheless, it has the great advantage of experimental simplicity. It begins at higher initial phase space densities than are achievable with magnetic traps. Further, starting densities are higher, so evaporation can be performed much more rapidly. Higher starting densities place less stringent requirements on the background gas pressure; unlike most experiments with magnetic traps, we conduct evaporation in the same vacuum chamber which produced our vapor-loaded MOT.

We begin with a theoretical model presenting a scaling-law analysis of the thermodynamic properties involved in evaporation and their dependence on the trap potential in Section 6.2. Section 6.3 describes a computer model we have created to predict and optimize the phase space density as a function of the decrease in trap depth. The model produces a plot of the trap potential decreasing with time. We have experimented with a number of these potential ramps, and representative data are presented in Section 6.4.

We have increased the phase space density by more than two orders of magnitude in 0.5 seconds. Our best data so far, ≈ 1000 atoms at 100 nK, corresponds to a phase space density of $0.91^{+1.1}_{-0.5}$, a factor of three short of BEC. In Section 6.5, we discuss

the data and conclude that background collisions with hot untrapped atoms in the vacuum chamber limit the evaporation. We propose a figure-of-merit, ξ, which is the ratio of the initial elastic scattering rate to the background collision rate. We find that ξ predicts the suitability of a trap for evaporation to BEC. Our current best starting conditions correspond to $\xi = 1 \times 10^4$. In Section 6.6 we predict that increasing ξ to 3×10^4 would permit evaporation to BEC, and we propose to do this by decreasing the background pressure in our vacuum chamber.

6.2 Theory

Evaporative cooling relies upon the preferential removal of atoms with energy higher than the average energy of the trapped atom cloud. Atoms remaining in the trap reach a new, lower equilibrium temperature as the hotter atoms carry energy away. This process is most easily described by a two-step model, which deals with the ejection of the hotter atoms and the subsequent rethermalization as two separate mechanisms. This description was first put forth in the context of magnetic evaporation by Davis *et al.* [Davis *et al.*, 1995, b] and later developed by Ketterle *et al.* [Ketterle and van Druten, 1996]. As has been pointed out by [O'Hara *et al.*, 2001, Barrett *et al.*, 2001], there are important qualitative differences for optical traps. We present here a simple model of evaporation that suitable for optimization of the evaporation process.

Physically, ejecting hotter atoms is achieved by decreasing the FORT laser intensity and thus decreasing the trap depth; atoms with energies greater than the trap depth escape. Rethermalization occurs as atoms held in the trap collide elastically with one another and reach a new equilibrium temperature. The intimate connection between trap depth and oscillation frequency make evaporation less efficient for optical traps

than for magnetic ones.

6.2.1 Rethermalization

We will first consider the process of rethermalization within the trap. When two atoms elastically collide occasionally one will be left with an energy greater than the trap potential and be ejected. The departing atom carries energy away, leaving the remaining ensemble cooled. We can define two parameters describing this process,

$$\nu = \frac{N'}{N} \tag{6.1}$$

$$\epsilon = \frac{E'}{E} \tag{6.2}$$

where N is the number of atoms in the trap, E is the thermal energy, and the primes denote quantities after the rethermalization step. It is also useful to define η, the ratio of the trap depth to the thermal energy.

$$\eta = \frac{U_0}{k_B\, T} \tag{6.3}$$

This leads to

$$\nu(\eta) = \frac{\int_0^{\eta k_B T}\, g(E)\, e^{\frac{-E}{k_B T}}\, dE}{\int_0^{\infty}\, g(E)\, e^{\frac{-E}{k_B T}}\, dE} \tag{6.4}$$

$$\epsilon(\eta) = \frac{\int_0^{\eta k_B T}\, E\, g(E)\, e^{\frac{-E}{k_B T}}\, dE}{\int_0^{\infty}\, E\, g(E)\, e^{\frac{-E}{k_B T}}\, dE} \tag{6.5}$$

where $g(E)$ is the density of states, which is proportional to E^3 for a three dimensional harmonic trap. After integration we find

$$\nu(\eta) = 1 - \frac{2 + 2\eta + \eta^2}{2e^{\eta}} \tag{6.6}$$

$$\epsilon(\eta) = \frac{1}{3}\left(3 - \frac{6 + 6\eta + 3\eta^2 + \eta^3}{2e^{\eta}}\right) \tag{6.7}$$

All relevant thermodynamic properties can be related to ν and ϵ. The temperature can be found by noting that $E \propto N\,T$, so

$$\frac{T'}{T} = \frac{E'\,N}{E\,N'} = \frac{\epsilon}{\nu} \tag{6.8}$$

Similarly, the peak density of atoms in the trap goes as

$$\frac{n'}{n} = \nu \left(\frac{T}{T'}\right)^{3/2} = \frac{\nu^{5/2}}{\epsilon^{3/2}} \tag{6.9}$$

The atoms rethermalize by elastically colliding with one another, the time τ necessary for thermalization is thus related to the collision rate $\tau \propto 1/(n\,\sigma\,v)$. We therefore find

$$\frac{\tau'}{\tau} = \frac{n}{n'} \left(\frac{T}{T'}\right)^{1/2} = \frac{\epsilon}{\nu^2} \tag{6.10}$$

Finally, the phase space density in the trap is given by

$$\rho = N \left(\frac{\hbar\overline{\omega}}{k_B\,T}\right) \tag{6.11}$$

and therefore scales according to

$$\frac{\rho'}{\rho} = \frac{N'}{N} \left(\frac{T}{T'}\right)^{3} = \frac{\nu^4}{\epsilon^3} \tag{6.12}$$

6.2.2 Decreasing the potential

We wish to decrease the depth of the potential well by decreasing the intensity of the FORT laser. If this is done slowly with respect to the mean trap oscillation period the process is adiabatic and will conserve phase space density ρ and the total number of atoms N. We can define a third parameter of evaporation, the fraction by which the potential is cut in each step:

$$\mu = \frac{U'}{U} \tag{6.13}$$

The mean oscillation frequency $\overline{\omega}$ scales as

$$\frac{\overline{\omega}'}{\overline{\omega}} = \mu^{1/2} \tag{6.14}$$

During an adiabatic decrease in the potential, the quantum number of each atom is unchanged. The total energy in the trap, and thus its temperature, depends on the the quantum number and the oscillation frequency according to $E = 3/2Nk_BT = (n + 1/2)\hbar\overline{\omega}$. Consequently, the temperature scales just like the oscillation frequency.

$$\frac{T'}{T} = \frac{\overline{\omega}'}{\overline{\omega}} = \mu^{1/2} \tag{6.15}$$

Similarly, the peak density scales as

$$\frac{n'}{n} = \left(\frac{T}{T'}\frac{\overline{\omega}'^2}{\overline{\omega}^2}\right)^{3/2} = \mu^{3/4} \tag{6.16}$$

Finally, the rethermalization time depends on the density and the temperature, so

$$\frac{\tau'}{\tau} = \frac{n}{n'}\left(\frac{T}{T'}\right)^{1/2} = \mu^{-1} \tag{6.17}$$

6.2.3 Background collisions

Atoms are lost from the trap during each rethermalization step and also through collisions with untrapped atoms in the background vapor. The loss from background collisions leads to the ≈900 millisecond trap lifetime discussed in Section 4.6.2. This loss is included in our computer model after each iteration by reducing the number of atoms by $exp(-\Gamma_{BG}\ \Delta t) \simeq -\Gamma_{BG}\ \Delta t$, where Δt is the duration of the step, and Γ_{BG} is the reciprocal of the trap lifetime.

6.3 Computer model

We have developed a computer model which uses these scaling relationships to generate an optimized potential ramp and predict the values of these trap parameters throughout the curve. The model works in an iterative process, first reducing the potential by some amount, then waiting for the atoms to rethermalize, then repeating. For each

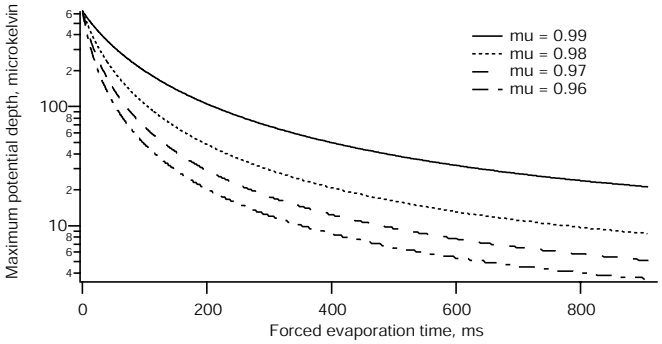

Figure 6.1: Potential depth vs. time for various values of μ.

step it calculates N, n, $\overline{\omega}$, ρ, and τ. It minimizes the loss of atoms by calculating the time necessary for the potential decrease step to be adiabatic (twice the oscillation period), and the time necessary for five collisions in the rethermalization step [Davis *et al.*, 1995, b]. Given the HAT lifetime (section 4.6.2), the model also takes into account atom loss due to background gas collisions.

To illustrate the utility of this model, we consider a ramp in which the potential is decreased by a constant fraction in each step (constant-μ). A series of such curves is shown in Figures 6.1, 6.2, 6.3, and 6.4. All these curves were calculated with the same initial conditions: 18,000 atoms in the center well, 50 μK temperature, $\nu_x = \nu_y = 6.4$ kHz, and a trap lifetime of 850 ms.

It can be seen from the graphs that a more aggressive ramp, with the potential being reduced by 4% in each iteration, results in a lower number of atoms, but also a lower temperature which leads to a higher phase space density. Given the initial conditions the ramps predict a final phase space density of about 0.5; the highest achievable with these starting conditions is below 0.9 with a very aggressive $\mu = 0.80$ ramp.

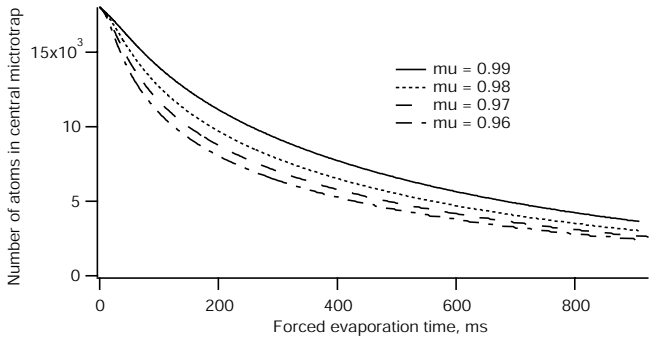

Figure 6.2: Number of atoms vs. time for various values of μ.

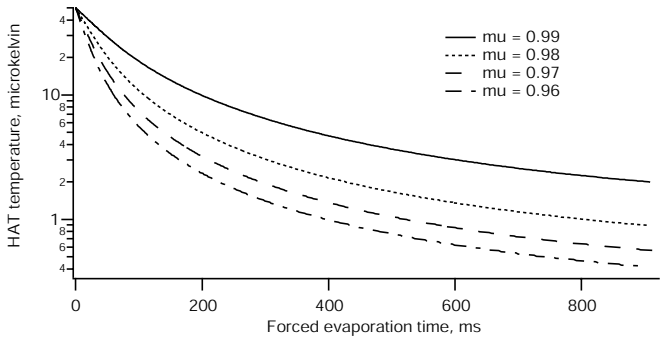

Figure 6.3: Temperature vs. time for various values of μ.

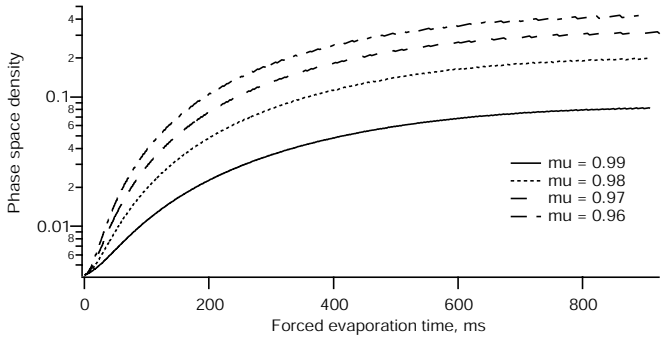

Figure 6.4: Phase space density vs. time for various values of μ.

6.4 Experimental results

We have performed evaporative cooling on our HAT using a number of different potential ramps. Some, such as the constant-μ ramp shown above are amenable to analysis with our computer model and we can predict the number of atoms and phase space density in the trap as the potential is decreased. Others, such as the linear ramp and the pure exponential ramp are more difficult to analyze, and were attempted on a try-it-and-see basis.

6.4.1 Uncertainty in phase space density

Measurement of the phase space density at the end of a potential ramp is complicated by two factors: uncertainty in the center-well fraction, and uncertainty in the potential.

As discussed in Section 4.6, we measure the total number of atoms in a Talbot fringe and measure the fraction of those in the center well to calculate the number in the center. Measuring the center-well fraction is not difficult when the total number is large, but late into these evaporation ramps the total number is small and the signal-to-noise ratio makes measurement of the center-well fraction difficult. Even though we do not expect atoms to redistribute among the microtraps (see Section 6.4.3), we do expect the center-well fraction to change during forced evaporation. This is because the potential ramp, whether constant-μ or constant-η, is optimized for the initial conditions of the center well. Outer microtraps start with smaller potential depths and fewer atoms, so they have lower collision rates and longer rethermalization times. Consequently, our applied potential ramp is too rapid for the outer traps and they lose a larger fraction of their initial number than will the center trap. This has been seen in our experiments and modelled by computer. Prior to evaporation we typically see each Talbot fringe containing 6×6 microtraps, with 3% of the atoms

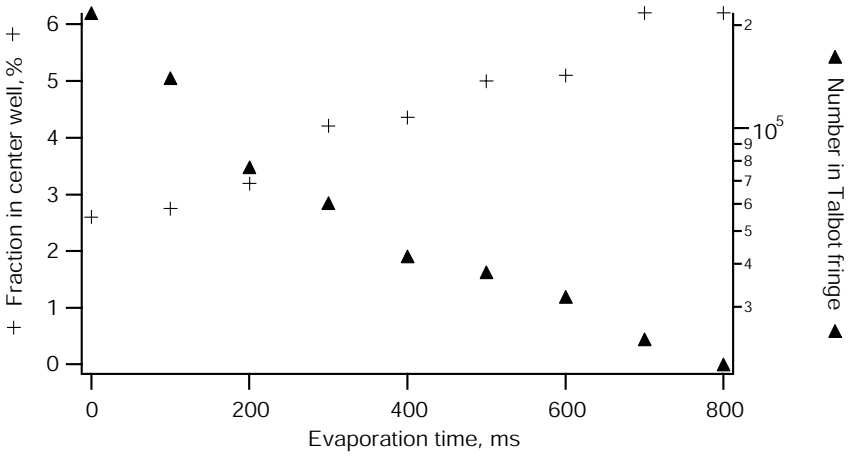

Figure 6.5: Center well fraction (left) and total in a Talbot fringe (right) vs. time.

in a Talbot fringe in the centermost microtrap. A representative data set is seen in Figure 6.5; the center well atom fraction increases (left axis) as the total number in the Talbot fringe decreases (right axis). Given the difficulty encountered in measuring the center well fraction when the number per Talbot fringe falls below ~ 5000, we believe the center well fraction rises to $9.5\% \pm 2\%$ at the end of evaporation.

The other large source of uncertainty in the phase space density is the exact value of the potential depth just prior to releasing the trap and measuring the temperature. We measure the intensity of the YAG laser by recording the voltage on the monitor photodiode in our noise-eater system (Section 4.4.3). Just prior to measuring the temperature at the end of a ramp, this voltage is typically under 10 millivolts. The difficulty arises from various millivolt-size variations and offsets in our circuitry. The analog output channels on the multi-function data acquisition card, for example, routinely develop a 5 mV offset from ground. The two input stages of the differential amplifier which generates the reference voltage are also prone to offsets, and need to be trimmed to ensure that input stages are balanced. Finally, the presence of electronic

noise must be closely monitored- we have found that several millivolts of 60 Hz noise will appear depending on the position of the differential amplifier in the room. Given these sources of errors, we assign $\pm$ 5 mV of uncertainty to our voltage measurements. Thus a measurement of 10 ± 5 mV corresponds to a mean trap oscillation frequency of 243^{+55}_{-71} Hz.

This 30% uncertainty leads to a considerable uncertainty in the final phase space density, since phase space density depends on the cube of the oscillation frequency. We conclude that our measurements of phase space density at the end of a potential ramp are accurate to within a factor of two.

6.4.2 Constant-μ ramp

Figures 6.6 through 6.8 show our model predictions and results for a $\mu = 0.983$ ramp. The temperature measurements agree quite well with the expected values. There is more noise on the number measurements, this is because these data were taken with the Spatial Heterodyne imaging system. To measure the number of atoms we fit the image to gaussian peaks and calculated the area under curve given its waist and amplitude. The waist measurements were prone to noise in the images, particularly late in the evaporation when the signal size was small. Nonetheless, we can see reasonably good agreement with the model predictions. Naturally the scatter in the number measurements translates into scatter in the phase space density measurements. Even so, we can see that the predicted final phase space density of 0.6 is in reasonably good agreement with our measurement.

Several other constant-μ evaporation data sets were taken with similar results; our model appears to predict the temperature, number of atoms, and phase space density fairly well.

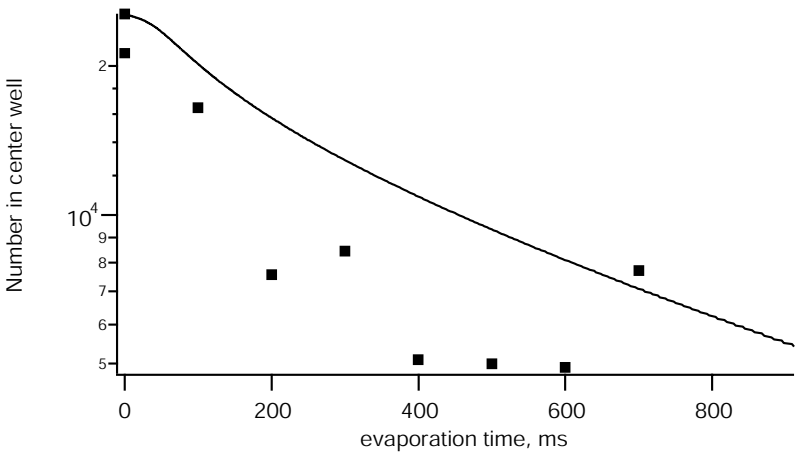

Figure 6.6: Measured number of atoms vs. time for $\mu = 0.983$.

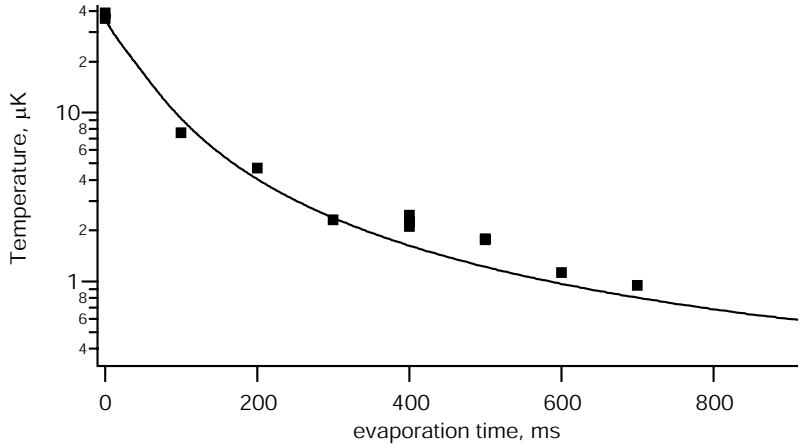

Figure 6.7: Measured temperature vs. time for $\mu = 0.983$.

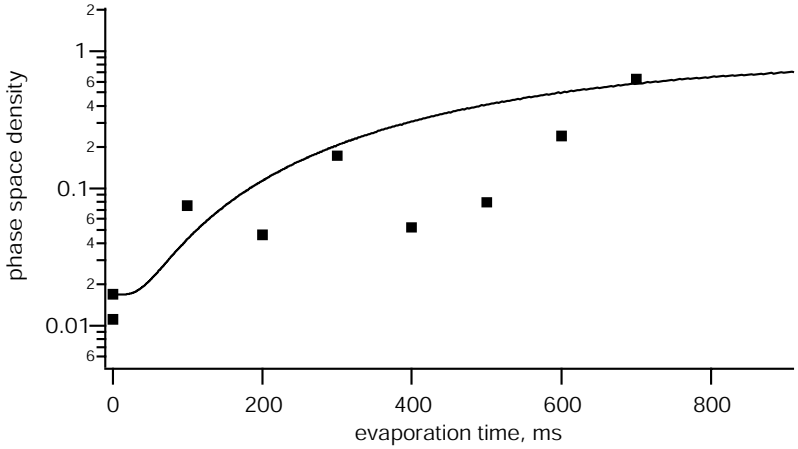

Figure 6.8: Measured phase space density vs. time for $\mu = 0.983$.

6.4.3 Constant-μ ramp with redistribution

Our original model for forced evaporation in the HAT included a subroutine to simulate the movement of atoms from one microtrap to another. Since the trap depth does not rise all the way to zero potential energy in the interstices between the microtraps, we thought it would be possible for atoms to jump from outer microtraps into the center one as the potential depth is decreased. For each step in the evaporation our model calculated the number of atoms with a thermal energy low enough to remain trapped in the HAT, but large enough to jump into a neighboring microtrap.

We eventually abandoned this model of forced evaporation in the HAT, as we believe that redistribution between the wells is extremely unlikely. For an atom to be transferred from one microtrap to another, it must elastically scatter with an atom in the original microtrap and be left with a suitable kinetic energy. It must then travel to the second microtrap and make a second elastic collision with a trapped atom there. Since two collisions are necessary, redistribution depends on the probability of making a second collision. We can calculate this probability with the collisional opacity of the

microtrap: the density of atoms n times the collision cross section σ_c times the width of the trap l.

At atom which leaves a microtrap travelling along the x- or y- directions will approach neighboring microtraps along their skinny direction. At 50 μK, the thermal waist of the microtrap in the x- and y- directions is roughly 1.2 μm. If we say the average density in a microtrap is $n = 10^{13}$ cm^{-3} and we use the elastic-collision cross section $\sigma_c = 4.8 \times 10^{-12}$ cm^2, we find a collisional opacity of 0.006. This means that an atom which leaves the center of one microtrap headed directly for the center of a neighboring trap has only a one in 150 chance of making a collision and staying there.

Redistribution is a bit more likely among the z-direction: the thermal width of the microtraps in their long axis is roughly 50 μm, so the the collisional opacity is 0.25. Thus there is roughly a one-in-four chance that an atom which leaves one microtrap headed for the corresponding microtrap in the neighboring Talbot fringe will make a collision stay there. Redistribution among adjacent Talbot fringes is of little interest, however, since neighboring Talbot fringes have roughly the same potential energy. It is only the improbable transitions in the x- and y- directions which transfer atoms into the center microtrap and increase the peak density.

A data set taken with $\mu = 0.995$ is seen in Figures 6.9 through 6.11. The temperature measurements tend to be below the predictions and the atom loss appears to be greater than predicted, but these two effects largely counteract each other in the phase space calculation. The final phase space density, 0.63, is above the predicted 0.37.

6.4.4 Accelerated ramp

We have also considered a variation on the constant-μ ramp which uses a different method to calculate the adiabatic condition. As described above, our standard

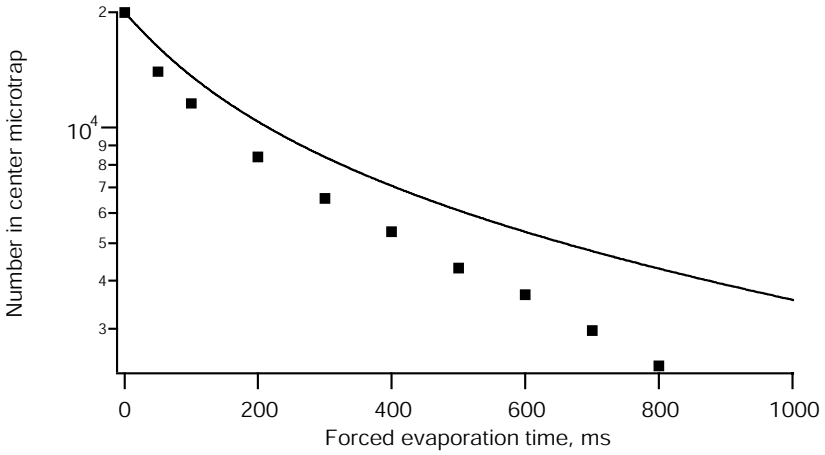

Figure 6.9: Measured number of atoms vs. time for $\mu = 0.995$ with redistribution.

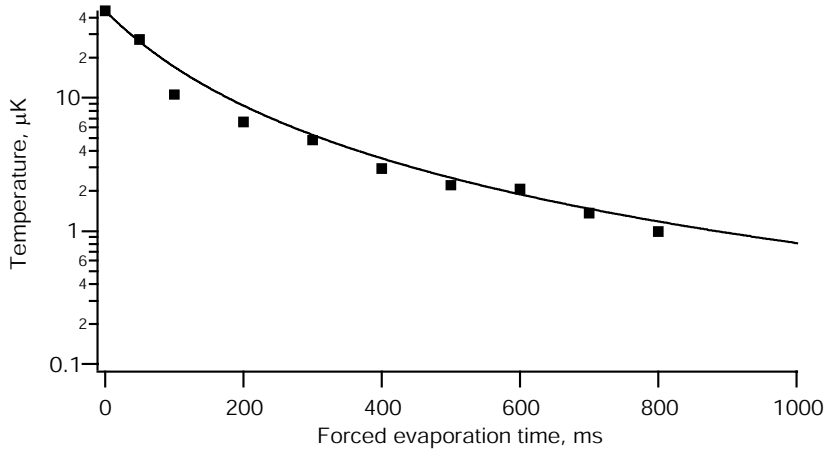

Figure 6.10: Measured temperature vs. time for $\mu = 0.995$ with redistribution.

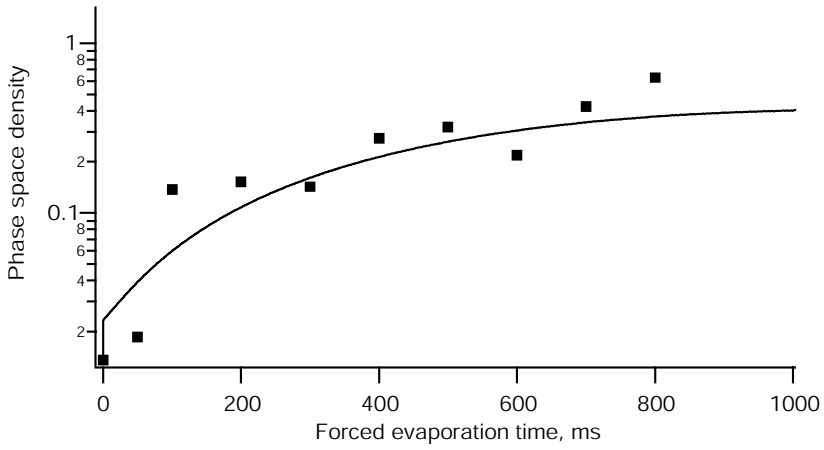

Figure 6.11: Measured phase space density vs. time for $\mu = 0.995$ with redistribution.

constant-μ ramp decreases the potential by a fixed fraction, then ensures that the decrease is adiabatic by waiting twice the oscillation period in the trap before decreasing the potential again. We consider the possibility that this adiabatic condition is too strict. Since the potential is changed by a set fraction each time, the changes are increasingly small as the ramp progresses and it may not be necessary to wait two oscillation periods. Our accelerated criterion for adiabaticity is to wait an amount of time corresponding to $10\Delta\omega/\omega^2$. This criterion decreases the oscillation frequency in the trap by a set fraction each time, instead of decreasing the potential by a set fraction. Since the trap oscillation frequency ω scales as the square root of the potential, this length of time scales differently from our normal $2/\omega$ waiting time. The result is a potential ramp which decreases more quickly at the beginning and more slowly at the end than our standard ramp. A representative data set using this accelerated ramp with $\mu = 0.98$ is seen in Figures 6.12 through 6.14. The temperature predictions agree well with our measurements, but the loss rate from the trap is higher than predicted. We have consistently seen that atom loss during these accelerated ramps is unusually

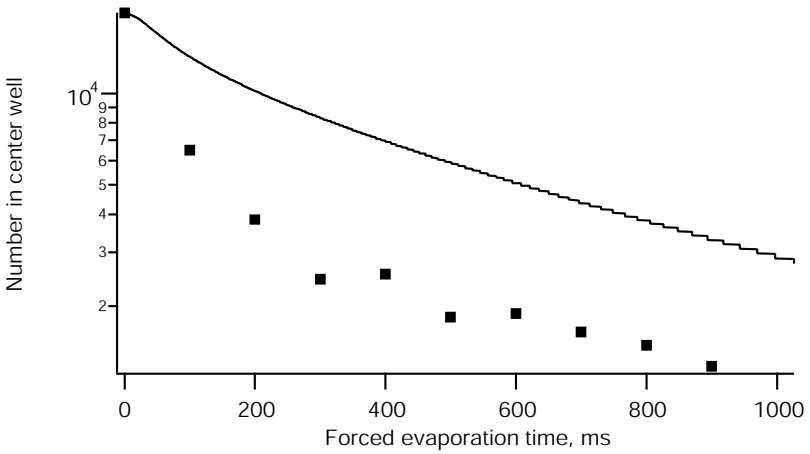

Figure 6.12: Measured number of atoms vs. time for an accelerated $\mu = 0.98$ ramp.

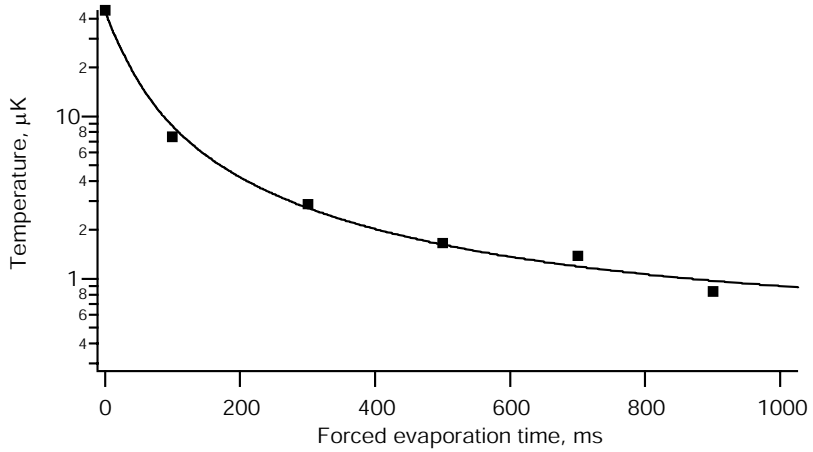

Figure 6.13: Measured temperature vs. time for an accelerated $\mu = 0.98$ ramp.

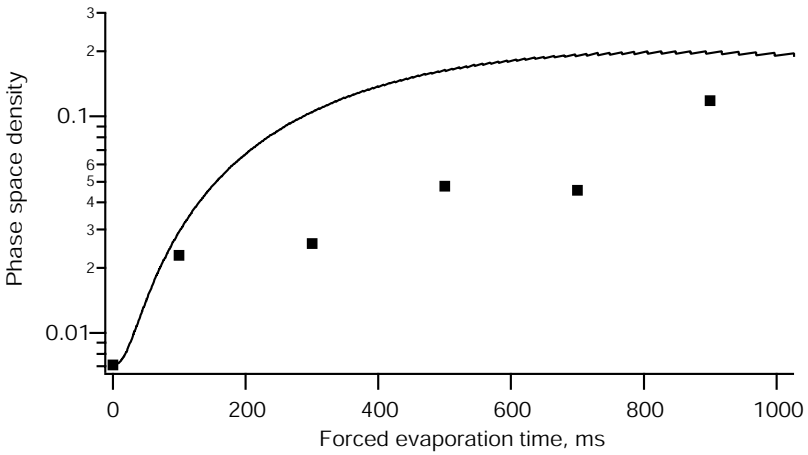

Figure 6.14: Measured phase space density vs. time for an accelerated $\mu = 0.98$ ramp.

high, and conclude that it is better to wait two oscillation periods after reducing the potential.

6.4.5 Constant-η ramp

By taking a slightly different model of atom loss during forced evaporation, O'Hara *et al.* present a different optimized potential ramp [O'Hara *et al.*, 2001]. Their model proposes that atoms will be ejected from the trap such that the remaining thermal energy is a fixed fraction of the well depth. The Boltzmann transport equations are used to calculate the atom loss necessary to meet this condition. The value at which the ratio $\eta = U/T$ is fixed is determined by the tail of the thermal distribution and is very near 10. Given the initial potential depth, number of atoms, and temperature, this model calculates an optimized potential ramp at constant η. We conducted several experiments with η values between 9 and 11, representative data are shown in Figures 6.15 through 6.17. Our temperature measurements agree with predictions fairly well, but atom loss rate is slightly greater than expected. This results in a phase space

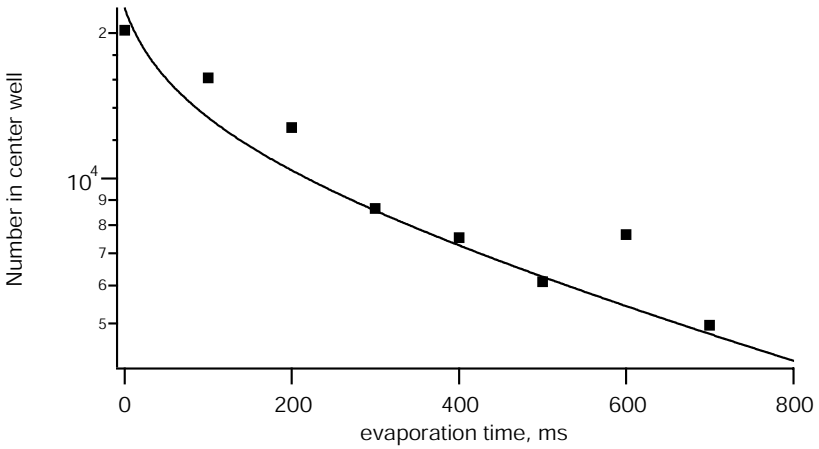

Figure 6.15: Measured number of atoms vs. time for $\eta = 10$.

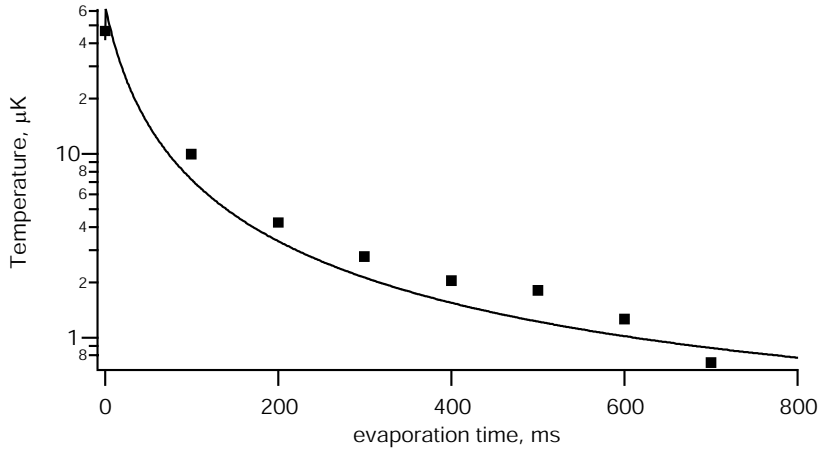

Figure 6.16: Measured temperature vs. time for $\eta = 10$.

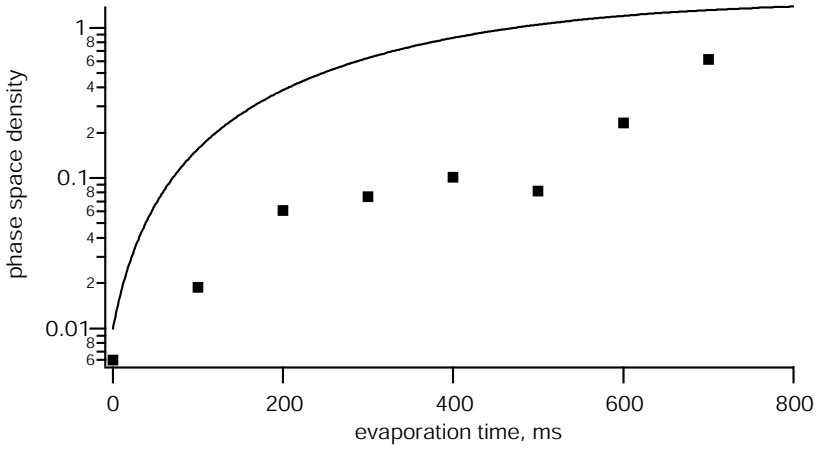

Figure 6.17: Measured phase space density vs. time for $\eta = 10$.

density of 0.60 instead of the anticipated 1.31.

6.4.6 Linear ramp

Rather than rely on models to predict the best evaporation path, we decided to try a potential ramp which we optimize "by hand" in a series of linear steps. This method has the advantage that we can be reasonably confident the resulting ramp is ideal for our starting conditions. A disadvantage is that our computer model is not currently equipped to predict the number of atoms and final phase space density given an arbitrary potential ramp.

We divided the total dynamic range of our potential into four segments, the first from U_{max} to $U_{max}/2$ the second from $U_{max}/2$ to $U_{max}/4$ and so forth until the final segment, which ends at the smallest voltage accessible by our analog output card (see Section 4.4.3).

Each segment is optimized by picking a $\Delta U/\Delta t$ slope and performing forced evaporation down to the minimum of that segment. We then hold the potential at that

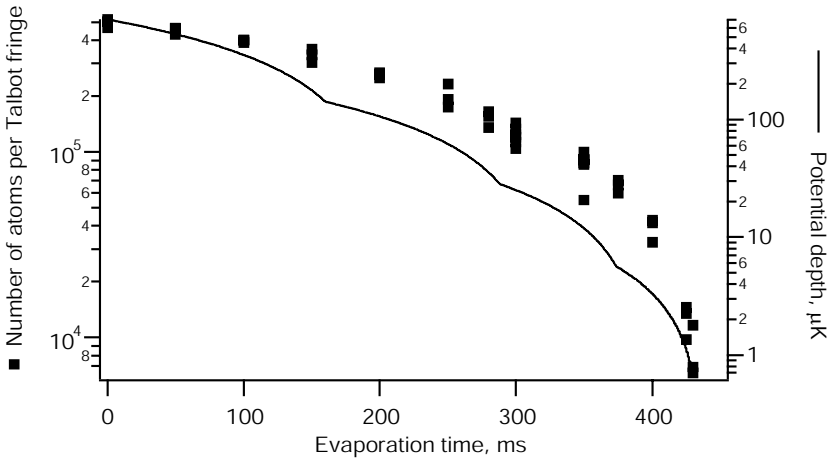

Figure 6.18: Number of atoms vs. time for optimized four-piece linear ramp.

value for about 20 milliseconds to be certain that any ejected atoms have left the field of view, and take an image. We vary the slope to maximize the number of atoms remaining. We did not take the temperature at the end of each ramp, as we have seen that the temperature is consistently 1/10th the trap depth. We start by optimizing the first segment, find the best slope, then use slope to optimize the second segment, and so forth. In this manner we found that the four slopes -3.52 μK/msec, -0.88 μK/msec, -0.26 μK/msec, and -0.088 μK/msec resulted in the highest final number of atoms in the trap. A plot of the atom loss for this piecewise-optimized ramp is seen in Figure 6.18. The number of atoms are scaled on the left axis, and the trap depth is scaled on the right axis.

Two temperature measurements performed at the very end of this ramp yielded the remarkable values 99 ± 10 nK and 113 ± 14 nK. The voltage on the YAG monitor photodiode was 7.9 ± 5 mV at the end of this ramp, corresponding to a mean trap oscillation frequency of 216^{+60}_{-85} Hz. Combining our number, power, and temperature measurements, we find a final phase space density of $0.91^{+1.1}_{-0.5}$. It is important to note

that large uncertainty attached to this measurement arises primarily from systematic errors (voltage offset in the photodiode), not random variations. Thus we conclude that we have measured a phase space density of 0.91, but the actual value could be different by a factor of two in either direction.

6.4.7 Exponential and linear-exponential ramps

Upon examining Figure 6.18 we noticed that atoms are ejected more quickly at the end of the ramp than at the beginning; during the final segment of the ramp the number per Talbot fringe falls from 40,000 to $<$ 10,000 in only 40 milliseconds. This led us to suspect this ramp was still too fast at the very end, and a ramp with an exponential tail might be preferable.

We generated a series of ramps whose final segment decreased exponentially according to $U(t) = U_0 exp(t/\tau)$ with various values of the time constant τ. A graph showing the final 500 milliseconds of these potential curves and the number of atoms measured throughout each is seen in Figure 6.19

For comparison, the exponential curve with the 125 ms time-constant has the same initial slope as our 0.088 $\mu K/ms$ final linear segment. At 400 ms into the linear ramp, 6000 atoms are left at a trap depth of 2.94 μK. The ramp with the exponential end has 6500 atoms left at 600 ms, with a trap depth of 2.71 μK. Though we have not measured the temperature for these data points, we may reasonably assume that it is one tenth the trap depth, as for all our other measurements. In that case, the phase space density for these two points is 0.20 for the linear-end ramp, and 0.25 for the exponential-end ramp. Final phase space densities for all the ramps shown, assuming temperatures of one tenth the trap depth, range from 0.15 to 0.30. Although the ramps with exponential ends do keep atoms in the trap for longer periods of time, they

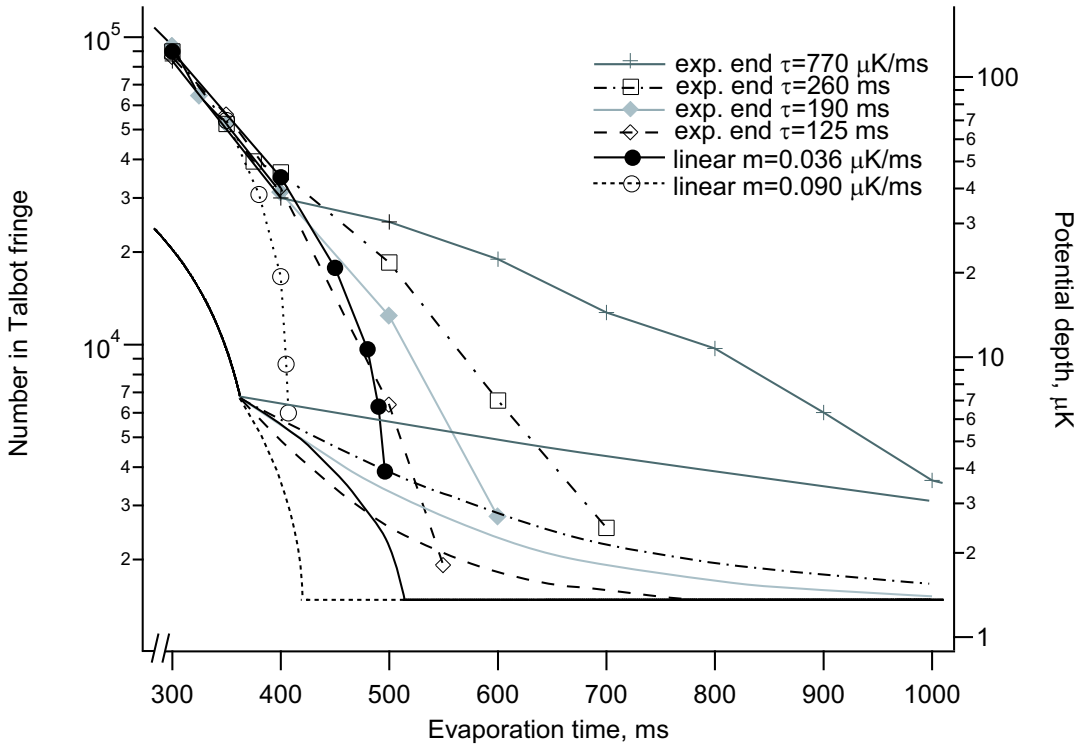

Figure 6.19: Number of atoms per Talbot fringe (left) and trap depth (right) vs. time for a number of exponential-end ramps.

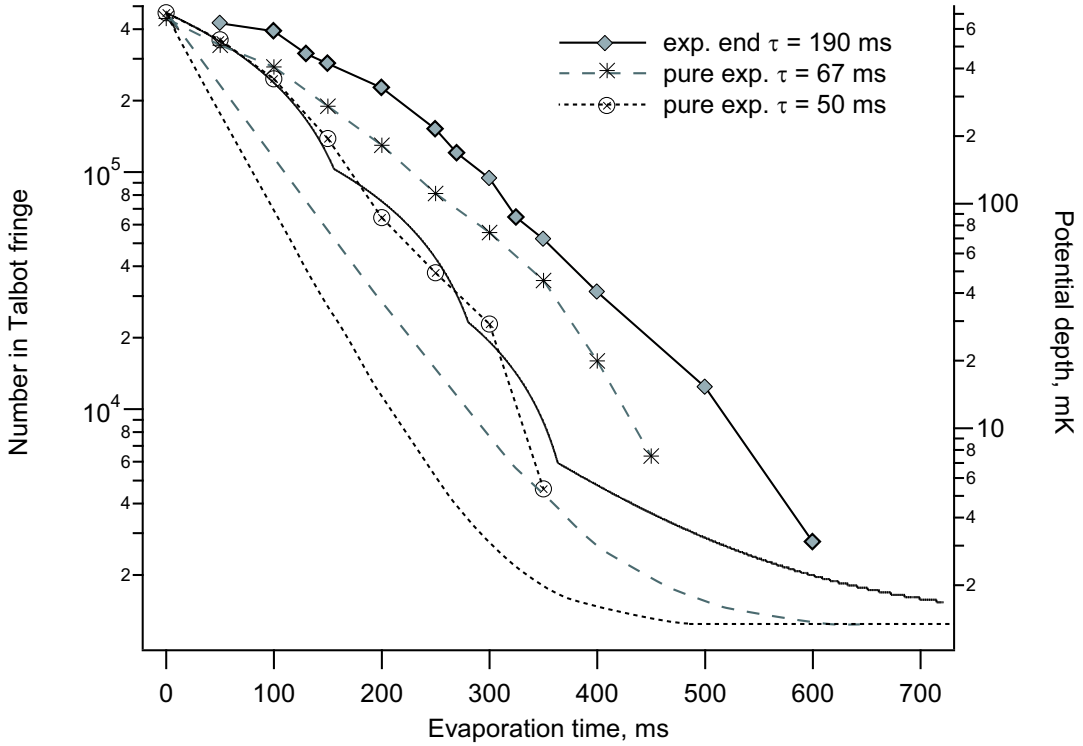

Figure 6.20: Number of atoms per Talbot fringe (left) and trap depth (right) vs. time for two purely exponential ramps and an exponential-end ramp.

ultimately offer only slight improvements on final phase space density.

We also collected forced evaporation data with two potential ramps using purely exponential curves, seen in Figure 6.20. For comparison, the data for the $\tau = 190$ ms exponential-ended ramp is included in the figure. Once again we found that the slower of the two pure exponential ramps lost fewer atoms, but there is little improvement in final phase space density, as the higher number of atoms are at higher temperatures.

6.5 Discussion

Despite their various differences, it seems that the phase space density achieved by different ramps is nearly the same. For our initial conditions, the computer model has not predicted, nor have experiments found a potential ramp which is slow enough to evaporate without ejecting too many atoms but fast enough to avoid excessive losses from background collisions.

This suggests that we define a figure of merit for the initial conditions in the HAT which determines its suitability for evaporation. The best such figure of merit is the ratio of rate of elastic collisions between atoms in the trap Γ_{col} to the rate of collisions with hot untrapped background atoms Γ_{BG}. A large elastic collision rate allows for short rethermalization times and evaporation can proceed quickly, a smaller elastic collision rate requires a more gradual ramp. Conversely, a large background collision rate favors a faster ramp, and a smaller background rate will allow a more gradual one. Thus the elastic scattering rate and the background collision rate are in competition with each other, and their ratio is a useful figure of merit, which we will call ξ.

For our current starting conditions, $\Gamma_{col} = 1.1 \times 10^4\ s^{-1}$, and $\Gamma_{BG} = 1.1\ s^{-1}$, for a figure of merit $\xi = 1.0 \times 10^4$

6.6 Current and future efforts

It is natural to ask how our experiments might be altered to improve the final phase space density and reach the conditions for condensation. For this purpose we use the figure of merit for starting conditions, the ratio of the elastic collision rate to the background scattering rate.

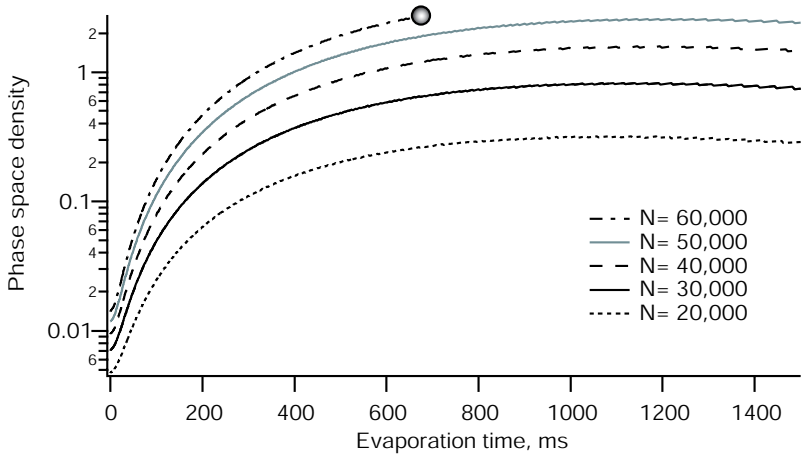

Figure 6.21: Predicted phase space density vs. time for different initial N.

6.6.1 Increase initial N

It is easy to imagine that starting with more atoms in the center microtrap would improve our final phase space density, and this is certainly so. Figure 6.21 shows optimized constant-μ ramps for various values of the initial number of atoms in the center microtrap. All other parameters, such as trap depth, oscillation frequency, and background collision rate are held at our typical values. Our typical initial number, 18,000, reaches a maximum phase space density of 0.32. Further evaporation is not helpful, as losses due to background collisions outpace gains from further reductions in the potential. Doubling the number of atoms in the trap to 40,000 would increase the final space density more than a factor of five. The gain is more than linear, because having more atoms not only increases the density, but also the rethermalization rate in the trap, so evaporation can progress more rapidly and background collisions are less costly. Nonetheless, our model predicts that we would need to triple our starting number of atoms to achieve BEC with all other conditions as they are currently.

By increasing the initial number by a factor of three, we would triple the elastic

collision rate. Consequently for this case $\Gamma_{col} = 3.3 \times 10^4\ s^{-1}$, and $\Gamma_{BG} = 1.1\ s^{-1}$, for a figure of merit $\xi = 3.3 \times 10^4$

Unfortunately, we believe we have reached a limit on the initial density of atoms in the HAT. Since the HAT is loaded from a MOT, its initial average density cannot be much greater than the average density in the MOT. If we approximate one Talbot fringe as an 100 μm $\times$ 100 μm $\times$ 100 μm volume, and say that it contains 500,000 atoms, we find that the average density in the HAT is $\approx 5 \times 10^{11}$ cm^{-3}. This is roughly the highest density achievable in a MOT: radiation pressure prohibits further increase (see Section 3.2.2). Since we cannot increase the density of atoms in the initial MOT, we cannot increase the average density in the HAT.

6.6.2 Increase lifetime

A more straightforward modification to our experiment is the reduction of the background pressure in the vacuum chamber. The loss rate from collisions with untrapped background atoms has been essentially fixed throughout all these experiments. Our 900 millisecond HAT lifetime limits our forced evaporation curves to a few hundred milliseconds in duration. With a lower background collision rate, however, it is possible to evaporate more gradually, and thus more efficiently. Figure 6.22 shows $\mu = 0.98$ potential ramps with various values of the background collision rate, Γ_{bg}. All other variables are held at our current experimental conditions, including N = 18,000 atoms in the center microtrap. The lowest line corresponds to our current conditions, $1/\Gamma_{bg} =$ 900 msec. Note that in each case the phase space density rolls off once the forced evaporation proceeds past the lifetime of the the HAT. With a HAT lifetime of 3 seconds our current starting conditions lead to BEC after 2.6 seconds of evaporation.

Clearly, decreasing the background collision rate by a factor of three would increase

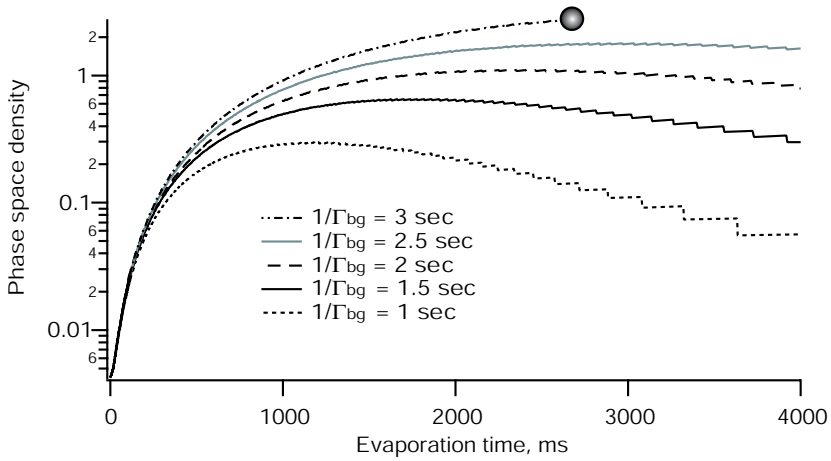

Figure 6.22: Predicted phase space density vs. time for different background collision rates.

our figure of merit by the same factor: $\Gamma_{col} = 1.1 \times 10^4\ s^{-1}$, and $\Gamma_{BG} = 0.33\ s^{-1}$, for a figure of merit $\xi = 3.3 \times 10^4$.

The comparison of these two approaches demonstrates the utility of the ratio ξ. Regardless of how a trap with $\xi = 33,000$ was made, it can be evaporated to BEC.

6.6.3 Current efforts

We believe that a reduction in the background pressure represents our best chance for evaporation to BEC. A factor of three reduction should be well within the means of our vacuum equipment. As of this writing, the ion pump has been replaced and a residual gas analyzer has been installed on our vacuum system. We plan to perform forced evaporation over longer time periods and assess our prediction that BEC is achievable in two to three seconds.

Chapter 7

Summary and conclusion

This section concludes the dissertation with a summary of the major experimental results and our outlook for the future.

A new non-destructive imaging system has been developed and characterized. Spatial Heterodyne Imaging measures the phase shift accumulated by a probe beam as it passes through a cloud of trapped atoms. This imaging system can generate images with high signal-to-noise ratios while scattering as few as 0.0004 photons per atom. This very low scattering rate suggests that Spatial Heterodyne imaging is ideally suited for situations in which one wishes to interrogate an atom cloud several times without generating heating.

This dissertation has described the development and characterization of a Holographic Atom Trap. This trap, or HAT, employs a novel configuration of far-off resonant laser beams to create a periodic array of small potential wells. These wells, or microtraps, typically measure $10\mu m \times 10\mu m \times 100\mu m$ and confine up to 18,000 atoms each at temperatures near 50 microkelvin. The very high oscillation frequencies within the microtraps ($\overline{\nu}$= 18.4 kHz) lead to high atomic densities ($> 10^{14}$ cm^{-3}) and a phase space density greater than 1/260. This periodic array of small, high density samples is

attractive for a number of experiments, in particular for studies of ultracold Rydberg atoms.

We have seen that laser cooling is inhibited in the HAT. The temperature remains fixed at one-tenth the trap depth; evaporation is the dominant temperature-setting mechanism. The inhibition of laser cooling is believed to be related to an excited-state mixing process driven by multiple longitudinal modes in our Nd:YAG laser. A test experiment to study this effect and possible remedies have been presented,.

Finally, this dissertation describes a number of forced evaporation experiments performed with the HAT. A computer model which simulates and optimizes the evaporation process has been created, and its predictions have largely agreed with our experimental results. We have been able to evaporatively cool atoms in the HAT to 100 nanoKelvin, and a phase space density of $0.91^{+1.1}_{-0.5}$, only a factor of three below the requirement for BEC. We have found that the limitation to further increases in phase space density is the rate of collisions with untrapped atoms in the vacuum chamber. Efforts are now underway to reduce the background pressure in our vacuum chamber and evaporate to Bose-Einstein Condensation.

Bibliography

[Bose, 1924] S. N. Bose, Z. Phys. Vol. 26, P. 128, 1924

[Einstein, 1924] A. Einstein, Sitzungsber. Kgl. Preuss. Akad. Wiss., Vol. 1924, P. 261, 1924

[Kadlecek *et al.*, 2001] S. Kadlecek, J. Sebby, R. Newell, and T. G. Walker, "Nondestructive spatial heterodyne imaging of cold atoms", Opt. Lett. Vol. 26, P. 137, 2001

[Newell *et al.*, 2003] R. Newell, J. Sebby, and T. G. Walker, "Dense atom clouds in a Holographic Atom Trap", Opt. Lett. Vol. 28, Iss. 14, P. 1266, 2003

[Anderson *et al.*, 1995] M. H. Anderson, J. Ensher, M. Matthews, C. Wieman, and E. Cornell, "Observation of Bose-Einstein Condensation in a dilute atomic vapor", Science, Vol. 269, P. 198, 1995.

[Bradley *et al.*, 1995] C. C. Bradley, C. A. Sackett, J. J. Tollett, and R. G. Hulet, "Evidence of Bose-Einstein Condensation in an atomic gas with attractive interactions" Phys. Rev. Lett. Vol. 75, 1687, 1995

[Saffman and Walker, 2002] M. Saffman and T. G. Walker, "Creating single-atom and single-photon sources from entangled atomic ensembles", Phys. Rev. A, Vol. 66, 065403. 2002

[Lukin *et al.*, 2001] M. D. Lukin, M. Fleischhauer, R. Cote, L. M. Duan, D. Jaksch, J. I. Cirac, and P. Zoller, "Dipole blockade and quantum information processing in mesoscopic atomic ensembles", Phys. Rev. Lett., Vol. 87, P. 037901, 2001

[Davis *et al.*, 1995a] K. Davis, M. Mewes, M. Andrews, N. van Druten, D. Durfee, D. Kurn, and W. Ketterle, "Bose-Einstein Condensation in a gas of sodium atoms" Phys. Rev. Lett. Vol. 75, 3969, 1995.

[Walker *et al.*, 1990] T. G. Walker, D. Sesko, and C. Wieman, "Collective behavior of optically trapped neutral atoms", Phys. Rev. Lett. Vol. 64, P. 408, 1990

[Ketterle *et al.*, 1993] W. Ketterle, K. B. Davis, M. A. Joffe, A. Martin, and D. E. Pritchard, "High densities of cold atoms in a dark spontaneous force optical trap", Phys. Rev. Lett., Vol. 70, P. 2253, 1993.

[Barrett *et al.*, 2001] M. D. Barrett, J. A. Sauer, and M. S. Chapman, "All-optical formation of an atomic Bose-Einstein condensate", Phys. Rev. Lett. Vol 70, No. 1, p. 010404, July 2001

[Lancaster *et al.*, 2000] G. P. T. Lancaster, W. Sibbett, and K. Dholakia "An extended-cavity diode laser with a circular output beam" Review of Scientific Instruments Vol 71 No 10 Oct 2000

[Andrews *et al.*, 1997] M. R. Andrews, D. M. Kurn, H. J. Miesner, D. S. Durfee, C. G. Townsend, S. Inouye, and W. Ketterle, "Propogation of sound in a Bose-Einstein condensate", Physical Review Letters 79, 553, 1997

[Andrews *et al.*, 1996] M. R. Andrews, M.-O. Mewes, N. J. van Druten, D. S. Durfee, D. M. Kurn, and W. Ketterle, "Direct, Non-destructive observation of a Bose condensate", Science Vol. 273, pp 84 - 87 Jul 1996

[Hecht, 1987] E. Hecht, "Optics", second edition, Addison-Wesley 1987

[Bradley *et al.*, 1997] C. C. Bradley, C. A. Sackett, and R. G. Hulet, "Bose-Einstein condensation of Lithium: Observation of limited condensate number", Physical Review Letters, Vol 78 No 6 pp 985-989 Feb 1997

[Chu *et al.*, 1985] , Steven Chu, L. Hollberg, J. E. Bjorkholm, Alex Cable, and A. Ashkin, "Three dimensional viscous confinement and cooling of atoms by resonance radiation pressure", Phys. Rev. Lett. Vol. 55 No. 1, pp 48-51, July 1985

[Foot, 1991] C. J. Foot, "Laser cooling and trapping of atoms, Contemporary Physics", 32 (6), Nov.-Dec. 19991, pp. 369-381

[Metcalf and van der Straten, 1999] , H. Metcalf and P. van der Straten,"Laser Cooling and Trapping", Springer-Verlag, 1999

[Williamson, 1997] R. S. Williamson, "Magneto-optical trapping of potassium isotopes", Doctoral Thesis, Univeristy of Wisonconsin- Madison, 1997

[Arnold *et al.*, 1998] A. S. Arnold, J. S. Wilson, and M. G. Boshier, "A simple extended-cavity diode laser", Rev. Sci. Inst. Vol 69, No. 3, p. 1236-1239, March 1998

[Yavin *et al.*, 2002] I. Yavin et al. "A calculation of the time-of-flight distribution of trapped atoms" Am. J. Phys. 70 (2) Feb 2002 p. 149-152

[Gerz *et al.*, 1993] C. Gerz et al. "The temperature of optical molasses for two different atomic angular momenta". Europhysics Letters 21 (6) pp 661-666 Feb 1993

[Anderson *et al.*, 1993] M. H. Anderson, W. Petrich, J. R. Ensher, E. A. Cornell, "Reduction of light-assisted collisional loss rate from a low-pressure vapor-cell trap", Physical Review A, Vol 50, R34947, 1994

[Ashkin, 1970] A. Ashkin "Acceleration and trapping of particles by radiation pressure" Phys. Rev. Lett. Vol. 24, p. 156 (1970)

[Gordon *et. al*, 1980] J. P. Gordon and A. Ashkin, "Motion of atoms in a radiation trap", Phys. Rev. A, Vol 21. No. 5 Pp. 1606-1617, May 1980

[Kadar-Kallen and Bonin, 1992] M. A. Kadar-Kallen and K. D. Bonin, "Light-force technique for measuring polarizabilities", Phys. Rev. Lett. Vol. 68, p. 2015, (1992)

[Dalibard *et al.*, 1985] J. Dalibard and C. Cohen-Tannoudji, "Dressed-atom approach to atomic motion in laser light: the dipole force revisited", J. Opt. Soc. B, Vol 2, No. 11, Pp. 1707-1720, November 1985

[Chu *et al.*, 1986] S. Chu, J. Bjorkholm, A. Ashkin, and A. Cable, "Experimental observation of optically trapped atoms" Phys. Rev. Lett. Vol 57, p 314 (1986)

[Miller *et al.*, 1993] J. D. Miller, R. A. Kline, and D. J. Heinzen, "Far-off-resonance optical trapping of atoms", Phys. Rev. A, vol. 47 No. 6, pp R4567-R4570, June 1993

[Han *et al.*, 2000] D.-J. Han, S. Wolf, S. Oliver, C. McCormick, M. T. DePue, and D. S. Weiss, "3D Raman sideband cooling of cesium atoms at high density", Phys. Rev. Lett. vol. 85, no. 4, pp 724-727, July 2000

[Takasu *et al.*, 2003] Y. Takasu, K. Maki, K. Komori, T. Takano, K. Honda, M, Kumakura, T. Yabuzaki, and Y. Takahashi, "Spin-singlet Bose-Einstein Condensation of two-electron atoms", Phys. Rev. Lett., Vol 91, No. 4, p. 040404-1, July 2003

[Weber *et al.*, 2003] T. Weber, J. Herbig, M. Mark, H-C. Nägerl, R. Grimm, "Bose-Einstein Condensation of Cesium", Science, Vol. 299, P. 232, January 2003

[Kerman *et al.*, 2001] A. J. Kerman, C. Cheng, V. Vuletic, S. Chu, P. J. Leo, C. J. William, and P. S. Julienne, "Determination of Cs-Cs interaction parameters using Feshbach spectroscopy", Comptes Rendus de l'Academie des Sciences, Serie IV: Physique, Vol 2, Iss. 4, P. 633-9, June 2001

[Granade *et al.*, 2002] S. R. Granade, M. E. Gehm, K. M. O'Hara, and J. E. Thomas, "All-optical production of a degenerate Fermi gas", Phys. Rev. Lett. Vol 88, No. 12, P. 120405, March 2002

[Friebel *et al.*, 1998] S. Friebel, R. Scheunemann, J. Walz, T. W. Hänsch, and T. W. Weitz, "Laser cooling in a CO_2 laser optical lattice", Appl. Phys. B, Vol. 67, Pp. 699-704, 1998

[Dumke *et al.*, 2002] R. Dumke, M. Volk, T. Muther, F. B. J. Buchkremer, G. Birkl, and W. Ertmer, "Micro-optical realization of arrays of selectively addressable dipole traps: a scalable configuration for quantum computing with atomic qubits", Phys. Rev. Lett, Vol 89, P. 097903, August 2002

[Boiron *et al.*, 1998] D. Boiron, A. Michaud, J. M. Fournier, L. Simard, M. Sprenger, G. Grynberg, and C. Salomon, "Cold and dense cesium clouds in far-detuned dipole traps", Phys. Rev. A. Vol. 57, Pp. R4106

[Vuletic *et al.*, 1998] V. Vuletic, C. Chin, A. Kerman, and S. Chu, "Degenerate Raman sideband cooling of trapped cesium atoms at very high atomic densities", Phys Rev. Lett. Vol. 81, Pp 5768, December 1998

[Kerman *et al.*, 2000] A. Kerman, V. Vuletic, C. Chin, and S. Chu, "Beyond optical molasses: 3D Raman sideband cooling of atomic cesium to high phase space density", Phys. Rev. Lett. Vol. 84, Iss. 3, P. 439-442, January 2000

[Corwin *et al.*, 1999] K. Corwin, S. Kuppens, D. Cho, and C. Wieman, "Spin-polarized atoms in a circularly polarized optical dipole trap" Phys. Rev. Lett. Vol. 83, No. 7, Pp. 1711- 1714, August 1999

[Ketterle and van Druten, 1996] W. Ketterle and N. J. van Druten, "Evaporative cooling of trapped atoms", Adv. in At. Mol. and Opt. Phys., Vol. 37, P. 181, 1996

[Heareus *et al.*, 1961] J. Opt. Sci. Am. Vol. 51, p. 1058, (1961)

[Savard *et al.*, 1997] T. A. Savard, K. M. O'Hara, and J. E. Thomas, "Laser noise induced heating in far-off resonant atomic traps", Phys. Rev. A Vol. 56 R1095 (1997)

[Gehm *et al.*, 1998] M. E. Gehm, K. M. O'Hara, T. A. Savard, and J. E. Thomas, "Dynamics of noise-induced heating in atom traps", Phys. Rev. A Vol. 58, P. 3914 (1998)

[Bali *et al.*, 1999] S. Bali, K. M. OHara, M. E. Gehm, S. R. Granade, and J. E. Thomas "Quantum-diffractive background gas collisions in atom-trap heating and loss", Physical Review A, Vol. 60, pp. R29 (1999)

[Dalibard and Cohen-Tannoudji, 1989] J. Dalibard and C. Cohen-Tannoudji "Laser cooling below the Doppler limit by polarization gradients - Simple theoretical models" J. Opt. Soc. Am. B, Vol. 6, pp 2023-2045 (1989)

[Ungar *et al.*, 1989] P. J. Ungar, D. S. Weiss, S. Chu, and E. Riis. "Optical molasses and multilevel atoms - Theory" J. Opt. Soc. Am. B, Vol. 6, pp 2058-2071 (1989)

[Nabors *et al.*, 1989] C. D. Nabors, A. D. Farinas, T. Day, S. T. Yang, E. K. Gustafson, and R. L. Byer, "Injection locking of a 13-W cw Nd:YAG ring laser", Opt. Lett. Vol. 14, No. 21, P 1189, November 1989

[Cregut *et al.*, 1989] O. Cregut, C. N. Man, D. Shoemaker, A. Brillet, A. Menhert, P. Peuser, N. P. Schmitt, P. Zeller, and K. Wallmeroth, "18 W single-frequency operation of an injection-locked, CW, Nd:YAG laser" Phys. Lett. A, Vol. 140, No. 6, P. 294. October 1989

[Golla *et al.*, 1993] D. Golla, I. Freitag, H. Zellmer, W. Schöne, I. Kröpke, and H. Welling, "15 W single-frequency operation of a cw, diode laser-pumped Nd:YAG ring laser" Opt. Comm. Vol. 98, P. 86-90, April 1993

[Shine *et al.*, 1995] R. J. Shine, Jr., A. J. Alfrey, and R. L. Byer, "40 W cw TEM_{00}-mode diode- laser-pumped Nd:YAG miniature-slab laser" Opt. Lett. Vol. 20, No. 5, P. 459, March 1995

[Ottaway *et al.*, 2000] D. J. Ottaway, P. J. Veitch, C. Hollitt, D. Mudge, M. W. Hamilton, and J. Munch, "Frequency and intensity noise of an injection-locked Nd:YAG ring laser", App. Phys. B. Vol. 71, Pp. 163- 168, June 2000

[Liem *et al.*, 2003] A. Liem, J. Limpert, H. Zellmer, and A. Tünnermann, "100-W single-frequency master-oscillator fiber power amplifier" Opt. Lett. Vol. 28, No. 17, P. 1537, September 2003

[Richards and McInnes, 1995] J. Richards and A. McInnes, "Versatile, efficient, diode-pumped miniature slab laser" Opt. Lett. Vol. 20, No. 4, P. 371, February 1995

[InnoLight, Lightwave] For instance, the Mephisto from InnoLight (distributed by Linos) which produces 500 mW single-frequency at 1064 nm for $22,500, or the Lightwave Electronics model 126-1064 with a 100 mW single-frequency output for $17,400.

[Davis *et al.*, 1995, b] K. B. Davis, M. O. Mewes, and W. Ketterle. "An analytical model for evaporative cooling of atoms" App. Phys. B, Vol. 60 pp 155-159 (1995)

[O'Hara *et al.*, 2001] , K. M. O'Hara, M. E. Gehm, S. R. Granade, and J. E. Thomas, "Scaling laws for evaporative cooling in time-dependent optical traps", Phys. Rev. A., Vol. 64, P. 051403(R), October 2001